Okinawa Institute of Science and Technology
Graduate University

Thesis submitted for the degree

Doctor of Philosophy

Signatures of Novel Spin Liquids in Kagome-like Lattices

by

Rico Pohle

Supervisor: **Nic Shannon**

November, 2017

Declaration of Original and Sole Authorship

I, Rico Pohle, declare that this thesis entitled *Signatures of Novel Spin Liquids in Kagome-like Lattices* and the data presented in it are original and my own work.
I confirm that:

- This work was done solely while a candidate for the research degree at the Okinawa Institute of Science and Technology Graduate University, Japan.
- No part of this work has previously been submitted for a degree at this or any other university.
- References to the work of others have been clearly attributed. Quotations from the work of others have been clearly indicated, and attributed to them.
- In cases where others have contributed to part of this work, such contribution has been clearly acknowledged and distinguished from my own work.
- None of this work has been previously published elsewhere, with the exception of the following: Chapter 4 has been published in collaboration with *Owen Benton* and *Ludovic Jaubert* in [1].

Date: November, 2017

Signature:

Abstract

Signatures of Novel Spin Liquids in Kagome-like Lattices

The phenomenon of magnetism in solids aroused the curiosity of scientists already in ancient times. While quantum mechanical effects on a single–particle level are well understood, magnets offer phenomena caused by collective interactions between many electrons and provide the opportunity to find novel states of matter. In this context, *frustrated* magnets play a central role, since interactions between local magnetic moments on a crystallographic lattice cannot be satisfied at the same time. This can prevent the systems to order even at very low temperatures, creating a magnetic state similar to those of liquids, which gives them the name *spin liquids*. Within this field, the kagome lattice — a two–dimensional network of corner–sharing triangles — has played a particularly iconic role and continues to provide rich inspiration to theoreticians and experimentalists alike.

In this thesis, we first explore the thermodynamic properties and signatures of classical spin liquids on kagome–like lattices, by the use of complementary analytical Husimi tree and numerical Monte Carlo simulation techniques. The emerging phenomenon of a *Curie–law crossover*, reflecting a crossover between a high–temperature paramagnet and a low–temperature collective paramagnet, turns out to be a powerful signature of exotic physics in classical spin liquids, and explains the difficulty of making a precise estimate of the Curie–Weiss temperature in experiments.

But spin liquids do not necessarily need to show just one Curie–law crossover. The anisotropic Ising model on the *shuriken*, or square–kagome lattice, shows a succession of multiple Curie–law crossovers due to a rich phase diagram with many disordered ground states. Hereby, low–and high–temperature regimes are less correlated than the intervening classical spin liquid, allowing to extend the definition of reentrant phenomena to disordered systems.

Furthermore, we also study dynamical properties of the nearest–neighbour Heisenberg model on the bilayer breathing kagome lattice, which has been motivated by recent experiments on $Ca_{10}Cr_7O_{28}$. Using semi–classical molecular–dynamics simulations, we are able to reproduce many features seen by inelastic neutron scattering experiments and provide a first explanation of its spin–liquid origin. Surprisingly, we find that excitations encode not one, but two distinct types of spin liquids at different time scales. Fast fluctuations reveal a *Coulombic spin liquid*, as known from the classical kagome–lattice antiferromagnet, while slow fluctuations reveal a *spiral spin liquid*, which can be understood by a mapping onto an effective spin-3/2 honeycomb model.

Acknowledgment

I am very honoured and pleased to be one of the first PhD students of the Okinawa Institute of Science and Technology Graduate University (OIST) and want to express my sincere gratitude to all people involved in its past and present development, allowing me to do my doctoral studies on this very special island.

My PhD studies would have never reached to this point without the support of many people. Firstly, I would like show my deep appreciation to *Nic Shannon* for his continuous support since the first time we met at the "Paul Rackwitz", a very nice, local restaurant in Dresden–Plauen. While talking about OIST, I would have never thought to do a PhD in theoretical physics in my near future. However, his optimism, love for physics, and engagement for a deep understanding of "everything" were exceptionally inspiring from the first time we met until the end of my PhD. Secondly, I would like to thank *Ludovic Jaubert*, for his valuable supervision, since my lab–rotation in the TQM unit at OIST. Next to providing me with all fundamental secrets of Monte Carlo simulations and statistical mechanics, and not–forgettable times late at night in the office, where "short questions" easily expanded into very interesting multiple–hour discussions, I enjoyed his enthusiasm, positivity and pedagogical know–how. Thirdly, I want to thank *Mathieu Taillefumier* for teaching me everything I know about high–performance programming and molecular dynamics simulations. Even at very busy times he was available and happy to help out, by convincing my computer code to work as intended. I also want to thank *Han Yan*, who initiated the work on the $Ca_{10}Cr_7O_{28}$ project (Chapter 5), by brilliantly spotting the connection between different underlying spin–liquid models for this material.

Personally, I want to deeply thank the members of the OIST Karate Club for their continuous support over the last 5 years, enabling me to practice and improve my physical and pedagogical karate skills. Especially I want to thank *Kimberly Remund*, who basically attended the Karate practice more often than I did, and gave me the secure feeling, that there will be definitely, at any time, at least one student waiting for me in the Dojo. I am in deep dept to my parents and my family back home in Germany, who supported me throughout my whole life and never pushed or criticised me on any of my decisions, as well as my "new" family here in Okinawa, who included me from the first day we met as their "Uchinaa Muukuu" (Okinawan son). Last but not least, I want to thank my wife *Yuno Pohle Kaneshi*. I would have not been able to finish my studies without her support from the first day I arrived at OIST — while she was working for the Graduate School — until the end of my thesis. Her optimism and attitude to learn and improve herself every day is highly inspiring and encouraging, and allows me to look into a bright future of whatever might await on our way.

Contents

List of Figures

List of Tables

Chapter 1

Introduction to Magnetism and Spin Liquids

" *Dass ich erkenne, was die Welt*
Im Innersten zusammenhält."

Faust 1, Vers 382 f. (Faust)
Johann W. v. Goethe

While quantum mechanical effects on a single–particle level are well understood, magnets offer phenomena caused by collective interactions between many electrons, and provide the opportunity to unveil novel states of matter. To study the "social life" of particles, which allows for such unconventional phases, frustrated magnets found their way into active research areas more than 30 years ago [2, 3] and grew to become one of the most active topics in many–body physics today.

Conventional magnets are described by their ordering process into a symmetry–broken state. On the other hand, in frustrated magnets the interaction energy on all magnetic degrees of freedom cannot be minimised simultaneously, which generally suppresses conventional order. Subdominant interactions become predominant and allow for unconventional types of order and novel states of matter, like spin liquids, which do not order at any temperature.

In its own way, this research is as fundamental as the search for new particles in high–energy physics. Indeed the Higgs boson was first proposed in the context of a superconductor [4, 5, 6], while the first observation of magnetic monopoles [7, 8] and Majorana fermions [9] have taken place in magnets.

1.1 Origin of Magnetism in solids

Magnetism is one of the fundamental forces in physics, which caught the interest of researchers already in ancient times. However, a modern understanding of magnetism in solids dates back not much further than to the end of the 19^{th} century. While e.g. *Pierre Curie* [10] and *Pierre Weiss* [11] significantly contributed to an understanding of thermodynamic properties in magnetic crystals, a microscopically exact understanding of magnetism still needed to wait until the invention of modern quantum mechanics.

1.1.1 A historical summary

Magnetism has been known since antiquity from lodestone, a naturally occurring form of magnetite (Fe_3O_4). Greek philosophers wrote about lodestone around 800 B.C., while Chinese writings about magnetite date back to 4000 B.C., assuming that the original discoveries were made in China [12]. A pivoted–needle compass developed before 1000 A.D. has been used in China for navigation on land and water, and also became highly important in the 13$^{\text{th}}$ century in medieval Europe [12, 13].

However, the first scientific investigation of the phenomena of magnetism happened 1269 by *Pierre Pélerin de Maricourt* [14], who described simple laws of magnetic attraction. Following de Maricourt's work, the English scientist *William Gilbert* published three centuries later *"De Magnete"*, a landmark treatise, to be the first which clearly distinguishes electric from magnetic effects and also explains that the earth by itself behaves like a large magnet [15].

It was the danish physicist *Hans Christian Ørsted*, who in 1819 discovered the link between electricity and magnetism, by placing a compass needle near a wire with an electric current [16]. While *Biot*, *Savart* and *Ampere* established the relationship of the magnetic induction and the current that generates it, *James Clerk Maxwell* essentially completed in 1865 the classical theory of electromagnetism by showing that electricity and magnetism represent two different aspects of the same fundamental force field [17, 18, 19]. Still without knowing the microscopic mechanism, *Pierre Curie* [10] and *Pierre Weiss* [11] contributed significantly to a modern understanding of magnetic phenomena in solid state physics by examining the effect of temperature on magnetic materials and the existence of phase transitions between magnetically ordered and disordered phases. Indeed, *Pierre Curie* even introduced the concept of symmetry analysis to classify ordered phases in his PhD thesis. However, a microscopically exact understanding of magnetism still needed to wait until the invention of modern quantum mechanics.

The concept of quantisation at the beginning of the 20$^{\text{th}}$ century introduced by *Max Plank* [20] and *Albert Einstein* [21] induced a series of discoveries in the so–called period of "old quantum theory". Fundamental work towards a microscopic understanding of magnetism has been done by *Niels Bohr* [22], who quantised energy levels in the Rutherford's atom. The famous experiment by *Stern* and *Gerlach* allowed the determination of quantised angular and magnetic moments of atoms [23]. In 1921 *Compton* suggested an intrinsic spin and therefore a magnetic moment to electrons [24], which has been proven to be correct by *Goudsmit* and *Uhlenbeck* in 1925 [25]. The magnetic moment of the electron is

$$\mathbf{m}_s = -g\mu_{\text{B}}\frac{\mathbf{S}}{\hbar}\,, \tag{1.1}$$

where $\mathbf{S}$ is the quantised electron spin and the unit of magnetic momentum has been defined with the Bohr magneton

$$\mu_{\text{B}} \equiv \frac{e\hbar}{2m_e}\,. \tag{1.2}$$

The origin of the Landé g–factor $g \cong 2.0023$ could be explained by *Dirac*, who included relativistic aspects of electrons. With his postulation of the particle–wave

duality [26], *Louis de Broglie* provided the starting point for *Schrödinger* to formulate his famous wave equation in 1926 [27]. The Schrödinger equation forms the basis of a successful description of solid–states physics and quantum statistical mechanics

$$\mathcal{H}\Psi_n = E_n\Psi_n \ , \quad n \in \mathbb{N} \ , \tag{1.3}$$

with the ground state Ψ_0 of the system corresponding to the state with the lowest energy eigenvalue E_0 of the Hamiltonian $\mathcal{H}$. At the same time, *Heisenberg* and co–workers developed a synonymous description of quantum systems via harmonic oscillators. Hereby, the use of a coherent formulation of a non–commutative matrix algebra turns out to be a very powerful tool to assign every physical quantity a corresponding mathematical operator.

In 1933 *Arnold Sommerfeld* introduced the free–electron model for solids by applying quantum mechanical Fermi–Dirac statistics and the Schrödinger equation to the classical Drude model [28, 29]. This concept has been formulated in second quantisation as the "band theory of solids", which averages out interaction effects by using the Hartree–Fock approximation (Stoner mean–field theory). A huge number of crystalline solids like metals and insulators could be classified using this method, but showed very quickly its limitations.

Transition and rare–earth metals have in addition to their conduction bands also partially filled d or f orbitals. It turns out, that strong Coulomb repulsion at commensurate filling, can suppress the electrons agility, localise them and make the material insulating, by performing a metal–insulator transition as seen for several simple transition–metal oxides [30]. Materials, which show such a behaviour are called Mott insulators [31] with many unconventional physical properties (reviewed in [32, 33]). The magnetism within those materials cannot be explained by the band theory of solids [34, 35] and requires an extension of concepts. A microscopic model, including interactions of electrons within solids is provided by the well–known Hubbard model, which shall be described in further details in the next section.

1.1.2 Hubbard model

The unification of electricity and magnetism by *Maxwell* [19] and work of *Pierre Curie* [10] and *Pierre Weiss* [11] on fundamental properties of magnetic materials motivated the importance of a microscopic description of magnetism in solids. However, such a description needed to wait for a sound foundation of quantum mechanical concepts. This was also qualitatively stated by *Niels Bohr* in 1911 [36] and *Hendrika Johanna van Leeuwen* in 1921 [37], saying that magnetism in solids is a purely quantum mechanical effect and cannot be described by a classical theory (known as the Bohr–van Leeuwen theorem).

The Hubbard model was introduced in 1963 independently by *Martin Gutzwiller* [38], *Junjiro Kanamori* [39] and *John Hubbard* [40, 41, 42], and formulates the simplest, one–band many–body Hamiltonian which allows for a meaningful description of d and f electron systems with correlated conduction electrons.

Microscopically, those conduction electrons are allowed to occupy and hop between different atomic orbitals. Spatially extended orbitals are expressed as Wannier-

functions $\phi(\mathbf{r}-\mathbf{R}_i)$, an orthogonal set of functions, localised around the position $\mathbf{R}_i$ of the i^{th} ion and rapidly falling off to zero away from it.

In respect to the Pauli exclusion principle, electrons will be created ($\hat{c}^\dagger_{i\sigma}$) and annihilated ($\hat{c}_{i\sigma}$) with spin σ at discrete points $\mathbf{R}_i$ of the crystallographic lattice, following the fermionic anticommutation relations

$$\{\hat{c}_{i\sigma}, \hat{c}^\dagger_{j\sigma'}\} = \hat{c}_{i\sigma}\hat{c}^\dagger_{j\sigma'} + \hat{c}^\dagger_{j\sigma'}\hat{c}_{i\sigma} = \delta_{i,j}\delta_{\sigma,\sigma'} \tag{1.4}$$

$$\{\hat{c}_{i\sigma}, \hat{c}_{j\sigma'}\} = \{\hat{c}^\dagger_{i\sigma}, \hat{c}^\dagger_{j\sigma'}\} = 0\ . \tag{1.5}$$

The Hamiltonian representing the kinetic energy of the system is

$$\mathcal{H}_{\text{t}} = -t \sum_{\langle i,j\rangle\sigma} (\hat{c}^\dagger_{i\sigma}\hat{c}_{j\sigma} + \hat{c}^\dagger_{j\sigma}\hat{c}_{i\sigma})\ , \tag{1.6}$$

whereas the overlap of the physical orbitals has been encoded in the hopping amplitude t. Eq. (1.6) is generally known as the tight–binding Hamiltonian [28], where delocalised electrons do not interact and lead to a conducting behaviour of the system.

Nevertheless, sufficiently dense electrons show correlation effects, due to Coulomb repulsion. A large on–site Coulomb energy

$$U = \int d\mathbf{r}_1 \int d\mathbf{r}_2\ |\phi(\mathbf{r}_1-\mathbf{R}_i)|^2\ \frac{e^2}{|\mathbf{r}_1-\mathbf{r}_2|}\ |\phi(\mathbf{r}_2-\mathbf{R}_i)|^2 \tag{1.7}$$

restricts the hopping of electrons to already occupied orbitals and tends to form an insulator. The energy increase for doubly occupied sites is written as

$$\mathcal{H}_{\text{U}} = U \sum_i \hat{n}_{i\uparrow}\hat{n}_{i\downarrow}\ , \tag{1.8}$$

where the occupation number operator is $\hat{n}_{i\sigma} = \hat{c}^\dagger_{i\sigma}\hat{c}_{i\sigma}$.

The Hubbard model accounts for both terms, Eq. (1.6) and Eq. (1.8)

$$\mathcal{H} = -t \sum_{\langle i,j\rangle\sigma} (\hat{c}^\dagger_{i\sigma}\hat{c}_{j\sigma} + \hat{c}^\dagger_{j\sigma}\hat{c}_{i\sigma}) + U \sum_i \hat{n}_{i\uparrow}\hat{n}_{i\downarrow}\ , \tag{1.9}$$

giving valuable insight into the nature of strongly–correlated electron systems. In the limit of $U/t \gg 1$ and half filling this model describes Mott insulators [43], an important group of materials in the scope of conventional and unconventional magnetism and therefore worth discussing in more detail.

1.1.3 Mott insulators

The microscopic understanding of Mott insulators does not only provide an explanation for the absence of electron conductivity, but also for the emergence of magnetic properties. For pedagogical reasons the magnetic properties in Mott insulators shall be demonstrated on the simple example of a half–filled dimer with strong coulomb interactions $U/t \gg 1$.

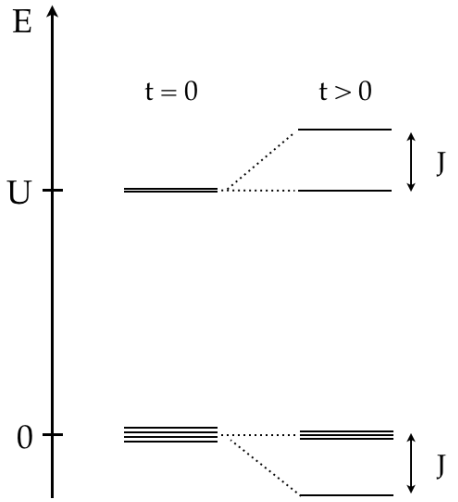

Figure 1.1: Energy spectrum of the Hubbard model for a dimer at half filling. Exact diagonalization of Eq. (1.10) gives a set of states, which are separated by the dominating Coulomb interaction U. A finite hopping t will split degeneracies of these states by $J := 4t^2/U$ and allows the singlet state to be the new grounds state.

The Hubbard model from Eq. (1.9) for two sites, labeled 1 and 2, reads:

$$\mathcal{H}^{\text{dimer}} = -t \sum_{\sigma} (\hat{c}^{\dagger}_{1\sigma} \hat{c}_{2\sigma} + \hat{c}^{\dagger}_{2\sigma} \hat{c}_{1\sigma}) + U(\hat{n}_{1\uparrow}\hat{n}_{1\downarrow} + \hat{n}_{2\uparrow}\hat{n}_{2\downarrow}) \; , \tag{1.10}$$

where $\sigma = \uparrow, \downarrow$. This Hamiltonian has eigenfunctions $|\psi_n\rangle$ and eigenvalues E_n

$$\mathcal{H}^{\text{dimer}} |\psi_n\rangle = E_n |\psi_n\rangle \; . \tag{1.11}$$

In the case of half filling (2 electrons) six possible wave functions are allowed. States with doubly occupied and one empty site form "excited" configurations, since they have to account for a large on–site Coulomb repulsion

$$\begin{aligned} |\text{ex}_1\rangle &= |\uparrow\downarrow, 0\rangle \; , \\ |\text{ex}_2\rangle &= |0, \uparrow\downarrow\rangle \; . \end{aligned} \tag{1.12}$$

Non–excited states are states with singly occupied sites. Those form one singlet and three triplet states and are denoted by their spin quantum numbers $|S, S^z\rangle$

$$\begin{aligned} |1,1\rangle &= |\uparrow,\uparrow\rangle \; , \\ |1,0\rangle &= \frac{1}{\sqrt{2}}(|\uparrow,\downarrow\rangle + |\downarrow,\uparrow\rangle) \; , \\ |1,-1\rangle &= |\downarrow,\downarrow\rangle \; . \end{aligned} \tag{1.13}$$

$$|0,0\rangle = \frac{1}{\sqrt{2}}(|\uparrow,\downarrow\rangle - |\downarrow,\uparrow\rangle) \; . \tag{1.14}$$

Diagonalising Eq. (1.10) reveals the following eigenvalues

$$E_5 = \frac{1}{2}(U + \sqrt{U^2 + 16t^2}) \approx U + \frac{4t^2}{U} \ , \tag{1.15}$$

$$E_4 = U \ , \tag{1.16}$$

$$E_1 = E_2 = E_3 = 0 \ , \tag{1.17}$$

$$E_0 = \frac{1}{2}(U - \sqrt{U^2 + 16t^2}) \approx -\frac{4t^2}{U} \ , \tag{1.18}$$

up to second order in t/U, where the energies for the triplet states are equal to zero. The corresponding wave functions are

$$|\psi_5\rangle \approx -\frac{2t}{U}|0,0\rangle + \frac{1}{\sqrt{2}}\left(1 - \frac{2t^2}{U^2}\right)(|\mathrm{ex}_1\rangle + |\mathrm{ex}_2\rangle) \ , \tag{1.19}$$

$$|\psi_4\rangle = \frac{1}{\sqrt{2}}(|\mathrm{ex}_1\rangle - |\mathrm{ex}_2\rangle) \ , \tag{1.20}$$

$$\begin{aligned} |\psi_3\rangle &= |1,1\rangle \ , \\ |\psi_2\rangle &= |1,0\rangle \ , \\ |\psi_1\rangle &= |1,-1\rangle \ , \end{aligned} \tag{1.21}$$

$$|\psi_0\rangle \approx \left(1 - \frac{2t^2}{U^2}\right)|0,0\rangle + \frac{\sqrt{2}t}{U}(|\mathrm{ex}_1\rangle + |\mathrm{ex}_2\rangle) \ , \tag{1.22}$$

where triplet wave functions are left unchanged.

As seen in Fig. 1.1 the system provides degenerate states at high and low energy in absence of an electron hopping $t = 0$. In a real lattice, those states would transform into bands, which then are commonly referred to as the upper and lower Hubbard bands. A finite kinetic energy $t > 0$ splits the degeneracies by $J := 4t^2/U$ and allow the singlet $|\psi_0\rangle$ to be the new ground state with energy $E_0 < 0$. The ground state mixes with $|\mathrm{ex}_1\rangle$ and $|\mathrm{ex}_2\rangle$ [Eq. (1.22)], providing a small but finite probability of finding doubly occupied sites in the ground state.

A large onsite Coulomb interaction $U \gg t$ separates states of low lying energy from excited ones. It becomes quite unlikely for electrons to occupy the excited states at very low temperatures, which is why a simplification of the Hubbard model — usually achieved by a canonical transformation [43] — allows to consider just the low–lying energy states. Such a simplification leads to the celebrated Heisenberg model, the core model for most theoretical descriptions of insulating magnets.

1.1.4 Heisenberg model

The ground state properties in a Mott insulator are described by singlet and triplet states in the lower Hubbard band. Their ground state physics is well explained by the celebrated Heisenberg model:

$$\mathcal{H}_{\mathrm{eff}} = J \sum_{\langle ij \rangle} \mathbf{S}_i \cdot \mathbf{S}_j + \mathrm{const} \ , \tag{1.23}$$

where $\sum_{\langle ij \rangle}$ runs over all sites i connected to neighbouring sites j via the bond–dependent exchange term J_{ij}. The spin operator on site i is represented by the Pauli matrix $\boldsymbol{\sigma}$

$$\mathbf{S}_i = \frac{1}{2} \sum_{\alpha\beta} \hat{c}^{\dagger}_{i\alpha} \boldsymbol{\sigma}_{\alpha\beta} \hat{c}_{i\beta} \ , \tag{1.24}$$

where one can see that the term $\mathbf{S}_i \cdot \mathbf{S}_j$ in Eq. (1.23) accounts for virtual hopping, or also "exchange" of electrons between two connected sites.

To convince oneself, that this concept is correct, one can again consider the example of a two site Mott insulator, where the product of spin operators with eigenvalue $S = 1/2$ is

$$\mathbf{S}_1 \cdot \mathbf{S}_2 = \frac{1}{2} \Big[(\mathbf{S}_1 + \mathbf{S}_2)^2 - 2S(S+1) \Big] \ . \tag{1.25}$$

It is easy to see that $\mathbf{S}_1 + \mathbf{S}_2 = 0$ and $\mathbf{S}_1 \cdot \mathbf{S}_2 = -3/4$ for the singlet, while $\mathbf{S}_1 + \mathbf{S}_2 = 1$ and $\mathbf{S}_1 \cdot \mathbf{S}_2 = 1/4$ for the triplet states. The result from the Hubbard model [Eq. (1.17) and Eq. (1.18)] can be reproduced by taking $J = 4t^2/U$ and the constant in Eq. (1.23) to $-J/4$.

Historically motivated by phenomena in Cuprate superconductors, which are basically doped Mott insulators, this model has been extended to the famous t-J model [44], allowing to describe correlated systems away from half filling [43, 45, 46, 47]. This model also allows the inclusion of higher order terms like further–neighbour interaction and higher–order spin–exchange terms, as e.g. the biquadratic term $\propto (\vec{S}_i \cdot \vec{S}_j)^2$ [43].

1.1.5 Anisotropic exchange

In Eq. (1.23), all spin components, S^x, S^y and S^z were considered on an equal footing. However, this is only true if effects like spin–orbit coupling are neglected. In general, the electron spin is coupled to its orbital momentum, which is influenced by the crystal field and therefore provides a mechanism where the spin can "feel" the orientation of the crystal axes. This phenomenon of magnetic anisotropy can be described by an anisotropic exchange Heisenberg Hamiltonian with the direction–dependent couplings J^z and $J^{\perp}$, parallel and perpendicular to the local field axes.

$$\mathcal{H} = \sum_{\langle ij \rangle} \left(J^{\perp}_{ij} (S^x_i S^x_j + S^y_i S^y_j) + J^z_{ij} S^z_i S^z_j \right) \ . \tag{1.26}$$

In the classical limit, there are commonly three different models:

- **Heisenberg model:** no orientation is favoured $J^{\perp} \approx J^z$. The spins contain $\mathbb{O}(3)$ symmetry, have two degrees of freedom and can point along any direction on the three–dimensional sphere.

- **XY model:** the crystal field suppresses the coupling between the local z–components of the spins $J^{\perp} \gg J^z$. The spins contain $\mathbb{O}(2)$ symmetry, have one degree of freedom and can point in any direction on a circle, perpendicular to the local z–direction.

- **Ising model:** the crystal field favours the coupling of spins along the local z–direction. $J^{\perp} \ll J^{z}$. The spins contain $\mathbb{Z}_2$ symmetry and can point just in two directions.

Different lattice symmetries can produce more complicated anisotropic exchange behaviour, such as Dzyaloshinski–Moriya interaction [48, 49].

1.2 Magnetic order in conventional magnets

Being able to formulate a microscopic model for a magnetic material is a fundamental step towards its complete physical description. However, solving such models exactly is quite often not possible, and requires approximations as given by simulation or field–theoretical methods.

The mean–field approach is a first step to simplify a complicated model Hamiltonian and estimate thermodynamic properties like phase transitions in conventional magnets. A general theory for explaining phase transitions and classifying various types of ordering mechanisms within them is provided by the Landau theory, which also shall be part of the discussions in this section.

1.2.1 Mean–field theory

Mean–field theory is a very general and usually the first approach to get insight into systems with complex magnetic correlations or unknown physical properties. It is an approximation, which neglects magnetic fluctuations and allows for a much simpler treatment of the problem at hand. This significant method has been introduced by *Pierre Curie* [10] and *Pierre Weiss* [11] to provide a simplified theory for phase transitions in ferromagnets [50].

An illustrative example for applying mean–field theory is provided by the Ising model

$$\mathcal{H} = J \sum_{\langle ij \rangle} \sigma_i \sigma_j - h \sum_i \sigma_i \; . \tag{1.27}$$

Hereby, the exchange interaction J couples nearest–neighbour spins on sites i and j with Ising degree of freedom $\sigma_i = \pm 1$. In the following one should consider $J < 0$ (ferromagnetic interaction) on the central site σ_0, which is surrounded by q neighbouring spins for the square lattice with lattice–coordination number $q = 4$. By averaging out fluctuations on these neighbouring spins

$$\langle \sigma_i \rangle = m \qquad 0 < i \leq q \; , \tag{1.28}$$

the new mean–field Hamiltonian will have the form

$$\mathcal{H}_{MF} = (Jqm - h)\sigma_0 \; . \tag{1.29}$$

The expectation value of the central site $\langle \sigma_0 \rangle$ follows from

$$\begin{aligned} m = \langle \sigma_0 \rangle &= \frac{\sum_{\{\sigma_0\}} \sigma_0 \; e^{-\beta \mathcal{H}_{MF}}}{\sum_{\{\sigma_0\}} e^{-\beta \mathcal{H}_{MF}}} \\ &= \tanh\big[-\beta(Jqm - h) \big] \; , \end{aligned} \tag{1.30}$$

where translational invariance of the lattice allows to set $\langle\sigma_i\rangle = \langle\sigma_0\rangle = m$.

The self–consistent Eq. (1.30) needs to be solved numerically or graphically and provides for $h = 0$ one trivial ($m_0 = 0$) and two non–trivial ($m_0 \neq 0$) solutions at exactly the critical temperature T_c

$$\frac{T_\mathrm{c} k_B}{|J|} = q \; . \tag{1.31}$$

The two–dimensional square lattice with $q = 4$ and ferromagnetic interactions shows a phase transition temperature $T_\mathrm{c} k_B/|J| = 4$, which is comparable, but still quite different from the exact result of $T_\mathrm{c} k_B/|J| = 2.269$ [51]. Similar mean–field techniques with probably better accuracy are available by the Bethe approximation [52, 53], and models on the Bethe lattice [52, 54, 55], which shall be explained for frustrated lattices in more detail in Section 2.1 and Chapter 3.

However, a very general theory of phase transitions is provided by Landau theory, which shall be the topic of the next section.

1.2.2 Landau theory

Many types of phase transitions exist as e.g. melting and crystallisation, evaporation and condensation, but also between different forms of solids, fluid–superfluid, or conducting–superconducting transitions. It was *Lev Landau* in 1936 who thought about a general theory for explaining such phase transitions [56], which shall here be applied to magnets.

The standard observable representing magnetic properties is the magnetisation m, which shall in the following correspond to the magnetic order parameter of an Ising magnet. To describe the phenomenon of phase transitions *Landau* expanded the free energy $\mathcal{G}(m,T)$ close to the critical temperature T_c

$$\begin{aligned} \Delta\mathcal{G}(m,T) &= \mathcal{G}(m,T) - \mathcal{G}(0,T) \\ &= \frac{b(T)}{2} m^2 + \frac{c(T)}{4} m^4 + \frac{d(T)}{6} m^6 + \cdots \; , \end{aligned} \tag{1.32}$$

here, presented for the case of the free energy function even in m. In more general models, cubic terms may also be allowed in the free energy, usually driving first order phase transitions.

It is assumed that $\mathcal{G}(m,T)$ is analytic at exactly the critical temperature, which generally is incorrect, since the only singular feature of a system performing a phase transition is exactly at T_c. Nevertheless, Landau theory works surprisingly well in classifying the nature of phase transitions and predicting physical observables in materials [57].

The temperature dependent coefficients $b(T), c(T)$ and $d(T)$ allow to modify the behaviour of Eq. (1.32) such that different types of magnetic phase transitions with different order can occur. The order of a phase transition equals the order of the lowest–order derivative in the free energy $-\frac{\partial\mathcal{G}}{\partial h}\big|_{h=0} = m$, which shows a discontinuity at the critical temperature.

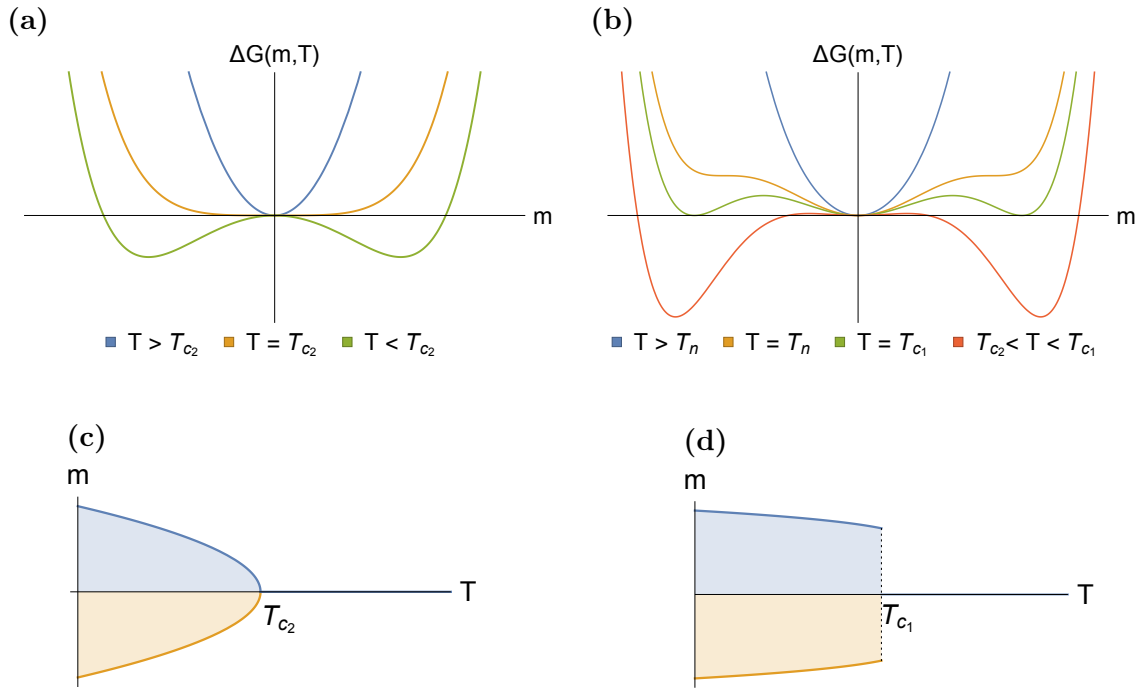

Figure 1.2: Landau theory for 2^{nd} and 1^{st} order phase transitions. Gibbs free energy $\Delta\mathcal{G}(m,T)$ [Eq. (1.32)] as a function of magnetisation m and temperature T. (a) Characteristic behaviour for a 2^{nd} order phase transition, with parameter $b(T) = b_0(T - T_{c_2})$ and b_0, c, d positive. T_{c_2} is the critical temperature, where the system magnetically orders into $+|m_0|$ or $-|m_0|$ as seen in (c). (b) Characteristic behaviour for a 1^{st} order phase transition, with $c(T)$ that changes sign at T_n, where $T_n > T_{c_2}$. Local minima in $\Delta\mathcal{G}(m,T)$ appear below T_n, which become global minima at T_{c_1}, why the magnetisation shows a jump, as seen in (d).

2^{nd} order phase transition

In a 2^{nd} order phase transition the correlation length diverges, causing strong correlations of spins throughout the lattice. Assuming that the leading term in the free energy [Eq. (1.32)] will change its behaviour at the critical temperature T_{c_2}, the pre factor $b(T) = b_0(T - T_{c_2})$ shall change its sign, whereas other coefficients $c(T), d(T), \ldots$ shall stay positive and constant. For temperatures above T_{c_2}, ΔG will have just one global minimum at $m = 0$, whereas for $T < T_{c_2}$ ΔG shows two degenerate non–trivial global minima

$$m_0 = \begin{cases} 0 & \text{if } T \geq T_{c_2} \\ \pm\sqrt{-\frac{b_0}{c}\,(T - T_{c_2})} & \text{if } T < T_{c_2}\ , \end{cases} \tag{1.33}$$

as shown in Fig. 1.2(a). At the critical temperature $T = T_{c_2}$ the potential is quartic, instead of quadratic, which allows for a large set of nearly degenerate ground states fluctuating around the global minimum $m = 0$. Below T_{c_2} two degenerate ground states are available. Since the system cannot occupy both states with an opposite magnetisation at the same time, it has to choose one of them, which happens via the

process of spontaneous symmetry breaking. Since the first derivative of the free energy $-(\partial G/\partial h)_h \equiv m$ is continuous, but not the second one, the transition is called 2^{nd} order or continuous phase transition.

1^{st} order phase transition

First order phase transitions are characterised by a discontinuity in the magnetisation at the critical temperature T_{c_1} as shown in Fig. 1.2(d), however without a diverging correlation length. The entropy also changes discontinuously at T_{c_1} by releasing latent heat.

By assuming $b(T)$ and $d(T)$ to be positive over the considered temperature region and $c(T)$ becoming negative below a temperature $T < T_n$, local minima for $m_0 \neq 0$ will occur in $\mathcal{G}(m,T)$ [Eq. (1.32)]. For $T < T_{c_1}$ these minima will become global minima, responsible for a jump in the order parameter from 0 to m_0. This can be seen by imposing the condition $\mathcal{G}(m_0,T_{c_1}) = \mathcal{G}(0,T_{c_1})$ and $\frac{\delta G}{\delta m}\big|_{m_0} = 0$, which will provide the magnetisation of the ordered state at T_{c_1}

$$m_0^2 = -\frac{3c(T_{c_1})}{4d} \tag{1.34}$$

by relating the coefficients of Eq. (1.32) as

$$b(T_{c_1}) = \frac{3c^2}{16d} > 0\ . \tag{1.35}$$

This justifies, that the critical temperature for 1^{st} order phase transitions occurs at higher temperatures, than phase transitions of 2^{nd} order $T_{c_1} > T_{c_2}$.

Assuming $b(T)$ and $c(T)$ to become negative at the same temperature ($T_n = T_{c_2}$), forbids the formation of metastable states, making the phase transition again continuous. Such a point in parameter space is called a tricritical point and separates different phase transition lines from each other.

Critical exponents

As shown for the magnetisation $m \propto (T - T_c)^{1/2}$ [Eq. (1.33) and Eq. (1.34)] thermodynamic observables follow a power law scaling close to the critical temperature T_c. These exponents are called critical exponents, written for thermodynamic observables as

$$\begin{aligned}
\chi(0,T) &\propto |T - T_c|^{-\gamma}\ , \\
C_h(0,T) &\propto |T - T_c|^{-\alpha}\ , \\
\xi(0,T) &\propto |T - T_c|^{-\nu}\ , \\
m(0,T) &\propto |T - T_c|^{\beta}\ , \\
|m(h,T_c)| &\propto |h|^{-1/\delta}\ .
\end{aligned} \tag{1.36}$$

Critical exponents are independent of the microscopic details of the system and just depend on the symmetry of the order parameter and its dimension. They fall into universality classes, classifying the nature of their phase transitions [43, 53].

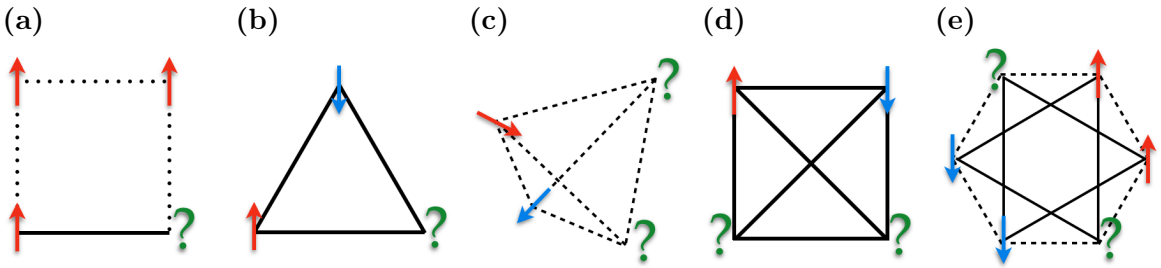

Figure 1.3: Different frustrated unit cells. (a) Ising spins on a chemically frustrated square, (b) a triangle, (c) a tetrahedron, (d) a square with further nearest–neighbour interactions and (e) a hexagon with further nearest–neighbour interactions. Dotted lines represent ferromagnetic interactions, while lines represent antiferromagnetic interactions. Due to the given configurations, the spins on the marked "**?**" are not able to minimise the energy of the unit cell by choosing a particular direction.

In the case of Landau theory, these exponents will take the following values

$$\beta = 1/2\,, \quad \delta = 3\,, \quad \gamma = 1\,, \quad \alpha = 0\,, \quad \text{and} \quad \nu = 1/2\,, \tag{1.37}$$

which are the values for a mean–field theory, since it neglects fluctuations in the system by considering a mean value of magnetisation m [Eq. (1.32)]. However, fluctuations can be introduced by an additional term $(\nabla m(\mathbf{r}))^2$, giving rise to the Landau–Ginzburg theory [58, 59], a theory enjoying large popularity in application also to superconductivity [60, 61, 62] and nonequilibrium physics [63].

A comparison to the previous result for Ising model (Section 1.2.1) gives the following coefficients:

$$b(T) = k_B(T - T_\mathrm{c}) \qquad \text{and} \qquad c(T) = \frac{k_B}{3}\left(\frac{T_\mathrm{c}^3}{T^2}\right). \tag{1.38}$$

1.3 Frustrated Magnetism

A magnetic system is said to be frustrated, when a simultaneous minimisation of the interaction energy between all degrees of freedom is impossible. Although, frustrated models have been studied in the context of water ice by *Bernal & Fowler* already in 1933 [64] and *Pauling* in 1935 [65], the term frustration in magnetism appeared the first time 1977 in a paper on spin glasses by *Toulouse* [66] and *Villain* [67], while geometrically frustrated antiferromagnets were pointed out by *Houtappel* [68], *Wannier* [69] and *Anderson* [70] in the 1950s.

Frustrated magnets can be divided into multiple categories. In one of them, chemical disorder causes a random arrangement of ferro and antiferromagnetic bonds on the lattice, as shown in the simple example for the square lattice in Fig. 1.3(a). This class of materials is generally known as spin glasses [71, 72, 73] and has motivated wide experimental and theoretical activity, aimed at e.g. the understanding of the nature of spin freezing and detection of a true thermodynamic spin–glass phase transition [66, 74].

Another category is represented by geometrically frustrated magnets, where a simultaneous satisfaction of interaction energies on all available bonds is not possible due to the geometric arrangement of lattice sites. This effect usually happens in antiferromagnetic models on lattices containing triangular plaquettes [Fig. 1.3(b)] as in triangular or kagome lattices, but can also appear in ferromagnetic models on e.g. the pyrochlore lattice, as in spin ice, where Ising spins pointing in or out of the centre of a tetrahedron [Fig. 1.3(c)].

However, frustrated magnets do not need to be restricted to geometric frustration only. Models with further–neighbour exchange interaction can also induce frustration, as e.g. shown on the antiferromagnetic Heisenberg model on the bipartite square [Fig. 1.3(d)] or honeycomb lattice [Fig. 1.3(e)].

For a very comprehensive introduction into the subject, the reader might refer to the book *"Introduction to Frustrated Magnetism: Materials, Experiments, Theory"* [3] and a review dedicated especially to pyrochlore oxides [75].

1.3.1 Properties of frustrated magnets

After providing an exact solution in two–dimensions by *Onsager* and *Kaufman* [51, 76, 77], thermodynamic properties of the Ising model on various lattice types became accessible. It turned out, that the Ising model on the triangular lattice has the rather interesting property of a residual entropy $S(T \to 0) \approx 0.3383$ [69], according to the effect of frustration, as shown in Fig. 1.3(b).

In 1973, *Phil Anderson* referred to the triangular lattice by stating, that the quantum model with antiferromagnetic nearest–neighbour interactions allows for a Resonance Valence Bond (RVB) ground state [78, 79]. By resonating between different arrangements of singlet–dimer coverings on this lattice, the RVB state — the first example of a quantum spin liquid state — is disordered down to the lowest temperatures. Since the suggestion of their possible relevance to cuprate superconductors in 1987 [80], insulating materials made of triangular unit cells were the focus of intensive studies and play until now a crucial role in the development of a fundamental understanding of spin liquids.

Obviously spin liquid behaviour can also be achieved in non–triangular frustrated unit cells as seen in pyrochlore and checkerboard [3], or other lattices with further nearest–neighbouring coupling like the J_1-J_2 Heisenberg model on the honeycomb lattice [81] or the J_1-J_2-J_3 Heisenberg model on the square lattice [82].

Classical Ground State Degeneracy

To understand the absence of order in spin liquids, one needs to understand their ground state properties. Each frustrated unit cell in Fig. 1.3(b)–(d) shows a 6–fold degenerate ground state manifold, due to lattice and time–reversal symmetry. Considering real systems with a total number of sites in the order of the Avogadro number, one can easily see that the ground state manifold of such a frustrated system will remain highly degenerate, giving rise to an extensive entropy.

The Maxwellian counting argument can be used to make a statement about the number of ground states in spin liquids. The number of ground state degrees of freedom

D is given by the difference of the total number of degrees of freedom F and the number of constraints K that must be satisfied.

Many frustrated lattices are made of corner–sharing units, such as e.g. the kagome and pyrochlore lattice. On such lattices, isotropic interactions can be written as

$$\mathcal{H} = J \sum_{\langle ij \rangle} \mathbf{S}_i \cdot \mathbf{S}_j = \frac{J}{2} \sum_{\alpha}^{N} \mathbf{L}_\alpha^2 + \text{const} \ , \tag{1.39}$$

where α runs over all N corner–sharing units of total spin $\mathbf{L}_\alpha$ in the lattice. The ground state of the classical Heisenberg antiferromagnet on the kagome and pyrochlore lattices follows the constraint

$$\mathbf{L}_\alpha = \sum_{i=1}^{q} \mathbf{S}_{i,\alpha} = 0 \qquad \text{for all unit cells} \ , \tag{1.40}$$

where q defines the total number of sites on one corner–sharing unit ($q = 3$ for kagome, $q = 4$ for pyrochlore).

The $O(n)$–symmetric Hamiltonian can be minimised by respecting n local constraints $L_\alpha^{x_1} = L_\alpha^{x_2} = \ldots = L_\alpha^{x_n} = 0$, while there are $(n-1)q$ degrees of freedom shared between two neighbouring unit cells. The difference between degree of freedom F and number of constraints K gives the number of ground state degree of freedom D for the entire system:

$$F = Nq(n-1)/2 \ , \tag{1.41}$$

$$K = nN \ , \tag{1.42}$$

$$D = F - K = \frac{N}{2}(n(q-2) - q) \ , \tag{1.43}$$

The counting argument for the Heisenberg model on the pyrochlore lattice ($n = 3$, $q = 4$) gives $D = N$, linearly depending on the number of tetrahedra in the lattice, and is therefore extensive.

On the other hand, the estimate for the XY model on the pyrochlore lattice ($n = 2$, $q = 4$) or the Heisenberg model on the kagome lattice ($n = 3$, $q = 4$) would give $D = 0$ and therefore naively predicts order [83, 84]. In that sense these models are exactly at the border, where the Maxwellian counting argument underestimates the ground state degrees of freedom. The assumption of constrained isolated unit cells in Eq. (1.43) does not include correlations beyond a single unit within the ground state manifold as e.g. necessary to capture weather vane modes in the kagome antiferromagnet [refer to Fig. 1.5(b) in Section 1.3.2]. In that context, corrections of the counting argument are important, if they contribute to the ground state degeneracy of the system.

One might ask, if an extensively degenerate ground state manifold is robust against thermal fluctuations. At any nonzero temperature, the system tends to minimise its free energy, which now depends on the type of thermal fluctuations. It turns out, that ground states with the lowest excitation frequencies are selected, because they have the largest entropy and the lowest zero–point energy. Such a mechanism, where fluctuations enhance order instead of suppressing it, is termed order by disorder and

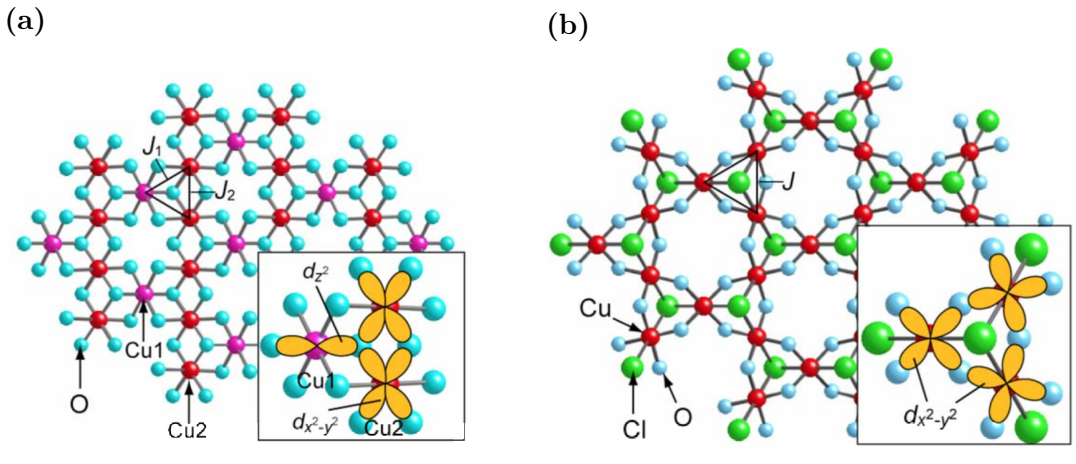

Figure 1.4: The kagome lattice in real materials, reproduced from [91]. The lattice structure of (a) Volborthite and (b) Herbertsmithite. The crystallographic lattices are drawn in the same scale. While Volborthite provides two different types of bond–interactions between Cu_1 and Cu_2 and Cu_2 and Cu_2, Herbertsmithite is claimed to be in a structurally perfect kagome lattice [92] providing isotropic nearest–neighbour exchange. The inset shows the possible arrangement of Cu $3d$ orbitals carrying unpaired electrons.

has been studied first by *Villain* in the context of Ising spins [85] and later by *Shender* [86], *Kawamura* [87] and *Henley* [88] for systems with continuous symmetries. Monte Carlo simulations showed, that the antiferromagnetic Heisenberg model on the kagome lattice develops coplanar spin order in the low–temperature limit [89, 90], while the Heisenberg model on the pyrochlore lattice does not seem to show any order by disorder mechanism [83, 84].

1.3.2 The classical Heisenberg antiferromagnet on the kagome lattice

Materials

The kagome lattice is a showcase model of frustrated magnetism. It was mentioned the first time in 1951 in a paper of *Syôzi* [93, 94], with respect to the typical shape of the Japanese bamboo basket, known as KAGO–ME. Due to its low dimensionality and simple corner sharing geometry the kagome lattice plays a crucial role in the discovery of new materials with spin liquid behaviour. Nevertheless, it took about 40 years until the kagome lattice found its first experimental realisation in the so–called "pyrochlore slab" $SrCr_8Ga_4O_{19}$, a material of decoupled kagome layers [95].

One of the most studied family of kagome antiferromagnets are the Jarosite materials, which provide properties in classical and quantum limits [96, 97, 98] with conventional long–range magnetic order and exotic unconventional order [96, 99]. The Volborthite ($Cu_3V_2O_7(OH)_2{\cdot}2H_2O$) and Herbertsmithite ($ZnCu_3(OH)_6Cl_2$) materials

(see Fig. 1.4 and [91, 100] for reviews on experimental advances on both materials) consist of kagome layers and are known to show no long range order down to 50 mK, strongly indicating to be spin liquids [101, 102]. Also, quite recently, "a family of novel materials based on a perfect two–dimensional rare–earth kagome lattice" of the form $RE_3Sb_3Mg_2O_{14}$ (RE = La, Pr, Sm, Eu, Tb, Ho) could be synthesised, and showed for many of them no sign of magnetic ordering above 2 K [103].

The antiferromagnetic Heisenberg model on the kagome lattice provides a possible model hamiltonian for several materials with kagome lattice structure. Large–S materials like $Y_{0.5}Ca_{0.5}BaCo_4O_7$ [104] (S = 3/2), deuterium Jarosite (S=5/2) [105] and the materials on the Swedenborgite lattice with Heisenberg [106] and Ising spins [107, 108] can be explained in a classical picture. Further more, results of the classical model are also relevant for low–spin models, since quantum fluctuations often play an important role just at very low temperatures, and might be overwhelmed by thermal fluctuations when heated.

Studies for more than 25 years [109, 110, 89, 111] show that the solution of the classical antiferromagnetic Heisenberg model on the kagome lattice is a challenging quest. Complex non–linear fluctuations around extensively degenerate harmonic ground states made fundamental statements about ground state properties difficult to formulate.

Thermodynamics

Early studies examined the classical antiferromagnet on the kagome lattice with nearest–neighbour interactions and n–component vector spins [109]. Hereby, each model showed its own specific behaviour, like a disordered ground state at all temperatures for the Ising model (n=1), a mapping to the three–state Potts model in the limit $T \to 0$ for the XY model and the development of a coplanar state at low temperatures for the Heisenberg model (n=3) [109].

For the Heisenberg model, it turns out, that the system energy is minimised by any configuration for which the total spin of each triangular plaquette is zero ($\sum_{i\in\triangle} \mathbf{S_i} = 0$). An extensive ground state degeneracy originates from many ways of fitting these plaquettes together, due to a rotational degree of freedom around a local exchange field. However, at low temperatures entropy selects a subset of the ground state manifold via an order by disorder mechanism and favours plaquettes aligned within a plane [89, 112, 111, 90].

Long–range ordered ground states, which are part of this manifold of planar configurations are the so–called $\mathbf{q} = 0$ and $\sqrt{3} \times \sqrt{3}$ states, as shown in Fig. 1.5 [111, 113]. Spins form an angle of 120° to each other, whereas green and red coloured spins are allowed to rotate around the local exchange axis, parallel to the blue–coloured spins, without any additional cost of energy. The $\mathbf{q} = 0$ state [Fig. 1.5(a)] shows a uniform spin chirality with repeating spin–ordering pattern on each geometric unit cell and allows for global spin excitations, traversing the entire lattice. On the other hand, the $\sqrt{3} \times \sqrt{3}$ state [Fig. 1.5(b)], is characterised by a alternating chirality, allowing for localised spin–excitations along hexagonal loops of the kagome lattice, the so–called "weather vane" mode [113, 114, 115]. Via an effective Hamiltonian approach the long–range ground state in the limit of $T \to 0$ has been proposed to select the $\sqrt{3} \times \sqrt{3}$

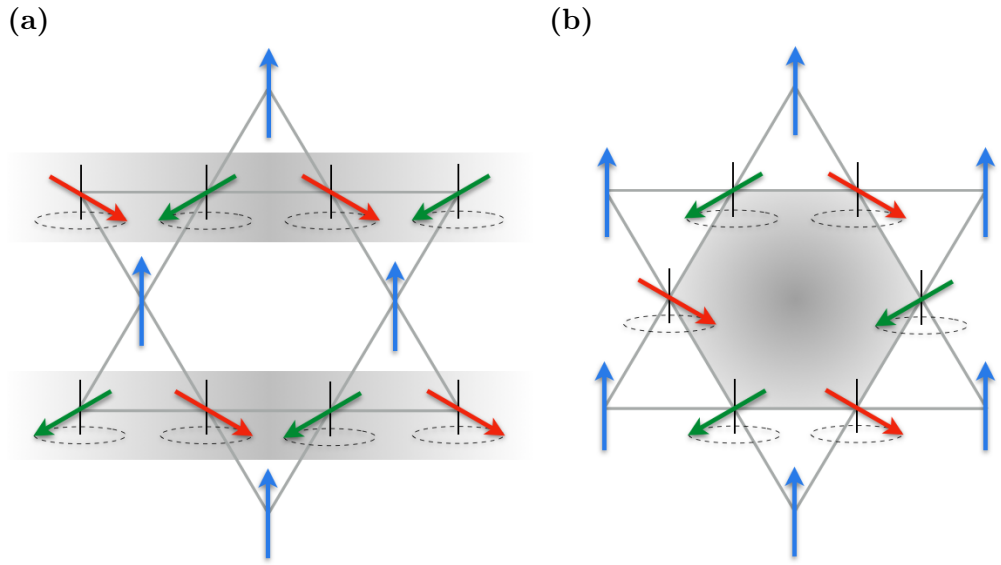

Figure 1.5: The two possible long–range ordered ground states of the classical antiferromagnetic Heisenberg model on the kagome lattice. (a) The $\mathbf{q} = 0$ state is characterised by the same chirality on each triangle with repeating spin–ordering pattern on each geometric unit cell and allows for global spin excitations. (b) The $\sqrt{3} \times \sqrt{3}$ state allows for an spin arrangement with alternating chirality, allowing for localised spin–excitations along hexagonal loops, so–called "weather vane" modes. These fluctuations cost no energy and are called weather–vane mode.

state and not the $\mathbf{q} = 0$ state [116].

Numerical techniques such as classical Monte Carlo simulations allow to investigate thermodynamic properties of the antiferromagnetic Heisenberg model on the kagome lattice at very low temperatures and large sizes, which ensures a control of finite–size effects. Simulations of the classical antiferromagnetic Heisenberg model on the kagome lattice were carried out, using the heat–bath, over-relaxation and parallel tempering method (see Chapter 2) for a system size of $N = 10800$ spins, and should be compared to published results by *Zhitomirsky* [90].

The specific heat per spin C/N, reveals three different temperature regimes: a high–temperature paramagnetic regime, a cooperative paramagnetic regime and a low–temperature coplanar state, as shown in Fig. 1.6(a). The crossover temperature into a coplanar state lays around $T_k \approx 0.004$ J and is indicated by a drop to $C/N = 11/12$, accounting for the number of zero modes in the model [see details in Appendix A.1].

Fig. 1.6(b)–(d) shows the momentum–resolved equal–time structure factor $S(\mathbf{q})$ for each temperature regime. The cooperative paramagnetic regime shows triangular, bowtie like regions of strong scattering intensity, which are connected via pinch–points, a signature of spin liquids with emergent Coulomb physics. Upon cooling the intensities are redistributed to the centres of the triangular regions with $\mathbf{q} = \{8\pi/3, 0\}$ and equivalent wave vectors. Those intensities are no Bragg peaks, since corresponding spin correlations fall off as r^{-2} [117] and the intensities grow logarithmically. The coplanar

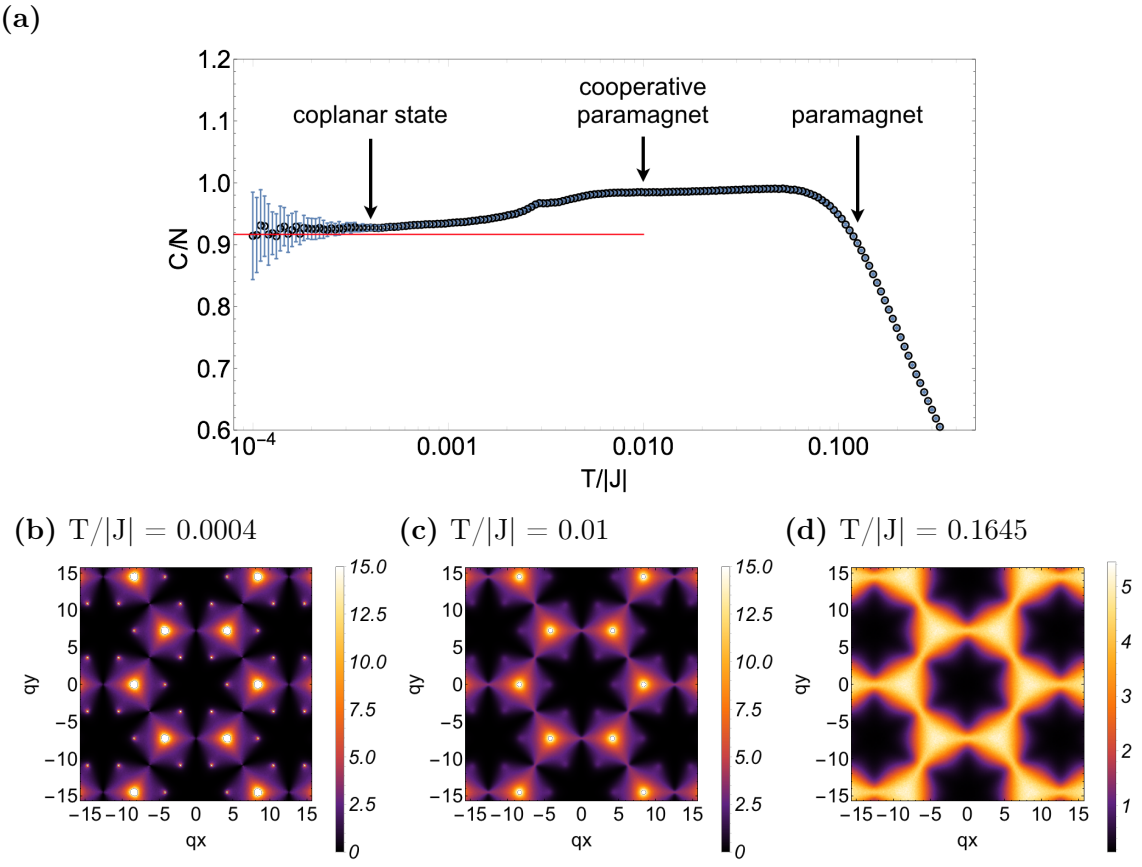

Figure 1.6: Thermodynamics in the Heisenberg model on the kagome antiferromagnet. (a) Specific heat over a wide temperature range shows three different regimes, a high–temperature paramagnetic regime, a cooperative paramagnetic regime and a low–temperature regime with a coplanar state. The red line corresponds to 11/12. Specific heat measurements were averaged over 40 independent samples, all with different random configurations. Error bars are sufficiently small down to very low temperatures ($T/|J| \sim 10^{-4}$). (b)–(d) Equal–time structure factor $S(\mathbf{q})$, within the regimes listed in (a). Results have been calculated for systems of size $N = 10800$.

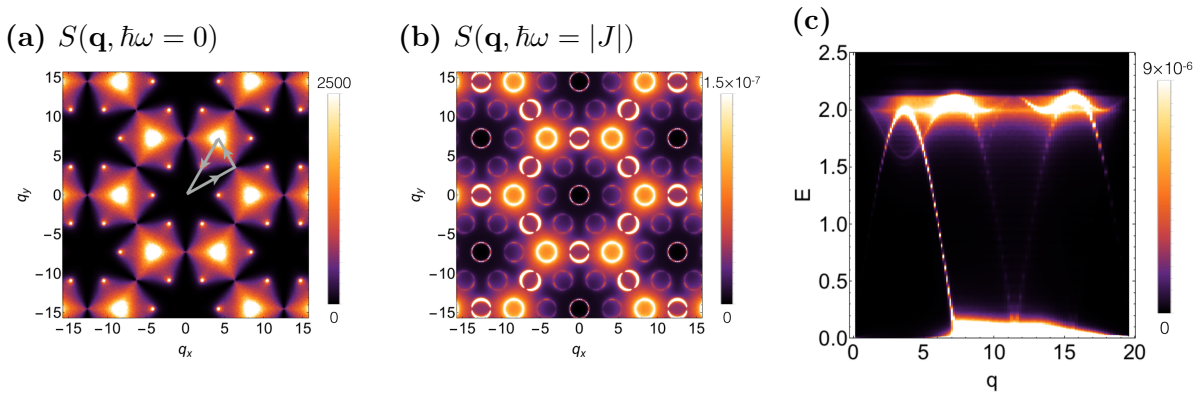

Figure 1.7: Dynamical structure factor for the Heisenberg model on the kagome antiferromagnet. (a) Energy cut at $\hbar\omega = 0$ shows a structure like in the energy–integrated structure factor S($\mathbf{q}$), shown in Fig. 1.6(b), suggesting that the largest weight lays in the zero–energy fluctuations. Diffuse scattering intensity is arranged on triangular bowtie–like features, separated via pinch–points. (b) Energy cut at $\hbar\omega = |J|$ shows rings evolving from the high–intensity regions, seen in (a), whereas "half–moon" features evolve out of pinch–points. (c) $S(\mathbf{q}, \omega)$ along the path, shown in (a), with start at $\mathbf{q} = \{0, 0\}$, shows spin waves evolving out of gapless high–intensity modes. Results have been calculated for systems of size $N = 10800$ at $T = 0.001|J|$.

state starts to develop at temperatures below T_k and is responsible for the peaks at $\mathbf{q} = \{4\pi/3, 0\}$ and vanishing pinch–points.

The consideration of the primary ordering parameter, a third–rank tensor accounting for all available symmetries in the kagome lattice provides evidence for octupolar ordering for $T \to 0$ [90], and has been concluded in later studies to be a very small dipolar–spin order with a tripled unit cell [118].

Dynamics

Classical Monte Carlo simulations, combined with molecular dynamics simulations (see Section 2.3) for a system of size $N = 10800$ spins has been used to present dynamical properties of the kagome antiferromagnetic Heisenberg model in the coplanar state at $T/|J| = 0.001$ and should be compared to results in the literature [113, 114, 119, 115]. While, in the paramagnetic regime dynamical properties show completely diffusive character, the cooperative paramagnetic regime is characterised by algebraic spin correlations mediated by dynamics of spin clusters. In the coplanar regime at very low temperatures, spin waves propagate through the system with very short life times and seem to stay strongly correlated with localised weather vane modes [115], which control the system's relaxation time scale.

The dynamical structure factor at zero frequency $S(\mathbf{q}, \hbar\omega = 0)$ [Fig. 1.7(a)] in the coplanar state looks very similar to the energy–integrated structure factor $S(\mathbf{q})$ [Fig. 1.6(b)], which suggests that the strongest intensities are coming from low–energy fluctuations. Pinch–points, located at the Brillouin zone centres evolve into "half–

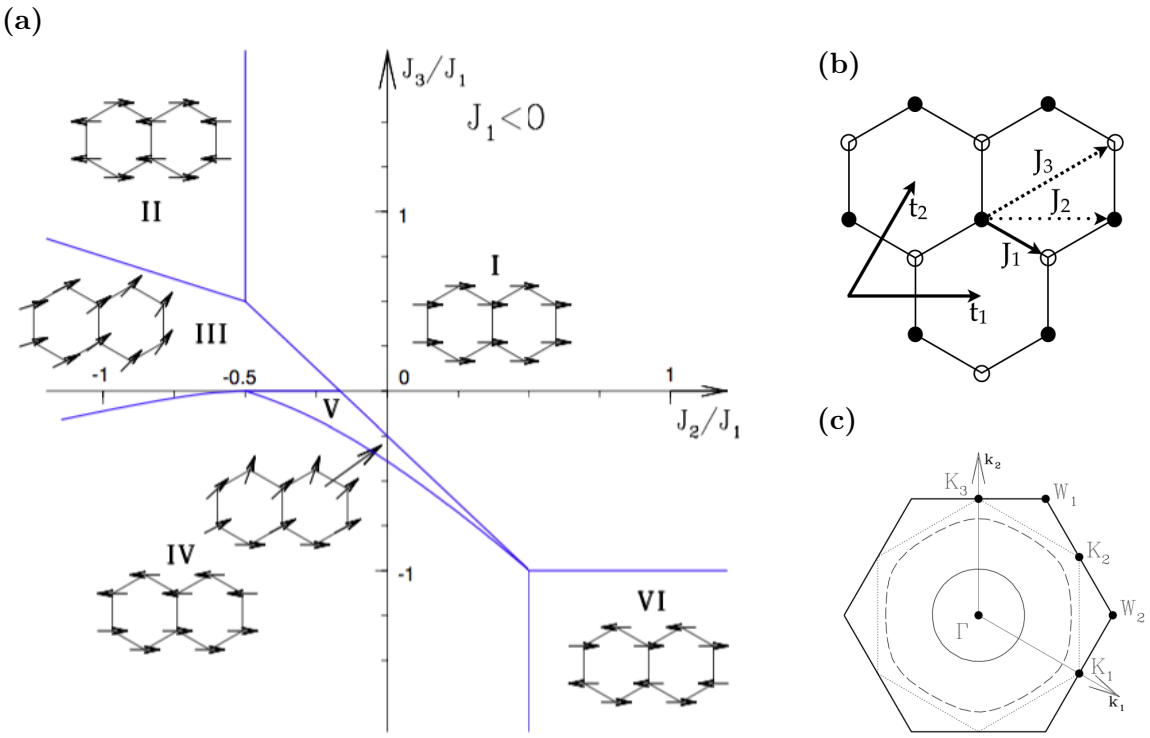

Figure 1.8: The J_1-J_2-J_3 Heisenberg model on the honeycomb lattice, reproduced from [120]. (a) T=0 phase diagram of the classical model for ferromagnetic J_1. Next to four collinear phases (I, II, IV, VI), also two spiral phases (III, V) exist. The phase boundary between phase III and V is very special, since it allows for an infinite degeneracy of spiral ground–states. (b) The bipartite honeycomb lattice with real–space lattice vectors $\mathbf{t}_1$ and $\mathbf{t}_2$ and exchange parameters J_1, J_2 and J_3. (c) Highly degenerate states on the coexistence line between phase III and V show rings in the momentum–resolved spin–spin correlations, shown for J_2 = -0.2, -0.4 and -0.5 respectively.

moon" features at higher frequency [Fig. 1.7(b)], spin–wave excitations with strongly reduced cross section along peculiar lattice directions [114]. The $S(\mathbf{q}, \omega)$ on a particular path in momentum space and function of energy [Fig. 1.7(c)] shows spin waves in form of acoustic and optical modes. However, optical modes seem to be an artefact of the simulation, and not measurable in large systems, as discussed in [119].

1.3.3 The J_1-J_2-J_3 Heisenberg model on the honeycomb lattice

Nearest–neighbour antiferromagnetic models on geometrical frustrated lattices with triangular units, like the triangular or kagome lattice, receive a lot of attention, due to the possible emergence of spin–liquid ground states.

However, spin liquids do not need to be restricted to geometric frustration only. Models with further–neighbour exchange interaction can also induce frustration, such as e.g. further–neighbour antiferromagnetic Heisenberg models on the square lattice

[121, 122, 123, 124, 82, 125].

Particular attention in this section shall be given to the J_1-J_2-J_3 Heisenberg model on the honeycomb lattice, due to its relevance for the spin liquid compound $Ca_{10}Cr_7O_{28}$, which shall be discussed detail in Chapter 5. The relevant classical Hamiltonian for this system is

$$\mathcal{H}_{\mathrm{HC}} = J_1 \sum_{\langle ij \rangle_1} \mathbf{S}_i \mathbf{S}_j + J_2 \sum_{\langle ij \rangle_2} \mathbf{S}_i \mathbf{S}_j + J_3 \sum_{\langle ij \rangle_3} \mathbf{S}_i \mathbf{S}_j \ , \tag{1.44}$$

where the first, second and third sums run respectively over the first, second and third nearest–neighbours, as depicted in Fig. 1.8(b). As evaluated in the literature [126, 120] the classical phase diagram of $\mathcal{H}_{\mathrm{HC}}$ provides a plethora of zero–temperature phases. As shown in Fig. 1.8(a) for ferromagnetic coupling $J_1 < 0$, four collinear phases (I, II, IV, VI) exist, next to two spiral phases (III, V). These spiral phases are characterised by a wave–vector $\mathbf{Q}$, such that the ground–state wave–function at position $\mathbf{R}$ on sublattice α is given as

$$\mathbf{S}_{\mathbf{R},\alpha} = S\big(\cos\left(\mathbf{Q}\cdot\mathbf{R} + \phi_\alpha\right)\mathbf{u} + \sin\left(\mathbf{Q}\cdot\mathbf{R} + \phi_\alpha\right)\mathbf{v} \big) \ . \tag{1.45}$$

Hereby, $\mathbf{u}$ and $\mathbf{v}$ are two orthogonal unit vectors defining the spin–plane and ϕ_α is an additional phase.

The phase boundary between the two spiral phases III and V is special [120], since it allows for an infinite degeneracy of spiral ground–states corresponding to:

$$\cos\left(\mathbf{Q}\cdot\mathbf{R}_1\right) + \cos\left(\mathbf{Q}\cdot\mathbf{R}_2\right) + \cos\left(\mathbf{Q}\cdot(\mathbf{R}_1 - \mathbf{R}_2)\right) = \frac{1}{8J_2^2} - \frac{3}{2} \ , \tag{1.46}$$

where $\mathbf{t_1} = \{1, 0\}$ and $\mathbf{t_2} = \{1/2, \sqrt{3}/2\}$ are the two lattice vectors of the triangular Bravais lattice. *Fouet et al.* [120] conjectured that the models on this coexistence line have a RVB spin–liquid ground–state, with a small but finite gap and strong short range order. Further more spin–spin correlations for models along this coexistence line will show a "ring" in momentum space, as presented for the in Fig. 1.8(c) for J_2 = -0.2, -0.4 and -0.5 respectively. This ring–signature has been recently measured in inelastic neutron scattering experiments on single crystals of $Ca_{10}Cr_7O_{28}$ [127] and shall be explained in detail in Chapter 5.

Similar signatures in the energy–integrated structure factor $S(\mathbf{q})$ have been identified for the classical J_1-J_2 Heisenberg model on the honeycomb lattice with antiferromagnetic ($J_1 > 0$) interactions [81] and in the J_1-J_2-J_3 Heisenberg model on the square lattice [82].

1.4 Outlook of this Thesis

This thesis is dedicated to the thermodynamic and dynamic signatures in kagome–like lattices and is divided into five Chapters. The aim of the current Chapter 1 was to generally introduce and motivate the concept of frustrated magnetism, which are impossible to study within a standard mean–field theory, as used for conventional magnets.

The next Chapter 2 discusses new methods, needed in order to access the low–temperature physics of spin liquids. The methods, used for this work are analytical Husimi tree calculations — a very powerful tool to predict thermodynamic properties in spin liquids — and classical Monte Carlo simulations, which additionally allow, combined with the numerical integration of the semiclassical–equations of motion, to access dynamical properties in spin liquids.

Chapter 3 presents thermodynamic properties and signatures of classical spin liquids on corner sharing lattices, by the use of complementary analytical Husimi tree and numerical Monte Carlo simulation techniques. The emerging phenomenon of a Curie–law crossover between a high–temperature paramagnetic and a low–temperature collective paramagnetic regime, turns out to be a powerful signature of exotic physics in classical spin liquids, and explains the difficulty for a precise estimate of the Curie–Weiss temperature in experiments.

But spin liquids do not necessarily need to show just one Curie–law crossover, as shown in Chapter 4, which discusses results for the anisotropic Ising model on the "shuriken", or "square–kagome" lattice. A rich phase diagram provides multiple disordered ground states, where low–and high–temperature regimes are less correlated than the intervening classical spin liquid, giving rise for a reentrant phenomenon in disordered systems.

Motivated by recent experiments on $Ca_{10}Cr_7O_{28}$, Chapter 5 shows dynamical properties and signatures of the nearest–neighbour Heisenberg model on the bilayer breathing kagome lattice. Hereby semi–classical molecular–dynamics simulations could be used to reproduce many features seen by inelastic neutron scattering experiments and allowed to provide a first explanation of the spin–liquid origin in $Ca_{10}Cr_7O_{28}$. Surprisingly, magnetic excitations of $Ca_{10}Cr_7O_{28}$ encode not one, but two types of spin liquids; a gapless "spiral spin liquid", with origin in an extensive ground state degeneracy, understandable by a mapping onto the J_1-J_2 honeycomb model; and, at finite energy, a "Coulombic spin–liquid" familiar from the kagome–lattice antiferromagnet.

Chapter 2

Technical Background

" Ein Kerl, der spekuliert,
Ist wie ein Tier, auf dürrer Heide,
Von einem bösen Geist im Kreis herumgeführt,
Und ringsumher liegt schöne grüne Weide."

Faust 1, Vers 1830 ff. (Mephistopheles)
Johann W. v. Goethe

In the framework of a mean–field theory, conventional magnets typically order at temperatures comparable to the exchange interaction ($T_c \sim |J|$) via spontaneous symmetry breaking. On the other hand, magnetic moments in frustrated magnets are characterised by a suppression of such an ordering mechanism down to very low temperatures, due to strong fluctuations.

Since thermodynamic and dynamic properties of systems with such behaviour are reasonably hard to access, specific analytical and numerical methods are crucial. Possible methods allowing to access those physical quantities presented in this work consider both, analytical calculations on the Husimi tree and numerical Monte Carlo simulations combined with molecular dynamics. With the help of these methods classical spin liquids can be characterised and classified due to their thermodynamic and dynamic signatures, which will be presented on specific examples for kagome–like spin systems in the following Chapters.

2.1 Husimi tree — a tool for exploring spin liquids in corner–sharing lattices

This Section will illustrate the importance and elegance of using the Husimi tree — a variation of the Bethe lattice — in order to describe the thermodynamic properties in classical spin liquids on corner sharing lattices. While this method tends to overestimate the critical temperature in systems with magnetic phase transitions, its application to classical spin liquids, which are characterised by crossovers between differently correlated regimes, provides a surprisingly good estimate of thermodynamic properties.

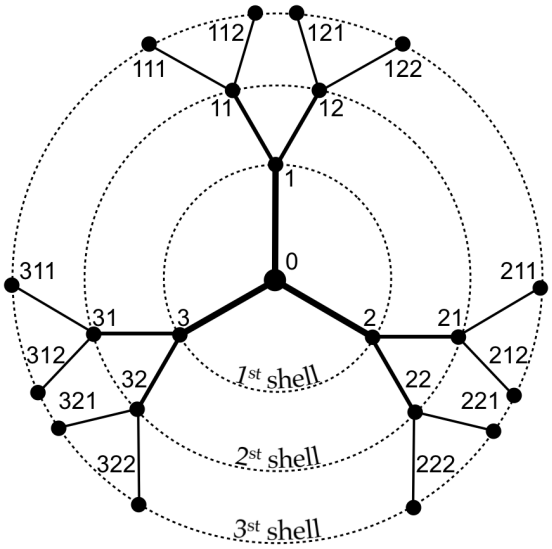

Figure 2.1: Cayley tree for coordination number q = 3 up to shell n = 3. The central site 0 is connected to q neighbours, which will form the 1^{st} shell. Connections to higher shells will happen to $q-1$ neighbouring sites. For $n \to \infty$ the Cayley tree can be considered as a Bethe lattice and allows to calculate thermodynamic properties deep within its centre at site 0.

Calculations on the Husimi tree shall be constrained to models with discrete degree of freedom, preferably Ising systems, providing the simplest model to show and understand spin liquid behaviour. An extension to Heisenberg models is generally possible, as explained in the literature [128, 129].

The Ising model has the general form

$$\mathcal{H} = J \sum_{\langle ij \rangle} \sigma_i \sigma_j - h \sum_i \sigma_i \ , \tag{2.1}$$

where the interaction J couples nearest–neighbouring spins $\langle ij \rangle$ of discrete spin value $\sigma_i = \pm 1$ on lattice sites i. Additionally, spins are coupled to an external magnetic field h, which shall be used later as a "probe" to enforce a magnetic signature in the system.

2.1.1 Bethe Lattice

Treating a system in a standard mean–field approach is usually the starting point for getting a good overview of its physical properties. However, it might not be enough to capture the important and charming physical properties, which make these complex systems so different and interesting, compared to others. Especially in the case of spin liquids unexpected physical properties are originated in long–ranged fluctuations within a disordered ground state, which simply would be ignored in a standard mean–field theory.

A solution can be found in pseudo–lattices like e.g. the Cayley tree, which is statistically simpler than the true lattice, but still includes fluctuations. Invented in the context of connected graph theory more than 100 years ago, Cayley trees still play

an important role in modern science, since exact solutions are available [55] and its application to more realistic random graphs [130] and complex networks [131, 132] is possible.

After providing a first abstract definition of a group in 1854 [133] *Arthur Cayley* introduced the concept of combinatorial graphs associated to a group in 1878 [134], which are now known as Cayley graphs. A further development of this idea in 1910 allowed *Max Dehn* to reintroduce in his lectures on group theory [135, 136] Cayley graphs under the name "Gruppenbild" (group diagram), which is nowadays known as geometric group theory. Specifically, if those Cayley graphs are simple connected undirected graphs with no cycles (no closed path), then they are called trees. [54].

A Cayley tree of order q (see Fig. 2.1 for order $q = 3$) and n shells consists of a root vertex (0), which is connected to q new vertices via q links. The first set of q vertices is named the shell $n = 1$ of the Cayley tree. In order to build shells ≥ 2 each vertex on shell 1 needs to be linked to $q - 1$ vertices from the next shell. For a Cayley tree of $q > 2$ the number of vertices on the n^{th} shell is given by

$$N_n = q(q-1)^{n-1} \,, \tag{2.2}$$

whereas the total number of vertices is

$$N = \frac{q((q-1)^n - 1)}{q-2} \,. \tag{2.3}$$

The ratio of both numbers for $n \to \infty$ is

$$\lim_{n\to\infty} \frac{N_n}{N} = \frac{q-2}{q-1} \sim 1 \,, \tag{2.4}$$

and does not approach zero, as it would be the case for a regular lattice of dimension d, which scales like $N^{-1/d}$. Furthermore, this shows that the Cayley tree in the thermodynamic limit has an infinite dimension [55], and offers unusual properties, as e.g. unconventional phase transitions for the Ising model [137, 138, 139].

Actually, the special case of a Cayley tree, which just considers local properties deep within the graph by pushing the boundaries to infinity is called the Bethe lattice, introduced in 1935 by *Hans Bethe* [52]. Using the recursive nature of the Bethe lattice allows to solve the Ising model on this pseudo–lattice exactly. Disassembling the Ising model [Eq. (2.1)] to each shell on the Bethe lattice (consider Fig. 2.1 for $n \to \infty$) leads to the following Hamiltonian:

$$\begin{aligned}
\mathcal{H} &= \mathcal{H}_0 + \sum_i^q \left(\mathcal{H}_i + \sum_j^{q-1} \left(\mathcal{H}_{ij} + \sum_k^{q-1} \left(\mathcal{H}_{ijk} + \cdots\right)\right)\right) \\
\mathcal{H}_0 &= -h\sigma_0 \\
\mathcal{H}_i &= \sigma_i(J\sigma_0 - h) \\
\mathcal{H}_{ij} &= \sigma_{ij}(J\sigma_i - h) \\
\mathcal{H}_{ijk} &= \sigma_{ijk}(J\sigma_{ij} - h) \\
&\vdots
\end{aligned} \tag{2.5}$$

The resulting partition function at the central site σ_0 can be expressed in a recursive way by considering the partition functions on each connected outer branch

$$\mathcal{Z}_0 = \sum_{\{\sigma\}} e^{-\beta\mathcal{H}} \tag{2.6}$$

$$= \sum_{\{\sigma_0\}} e^{-\beta\mathcal{H}_0} \cdot \prod_i^q \mathcal{Z}_1(\sigma_0, \sigma_i) \tag{2.7}$$

$$\mathcal{Z}_1 = \sum_{\{\sigma_i\}} e^{-\beta\mathcal{H}_i} \cdot \prod_j^{q-1} \mathcal{Z}_2(\sigma_i, \sigma_{ij})$$

$$\mathcal{Z}_2 = \sum_{\{\sigma_{ij}\}} e^{-\beta\mathcal{H}_{ij}} \cdot \prod_k^{q-1} \mathcal{Z}_3(\sigma_{ij}, \sigma_{ijk})$$

$$\vdots$$

with $\mathcal{Z}_i$ the partition function from branches originated in shell i and $\sum_\sigma$ the sum over all possible spin configurations within the lattice. Since each branch gives the same result, the partition function can be factorised

$$\mathcal{Z}_0 = \sum_{\{\sigma_0\}} e^{\beta h\sigma_0} [\mathcal{Z}_1(\sigma_0)]^q \tag{2.8}$$

and the magnetisation m on the central site σ_0 can be calculated

$$m = \langle\sigma_0\rangle = \frac{1}{\mathcal{Z}_0} \sum_{\{\sigma_0\}} \sigma_0 e^{\beta h\sigma_0} [\mathcal{Z}_1(\sigma_0)]^q \ . \tag{2.9}$$

Following the considerations from *Baxter* [55] the exact transition temperature at zero field for the Bethe lattice with an infinite number of shells is

$$J/k_B T_\mathrm{c} = \frac{1}{2} \ln\left(\frac{q}{q-2}\right) , \tag{2.10}$$

which gives a result of $T_\mathrm{c} k_B/J = 2.8854$ for the square lattice ($q = 4$). This result is much closer to Onsager's exact solution of $T_\mathrm{c} k_B/J = 2.269$ [51] than the result provided by general mean–field theory $T_\mathrm{c} k_B/J = 4$ [Eq. (1.31)].

2.1.2 Husimi tree

The Bethe lattice allows for exact solutions due to its recursive nature and is able to include fluctuations along non–intersecting links. However, it is not possible to use the Bethe lattice to solve models on geometrically frustrated lattices, since such models often need a minimum amount of short loops, e.g. loops of size 3 for models on the kagome lattice.

The Husimi tree — a cluster version of the Bethe lattice, where every vertex is replaced by a geometrically frustrated unit cell — allows to study spin liquids on

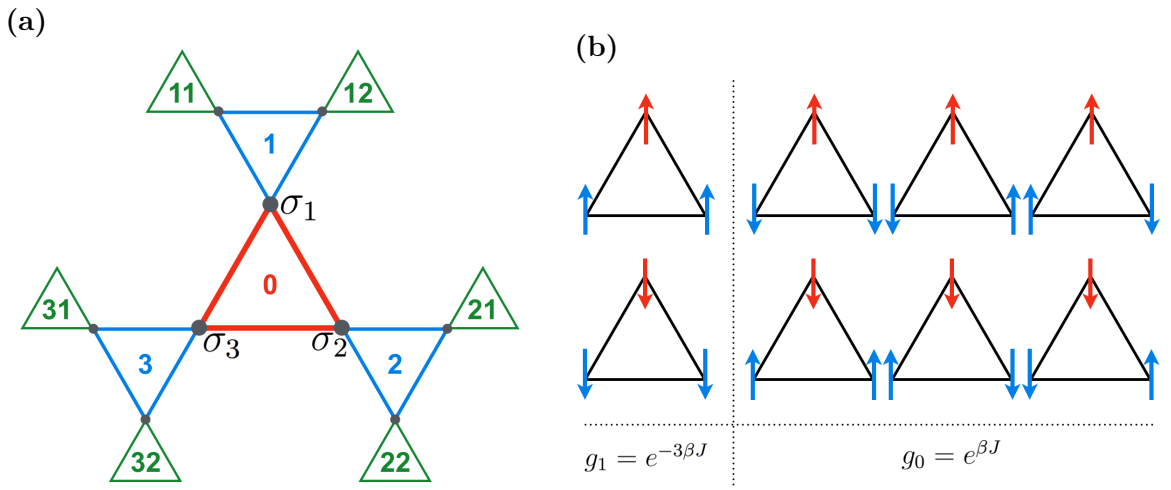

Figure 2.2: The Husimi tree on the kagome lattice. (a) Triangular unit cells arranged on the Husimi tree (Husimi Cactus). The Husimi tree is equivalent to the real kagome lattice up to its 2^{nd} shell (in green). (b) All possible spin configurations for an isolated triangular plaquette with Boltzmann weights g_0 and g_1 evaluating Eq. (2.1).

a pseudo lattice, and provided already very promising results in the past. E.g. a variational version of the Husimi tree has been used to study spin ice, a spin liquid on the pyrochlore lattice, and allowed to compute its correct zero–point entropy, which a simple mean field treatment fails to reproduce [140]. The Husimi tree also allowed to predict the isothermal magnetic susceptibilities of the spin ice materials $Dy_2Ti_2O_7$ and $Ho_2Ti_2O_7$ in a wide temperature range of $1.8 - 50$ K [141, 142], and has been applied to itinerant electron systems [143].

The definition of a Husimi tree dates back to *Harary* and *Uhlenbeck* [144], who have named it after its inventor, *Kôdi Husmi* [145] :

> "A Husimi tree is a connected graph in which no line lies on more than one cycle. It is characterised by the numbers $n_2, n_3, n_4, ...$ of lines, triangles, quadrilaterals, etc., out of which it is built up. A *pure* Husimi tree is one which consists of only one type of figure. Otherwise we speak of *mixed* Husimi trees. A pure Husimi tree consisting only of lines is a *Cayley tree*. If it consists only of triangles we will call it a *cactus*."

This definition can be applied to various other types of lattices, as e.g. done in Chapters Chapter 3 and Chapter 4 for pyrochlore, trillium and shuriken lattice.

In the following the Husimi tree calculation shall be explained on the example of the kagome lattice, shown in Fig. 2.2, where branches of nonintersecting triangular plaquettes are extending from the central unit (drawn in red). The definition for the magnetisation on the Bethe lattice [Eq. (2.9)] can be extended to the Husimi tree, by replacing every single vortex is by a triangular plaquette. The magnetisation on one

site within this triangular plaquette can be calculated, as

$$\langle\sigma_1\rangle = \frac{1}{\mathcal{Z}_0}\sum_{\{\sigma_1,\sigma_2,\sigma_3\}}\sigma_1\left(\prod_{\langle ij\rangle} g_{ij}\right)\left(\prod_{i=1}^{3}\alpha_i\right)\cdot\mathcal{Z}_1(\sigma_1)\mathcal{Z}_1(\sigma_2)\mathcal{Z}_1(\sigma_3)\;, \tag{2.11}$$

$$\mathcal{Z}_0 = \sum_{\{\sigma_1,\sigma_2,\sigma_3\}}\left(\prod_{\langle ij\rangle} g_{ij}\right)\left(\prod_{i=1}^{3}\alpha_i\right)\cdot\mathcal{Z}_1(\sigma_1)\mathcal{Z}_1(\sigma_2)\mathcal{Z}_1(\sigma_3)\;, \tag{2.12}$$

where $\prod_{\langle ij\rangle}$ is a product over the nearest–neighbour spins within the central triangular plaquette. $\mathcal{Z}_0$ and $\mathcal{Z}_1$ are the partition functions on sites in shell 0 (red) and shell 1 (blue), respectively. The Boltzmann weights accounting for the energies from the bond–interaction J and the coupling to the external magnetic field h are written as

$$g_{ij} = e^{-\beta J\sigma_i\sigma_j}\;, \tag{2.13}$$

$$\alpha_i = e^{\beta h\sigma_i}\;. \tag{2.14}$$

For a given triangle the Boltzmann factor becomes $g_0 = e^{\beta J}$ and $g_1 = e^{-3\beta J}$ as illustrated in Fig. 2.2(b). Eq. (2.11) gives explicitly for the kagome lattice

$$\langle\sigma_1\rangle = \frac{g_0(Y_1 - Y_1^2) + g_1(1 - Y_1^3)}{3g_0(Y_1 + Y_1^2) + g_1(1 + Y_1^3)}\;, \tag{2.15}$$

where we introduced the ratio between the partition function of a spin on shell n, pointing $\uparrow$ ($\sigma = 1$) and a spin pointing down $\downarrow$ ($\sigma = -1$) [55] as

$$\frac{\mathcal{Z}_n^{\downarrow}}{\mathcal{Z}_n^{\uparrow}} = Y_n\; e^{2\beta h}\;. \tag{2.16}$$

Since shell 0 is located in the centre of the Husimi tree, far away from its boundary, one can assume the ratios of the partition function between shell 0 and 1 to be equal in the thermodynamic limit

$$Y_0 = Y_1 \equiv Y\;. \tag{2.17}$$

In absence of an external magnetic field $Y = 1$, since the disordered system does not prefer any spin direction. However, small external magnetic fields h cause a perturbation ϵ away from this value, so that

$$Y = 1 - \epsilon\;, \tag{2.18}$$

which can be used together with Eq. (2.17) and Eq. (2.16) to obtain ϵ in first order approximation

$$\epsilon = 2\beta h\;\frac{3g_0 + g_1}{5g_0 - g_1}\;. \tag{2.19}$$

Please note, that the first–order expansion in h is sufficient to compute the magnetic susceptibility, since higher–order terms vanish as $h \to 0$. Introducing Eq. (2.19) into Eq. (2.15) gives the temperature–dependent magnetisation of σ_1

$$\langle\sigma_1\rangle = \beta h\;\frac{g_0 + 3g_1}{5g_0 - g_1}\;. \tag{2.20}$$

Knowing the partition function $\mathcal{Z}_0$ and the magnetisation $\langle\sigma_1\rangle$ allows to calculate further thermodynamic observables, like energy, specific heat, entropy and susceptibility. Therefore, the Husimi tree is a very powerful analytical method to predict thermodynamic properties of spin liquids over a wide range of temperatures. Its generality to other spin liquids on corner–sharing lattices has been investigated and discussed for the topic of a "Curie–law crossover" in Chapter 3 and the specific example of the shuriken lattice in Chapter 4.

2.2 Monte Carlo simulations for spin systems

The goal of this Section is to introduce the very powerful and widely used Monte Carlo method, a sampling algorithm, famous for simulating phenomena with a large number of coupled degrees of freedom. Due to its simple key concepts and ability to adapt to a very large range of problems, it is used in many different disciplines as a computational algorithm for numerical optimisation, finance and business, climate change, artificial intelligence, engineering, computational biology, and of course statistical physics [146].

Here, the basic concepts for using Monte Carlo algorithms, to draw states from a thermal distribution (Boltzmann distribution), will be explained by an application to spin systems with discrete Ising ($\mathbb{Z}_2$), and continuous Heisenberg ($\mathbb{O}(3)$) symmetry. It turns out that the implementation of the single–spin flip Metropolis Monte Carlo algorithm for conventional magnets is rather straight forward, but allows for new technical challenges in the application on spin liquids. Complex physical phenomena, like topological phase transitions, order by disorder effects or the absence of any order down to the lowest temperatures do not allow this algorithm to properly thermalise the system anymore, making the implementation of advanced algorithms like cluster or parallel tempering updates necessary.

Detailed explanations about equilibrium statistical physics and different Monte Carlo algorithms for various applications can also be found in the literature [53, 147, 148, 149].

2.2.1 A fundamental sampling method

To fully understand a complex system with a very large number of unknown quantities can be a very difficult, or even impossible task. For example 1 litre of air at room temperature and atmospheric pressure consists of 3×10^{22} molecules, all moving and colliding with each other and with the walls of a container, following their individual equations of motion [149]. Solving all equations of motion for so many interacting particles is basically impossible, which is why we need to rely on statistical sampling techniques by calculating physical quantities of many independent, well–behaved small ensembles, whose averaged properties allow us to make predictions for the entire system.

Markov process, Ergodicity and Detailed Balance

Temperature is one of the most important ingredients in Monte Carlo simulations, since it considers a canonical ensemble, which consists of stochastically–distributed

micro states coupled to an external heat bath. The energy coming from the heat bath can be exchanged with the system energy and allows for transition processes between different micro states. The time evolution of such micro states is directly coupled to their transition processes, and can very generally be described by the master equation:

$$\frac{d\omega_\mu}{dt} = \sum_\nu \Big[\omega_\nu(t)P(\nu \to \mu) - \omega_\mu(t)P(\mu \to \nu)\Big] \ . \tag{2.21}$$

Hereby, the time evolution of the occupation probability $\omega_\mu(t)$ provides a measure of how likely it is to find the system in a micro state μ at time t. $\omega_\mu(t)$ simultaneously obeys the sum rule:

$$\sum_\mu \omega_\mu(t) = 1 \tag{2.22}$$

for all t, since the system must be in a given state at all times. The transition probability from state μ to ν is described by $P(\mu \to \nu)$, where μ and ν do not necessarily have to be two different states. To allow for a proper statistical sampling, the system needs to be "memoryless". Therefore, the transition rates $P(\mu \to \nu)$ have to satisfy the fundamental condition of a Markov process, which means that they should not vary over time and should only depend on the properties of the current states μ and ν, and not on any other state the system passed through before. Also, the algorithm needs to provide ergodicity throughout the whole simulation, making the whole phase space accessible in a finite amount of time. Knowing the values for the occupation probabilities $\omega_\mu(t)$, we a priori know their equilibrium values by waiting long enough in time:

$$p_\mu = \lim_{t\to\infty} \omega_\mu(t) \ . \tag{2.23}$$

If the system reached in its time evolution an equilibrium state, then the occupation probabilities are not time dependent anymore:

$$\frac{d\omega_\mu}{dt} = 0 \ . \tag{2.24}$$

The right side of the master equation [Eq. (2.21)] can therefore be evaluated as:

$$\sum_\nu p_\nu P(\nu \to \mu) = \sum_\nu p_\mu P(\mu \to \nu) \tag{2.25}$$

whereas the sum over all incoming and outgoing transitions needs to be equal. For what follows, the sufficient, but not necessary condition of detailed balance

$$p_\nu P(\nu \to \mu) = p_\mu P(\mu \to \nu) \tag{2.26}$$

has been chosen to satisfy Eq. (2.25). This condition states that all individual incoming transitions $(\nu \to \mu)$ equals their opposed outgoing transition $(\mu \to \nu)$. Algorithms in general do not necessarily need to be constrained to this condition and can use more complex transition processes. One example is the Event Chain algorithm, which breaks detailed–balance, but satisfies global balance and can outperform conventional Monte Carlo algorithms [150, 151, 152, 153].

Metropolis Algorithm

Gibbs showed in 1902, by connecting statistical mechanics with thermodynamics [154], that the equilibrium occupation probabilities p_μ of systems in thermal equilibrium with a reservoir at temperature T follow the Boltzmann distribution:

$$p_\mu = \frac{1}{\mathcal{Z}} e^{-E_\mu / k_B T} \,, \tag{2.27}$$

where k_B has been denoted as the Boltzmann constant and E_μ as the energy of the system in state μ. In the following, the inverse temperature $(k_B T)^{-1}$ will be written as β, while the partition function

$$\mathcal{Z} = \sum_\mu e^{-\beta E_\mu} \tag{2.28}$$

operates as a normalisation parameter.

By introducing Eq. (2.27) into Eq. (2.26) one obtains:

$$\frac{P(\mu \to \nu)}{P(\nu \to \mu)} = \frac{p_\nu}{p_\mu} = e^{-\beta(E_\nu - E_\mu)} \,, \tag{2.29}$$

where the ratio of transition probabilities is expressed by the Boltzmann weight of the energy differences between two micro states μ and ν. In general these transition probabilities can be set to any arbitrary values, as long as they satisfy the condition in Eq. (2.29). However the efficiency of the algorithm depends on the choice of those values. Metropolis found that the efficiency of this algorithm is the highest, if the larger of the two transition probabilities gets the largest possible value, namely 1, and then adjust the other one in order to satisfy the constraint. Therefore the most efficient algorithm, which satisfies Eq. (2.29) will consider the constraint:

$$P(\mu \to \nu) = \begin{cases} e^{-\beta(E_\nu - E_\mu)} & \text{if } E_\nu - E_\mu > 0 \\ 1 & \text{otherwise.} \end{cases} \tag{2.30}$$

In other words, if a new state with a lower energy compared to the previous one has been selected, then the algorithm should always accept the transition to it. If it has a higher energy, then the transition is just accepted with the probability given in Eq. (2.30). This specific algorithm is called the Metropolis algorithm, pioneered by *Metropolis* and coworkers in their work on two–dimensional rigid–sphere systems in 1953 [155].

2.2.2 Measurement of thermodynamic observables

The laws of thermodynamics are omnipresent in our daily life and occupied researchers for more than 200 years by studying the efficiency of steam engines by e.g. *Nicolas Léanard Sadi Carnot* in 1824 [156] and *M.C. Clapeyron* in 1834 [157]. One of the charm of thermodynamics comes from its connection to statistical mechanics, which is the key in order to learn something about thermodynamic properties of spin liquids, simulated via numerical Monte Carlo techniques.

This section will review just a small portion of thermodynamical relations. The interested reader might refer to the book of *Michael Plischke and Birger Bergersen*

"Equilibrium Statistical Physics" [53] or "Monte Carlo Methods in Statistical Physics" by *Newman and Barkema* [149], in order to get a more profound insight into the topic.

Once a system has been thermalised one needs to extract physical observables like energy E, magnetisation M, or other system dependent order parameters to compare to experimental results. Hereby, the differential of the system energy is expressed as:

$$dE = \delta Q - \delta W \ , \tag{2.31}$$

where δQ is the heat, and δW is the infinitesimal change of work added to the system. For reversible processes the second law of thermodynamics states that:

$$\delta Q = T \ dS \ , \tag{2.32}$$

with S the entropy of the system. If the work W is performed by a coupling of the magnetisation $\mathbf{M}$ to the external magnetic field $\mathbf{h}$, then the internal energy for a canonical ensemble will look like:

$$dE = T \ dS - \mathbf{h} \ d\mathbf{M} \ . \tag{2.33}$$

A canonical ensemble hereby allows fluctuations about the fixed mean energy $\langle E \rangle$, but does not allow the number of particles and volume of the system to fluctuate.

$$\langle E \rangle = const \ , \qquad N = const \ , \qquad V = const \ , \tag{2.34}$$

Energy and Magnetisation

Fluctuations in energy and also in magnetisation are used to measure thermodynamical response functions such as the specific heat C_h at constant magnetic field $\mathbf{h}$ and the magnetic susceptibility χ.

$$C_h = \left(\frac{\partial \langle E \rangle}{\partial T} \right)_h \ , \tag{2.35}$$

$$\chi = \left(\frac{\partial \langle M \rangle}{\partial h} \right)_{h \to 0} \ . \tag{2.36}$$

Considering the fluctuation in energy from the mean value, given by

$$\Delta E = E - \langle E \rangle \ , \tag{2.37}$$

one can calculate the variance of the energy:

$$\langle \Delta E^2 \rangle = \langle E^2 - 2E\langle E \rangle + \langle E \rangle^2 \rangle \tag{2.38}$$

$$= \langle E^2 \rangle - \langle E \rangle^2 \ . \tag{2.39}$$

The connection between thermodynamical observables to statistical quantities, like the equilibration occupation probability p_μ, via the Boltzmann distribution [Eq. (2.27)] allows to express the mean system energy by the partition function $\mathcal{Z}$ [Eq. (2.28)]

$$\langle E \rangle = \sum_i p_\mu E_\mu = -\frac{1}{\mathcal{Z}} \left(\frac{\partial \mathcal{Z}}{\partial \beta} \right)_h = -\left(\frac{\partial}{\partial \beta} \ln \mathcal{Z} \right)_h \ , \tag{2.40}$$

$$\langle E^2 \rangle = \sum_i p_\mu E_\mu^2 = \frac{1}{\mathcal{Z}} \left(\frac{\partial^2 \mathcal{Z}}{\partial \beta^2} \right)_h \ . \tag{2.41}$$

This is an important point, since the fluctuations in energy can be connected to the specific heat C_h by using Eq. (2.39):

$$\langle \Delta E^2 \rangle = \frac{1}{\mathcal{Z}} \left(\frac{\partial^2 \mathcal{Z}}{\partial \beta^2} \right)_h + \frac{1}{\mathcal{Z}^2} \left(\frac{\partial \mathcal{Z}}{\partial \beta} \right)_h^2 = \frac{\partial}{\partial \beta} \left(\frac{\partial}{\partial \beta} \ln \mathcal{Z} \right)_h \tag{2.42}$$

$$= -\frac{\partial}{\partial \beta} \langle E \rangle_h = k_B T^2 C_h \ , \tag{2.43}$$

making it possible to express C_h in terms of the mean and mean–square values of the energy E.

$$C_h = \frac{1}{k_B T^2} \left[\langle E^2 \rangle - \langle E \rangle^2 \right] , \tag{2.44}$$

which can be easily extracted as a byproduct from the Monte Carlo simulations.

In the same spirit the susceptibility χ can be connected to the fluctuations of the corresponding order parameter under consideration, here the magnetisation M

$$\chi = \frac{1}{k_b T} \left[\langle M^2 \rangle - \langle M \rangle^2 \right] . \tag{2.45}$$

The relative fluctuations in energy on the scale of its mean may be written as:

$$\frac{\sqrt{\langle \Delta E^2 \rangle}}{\langle E \rangle} = \frac{\sqrt{k_B T^2 C_h}}{\langle E \rangle} \sim \frac{1}{\sqrt{N}} \ , \tag{2.46}$$

since C_h and E are extensive variables and explicitly depend on the number of particles in the system. Eq. (2.46) is a consequence of the central limit theorem. For Avogadro–sized assemblies $N \sim 10^{24}$ the fluctuations in energy will be about $\sim 10^{-12}$, which is smaller than any experimental precision could provide. Actually, energy fluctuations will vanish in the thermodynamic limit for $N \to \infty$, merging the physical properties for the canonical ensemble to those of the micro canonical ensemble.

Fluctuations play a central role in Monte Carlo simulations of finite sized systems, and can be treated efficiently in multi–canonical sampling methods, like the parallel tempering method, which shall be explained in more detail in Section 2.2.5.

Entropy

Next to the fluctuations in energy and magnetic order parameter, the entropy S is also very important for studying spin liquids. The entropy relates to the specific heat as:

$$C_h = T \left(\frac{\partial S}{\partial T} \right)_h \ , \tag{2.47}$$

leading to a solution for the absolute entropy $S(T)$ at temperature T by integrating the specific heat C_h over temperature T

$$S(T) = S(T_0) + \int_{T_0}^{T} \frac{C_h}{T} dT \ . \tag{2.48}$$

Hereby the integration constant $S(T_0)$ should be set to a known entropy value at temperature T_0.

Since Monte Carlo simulations are done over a set of discrete temperature values, one needs to perform the numerical integration in form of a sum

$$S\left(\frac{T_j + T_{j+1}}{2}\right) = S(T_0) + \sum_{i=0}^{j} \frac{C_i + C_{i+1}}{T_i + T_{i+1}} \left(T_{i+1} - T_i\right) , \tag{2.49}$$

in order to extract the entropy value between two given temperatures. Hereby, the specific heat C_i is measured at the corresponding temperature value T_i on the temperature grid, individually chosen for the simulation. Of course the temperature values should be chosen wisely, such that numerical errors are minimised and possible sharp, or singular features as seen at phase transitions are taken into account as well.

As a remark, the calculation of the entropy S as shown in Eq. (2.49) is not applicable for classical Heisenberg systems (see Section 2.2.4) since fluctuations of spins will scale with temperature even down to $T \to 0^+$.

Correlation Function

The correlation in real space of two spins at site i and j is expressed by the two–point correlation function

$$G_{ij} = \langle \mathbf{S}_i \mathbf{S}_j \rangle - \langle \mathbf{S}_i \rangle \langle \mathbf{S}_j \rangle \tag{2.50}$$

$$= \frac{1}{\beta^2} \frac{\partial^2 \log \mathcal{Z}}{\partial h_i \partial h_j} . \tag{2.51}$$

Since the system is translationally invariant, G_{ij} only depends on the displacement $\mathbf{r}$ between sites i and j, and not exactly on where the sites are. One can calculate the correlation function averaged over all sites on the lattice

$$G(\mathbf{r}) = \frac{1}{N} \sum_i G(\mathbf{r}_i, \mathbf{r}_i + \mathbf{r}) \tag{2.52}$$

$$= \frac{1}{N} \sum_{\substack{ij \text{ with} \\ \mathbf{r}_j - \mathbf{r}_i \,=\, \mathbf{r}}} \left[\langle \mathbf{S}_i \mathbf{S}_j \rangle - \langle \mathbf{S}_i \rangle \langle \mathbf{S}_j \rangle\right] . \tag{2.53}$$

Systems can show exponential or algebraic decay of correlations, a property used to classify spin liquids in a broad sense [2].

2.2.3 The Ising model

The Ising model is one of the simplest and best–studied statistical mechanics models. Introduced in his PhD, *Ernst Ising* used this model (later named after him, by *Rudolf Peierls* [158]) on a one–dimensional spin chain in order to understand ferromagnetism [159]. It was *Lars Onsager* in 1944 [51], who solved this statistical model analytically on the square lattice, and provided an exact solution in its thermodynamic limit. Not just important as a statistical model, it also allows to predict physical properties of real materials in two (e.g. $CoCs_3Cl_5$ and $CoCs_3Br_5$ [160]) and three-dimensions (e.g. $DyPO_4$ [161]).

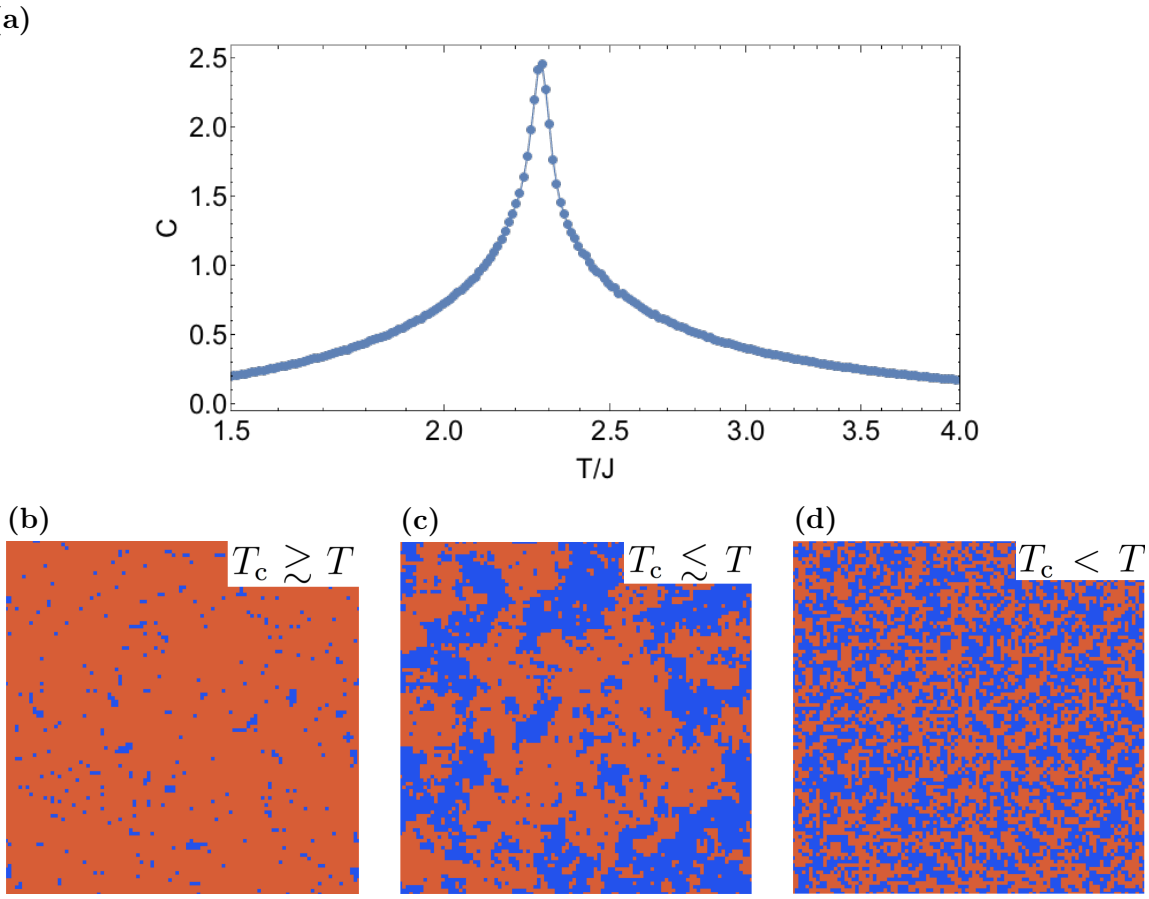

Figure 2.3: Monte Carlo simulations for the Ising model (100×100 **sites) on the square lattice.** (a) shows the specific heat with a global maximum at $T_c/J \approx 2.27$, comparable to the exact result ($T_c/J = 2.269$) by Onsager [51]. Snap–shots of the spin configuration are seen in (b) at $T_c \gtrsim T = 2J$ below the phase transition, (c) $T_c \lesssim T = 2.4J$ above the phase transition and (d) $T_c < T = 5J$ far above the phase–transition temperature T_c. Blue corresponds $\sigma_i = +1$, while orange corresponds $\sigma_i = -1$ at site i. Simulations were performed with local spin–flip Metropolis updates and parallel tempering, 10^5 steps for equilibration, annealing and statistical averaging.

The Ising model describes a magnet, where magnetic moments σ_i are placed on lattice sites i and are able to take two values: $+1$ or -1. If there are N sites on this lattice, then the total number of possible states will be 2^N and the system energy will be described by the following Hamiltonian:

$$\mathcal{H} = \sum_{\langle ij \rangle} J_{ij} \sigma_i \sigma_j - h \sum_i \sigma_i \ , \tag{2.54}$$

where J_{ij} represents the bond–dependent exchange energy between coupled spins $\langle ij \rangle$, and h is an external magnetic field.

Results from Monte Carlo simulations of the ferromagnetic Ising model ($J_{ij} = J = -1$) [Eq. (2.54)] are shown in Fig. 2.3 for the square lattice with $N = 10000$ sites. Fig. 2.3(a) shows the specific heat C_h [Eq. (2.44)] close to the phase transition temperature T_c with snapshots of spin configurations Fig. 2.3(b) below, (c) in the vicinity, and (d) above T_c.

Numerical Implementation

To numerically simulate the Ising model with classical Monte Carlo simulations, one needs to define an array of N lattice sites, with an Ising variable $\sigma_i = \pm 1$, connected with periodic, helical, or open boundary conditions. A random distribution of these spins on each site could be a starting configuration for the algorithm. The algorithm will randomly visit sites i in the lattice and evaluates the Metropolis sampling condition, stated in Eq. (2.30) by calculating the energy E_μ over all neighbouring bonds for the initial spin and E_ν for a new spin, which is flipped. The system energies for both configurations can be compared by using Eq. (2.54)

$$E_\nu^{-\sigma_i} - E_\mu^{\sigma_i} = \pm 2 \left(\sum_\delta J_{i,\delta} \, \sigma_\delta - h \right) , \tag{2.55}$$

where the difference of the total energy of both systems just depends on the change in energy on the bonds, connecting the flipped spin σ_i to its neighbouring spins σ_δ. If the new system energy is reduced in this new configuration, then the spin flip will be accepted. On the other hand, if the system energy increases, then the spin flip is just accepted, if the Boltzmann probability, stated in Eq. (2.30) allows it. The verification in that manner for N randomly chosen sites of the lattice is called one Monte Carlo step.

Random Numbers

The evaluation of the Metropolis argument in Eq. (2.30) takes place with a numerically produced random number $R_0 \in [0, 1]$. If the random number R_0 is hereby smaller than the Boltzmann weight, which corresponds to the energy difference between state μ and ν, then the transition is accepted.

The question is, how does a computer — probably one of the most deterministic machines, produced by humans — provide statistically independent random numbers? In this context, one relies on the use of random number generators, a piece of computer

(a)

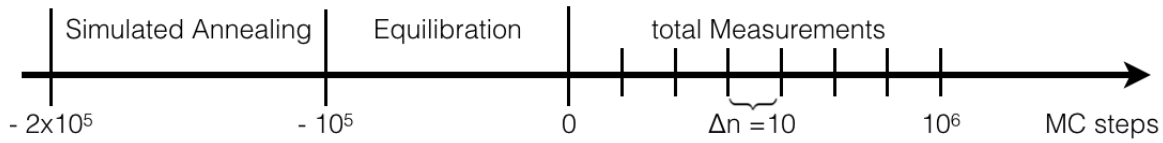

(b)

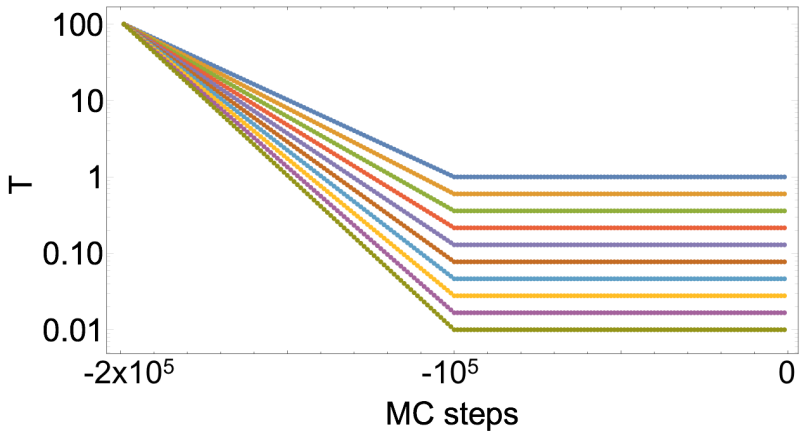

Figure 2.4: Monte Carlo scheme and simulated annealing. (a) Example scheme of a Monte Carlo (MC) simulation. The actual sampling for each replica starts after simulated annealing and equilibration. Thermodynamic properties are stored after Δn MC steps to account for statistically independent samples. (b) Example of temperature distributions per replica and MC step. The first 10^5 MC steps account for simulated annealing, while the next 10^5 MC steps are used to equilibrate the system at the fixed target temperature.

code, able to produce a sequence of statistically uncorrelated numbers. The length of this sequence is usually related to the periodicity of a random number generator and needs to be reasonably large to allow for uncorrelated statistical sampling in Monte Carlo simulations [162].

Thermalisation

Thermalisation in Monte Carlo simulations is a very important process, since the quality of the obtained results highly depends on the proper equilibration of the system. A sketch of the whole Monte Carlo sampling process can be seen in Fig. 2.4(a).

In order to "cool" a system down to low temperatures, one can, as in a real experiment, quench the system, by setting the temperatures for each replica directly to the target temperature. Starting from a decorrelated high–temperature paramagnetic phase, the system will "rush" through possible phase transitions and enter into a low–temperature correlated phase. Not allowing the system to thermalise within this broad temperature regime might cause difficulties for finding equilibrated replica. A useful

method for avoiding such effects is simulated annealing, which allows the system to adiabatically cool down to its target temperature. The distributions of temperature values are hereby chosen in any convenient way, as e.g. by a logarithmic distribution, shown in Fig. 2.4(b).

After the system reached its target temperature, one should allow the algorithm to further equilibrate the system by waiting a sufficiently large amount of Monte Carlo steps before starting the actual measurements. The actual measurement of physical observables happens after Δn MC steps in order to allow the system to decorrelate and provide statistically independent results. However, every system shows different correlation effects (especially at low T) and Δn can range from a few, up to many MC steps. To know if a simulation provides decorrelated samples one needs to consider the autocorrelation function.

Systems with phase transitions, show a diverging correlation length in the vicinity of the phase transition temperature T_c, as shown in the context of Landau theory of phase transitions in Section 1.2.2. Close to T_c the correlation length will be in the order of the length of the cluster, used for the simulation, producing large domains of equal magnetisation, separated by domain walls [Fig. 2.3(c)]. Since single–spin flip algorithms are not capable of flipping whole clusters of spins, thermalisation close to the transition temperature becomes difficult, and is called critical slowing down. However, advanced algorithms like cluster–flipping methods, as the Wolff algorithm [163] or the Swendsen–Wang algorithm [164], are able to flip large regions of spins with same magnetisation and can remove the problem of critical slowing down entirely.

Autocorrelation Function

In order to make a statement about the number of Monte Carlo steps Δn between each measurement [see Fig. 2.4(a)], one should consider the time-displaced autocorrelation function $G(t)$, a measure of the correlation between the spin configurations after a different number of Monte Carlo steps,

$$G(t) = \int dt' [m(t') - \langle m \rangle][m(t'+t) - \langle m \rangle] \tag{2.56}$$

$$= \int dt' [m(t')m(t'+t) - \langle m \rangle^2] \,, \tag{2.57}$$

where $m(t)$ is the instantaneous value of the system magnetisation at time t and $\langle m \rangle$ is the average value of it. This correlation time strongly depends on the system under consideration and might range between several Monte Carlo steps in simple models and up to infinity for e.g. spin glass models [72, 165, 73]. In absence of freezing, the autocorrelation is expected to decrease exponentially like

$$G(t) \sim e^{-t/\tau} \,, \tag{2.58}$$

where τ represents the correlation time, a measure of the minimal time window necessary to allow for two statistical independent samples.

2.2.4 The Heisenberg model

The Ising model can be generalised by increasing the degree of freedom of the spins on the lattice, as done for example in the Potts model [166]. Pushing the limit of allowed degrees of freedom up to infinity can be described, to some extend, by the classical Heisenberg model, where spins are allowed to point in any direction in space.

In the classical Heisenberg model spins at position i are treated as vectors with

$$\mathbf{S}_i \in \mathbb{R}^3 \quad \text{and} \quad |\mathbf{S}_i| = 1 \,, \tag{2.59}$$

where the spin length is set to be unity. The Hamiltonian evaluating the total energy of interacting spins on a lattice is

$$\mathcal{H} = \sum_{\langle ij \rangle} J_{ij}\, \mathbf{S}_i \cdot \mathbf{S}_j - \mathbf{h} \sum_i \mathbf{S}_i \,, \tag{2.60}$$

where J_{ij} represents the exchange energy between coupled spins $\langle ij \rangle$ and $\mathbf{h}$ the external magnetic field.

The infinite number of allowed spin directions makes the evaluation of this Hamiltonian with Monte Carlo simulations much more difficult than in the simple Ising model. At low temperatures Heisenberg systems might show unconventional phase transitions into partial ordered states [167, 168, 169], chiral–ordered states [170] or disordered states with decreased entropy, as in the case of the antiferromagnetic Heisenberg model on the kagome lattice (see Section 1.3.2). Hereby, the updating process of the single–spin flip Metropolis algorithm [Eq. (2.30)] is not able to provide sufficient spin–flip acceptance ratios anymore. Spins will mostly be stuck in a frozen configuration, which will prevent the algorithm from a proper sampling over a large amount of different ensembles and does not guarantee sufficient statistics. In the following, after presenting the familiar single–spin flip method by choosing a random vector uniformly distributed on a sphere, different algorithms are presented, which will help to recover sufficient sampling statistics at temperature regions, where the simple single–spin flip algorithm is not reliable anymore.

Uniformly distributed points on a sphere

In order to perform single or multiple–spin updates in Monte Carlo simulations for Heisenberg models one needs to ensure spins uniformly distributed on a sphere. To select cartesian coordinates x, y and z from uniform distributions $x, y, z \in [-1, 1]$ and normalising them such that $x^2 + y^2 + z^2 = 1$ will be incorrect, since points will be gathered near the edges and corners of the corresponding cube [see Fig. 2.5(a) and Fig. 2.5(b)]. In a similar spirit, selecting spherical coordinates ϕ and θ from uniform distributions $\phi \in [0, 2\pi)$ and $\theta \in [0, \pi]$ will be incorrect as well, since the area element $d\Omega = \sin\theta \; d\phi \; d\theta$ is a function of the azimuthal angle θ. To overcome this issue one can choose the following new set of coordinates:

$$\begin{aligned} x &= \sqrt{1 - u^2} \cos\phi \,, \\ y &= \sqrt{1 - u^2} \sin\phi \,, \\ z &= u \,, \end{aligned} \tag{2.61}$$

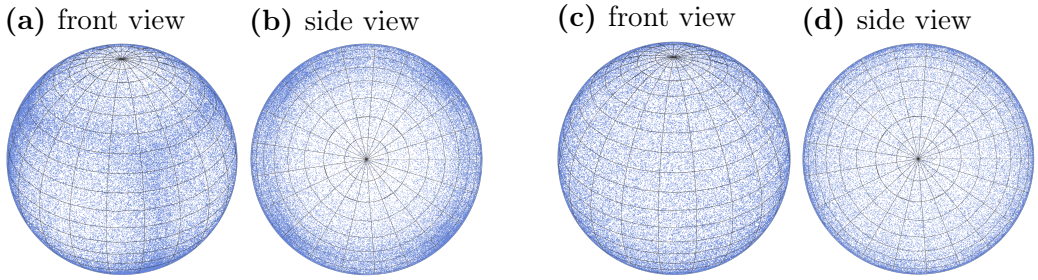

Figure 2.5: Random distributed points on a sphere. (a) and (b) show a non–uniform distribution of points on a sphere, seen by higher point–density on corners and edges of a cube. Hereby points have been selected uniformly on $x, y, z \in [-1, 1]$ and projected onto a sphere by normalising them with $x^2 + y^2 + z^2 = 1$. (c) and (c) show points chosen uniformly distributed on the sphere by the method of Marsaglia Eq. (2.63).

with $\phi \in [0, 2\pi)$ and $u \in [-1, 1]$. These new points are uniformly distributed on the sphere, since the differential element of the solid angle is not a function of the azimuthal angle θ anymore.

$$d\Omega = \sin\theta \; d\phi \; d\theta = -d\phi \; d(\cos\theta) \; . \tag{2.62}$$

In 1972 *George Marsaglia* [171] presented another method, where variables x_1 and x_2 are chosen randomly between $(-1, 1)$ and will be rejected, if $x_1^2 + x_2^2 \geq 1$. The remaining points

$$\begin{aligned} x &= 2x_1\sqrt{1 - x_1^2 - x_2^2} \; , \\ y &= 2x_2\sqrt{1 - x_1^2 - x_2^2} \; , \\ z &= 1 - 2\big(x_1^2 + x_2^2\big) \end{aligned} \tag{2.63}$$

will have a uniform distribution on a sphere, as shown in Fig. 2.5(c) and Fig. 2.5(d). Of course there are many more ways of distributing points randomly on a sphere [172, 173, 171].

Uniformly distributed points on a spherical cone

System dependent unconventional ordering mechanisms often become difficult to correctly sample at very low temperatures. A leading example would be the antiferromagnetic Heisenberg model on the kagome lattice, which lowers its free energy by entropic selection by condensing into a coplanar state. When spins freeze into such a state, fluctuations out of their local quasi–ordered direction will decrease by lowering the temperature and lead to low acceptance rates by choosing a new spin configuration on a sphere.

A possible way to overcome this issue and allow for sufficient acceptance rates and statistics is to sample spin configurations on a spherical cone. As a small but important remark: By choosing a sampling method on a spherical cone, one needs to be conscious

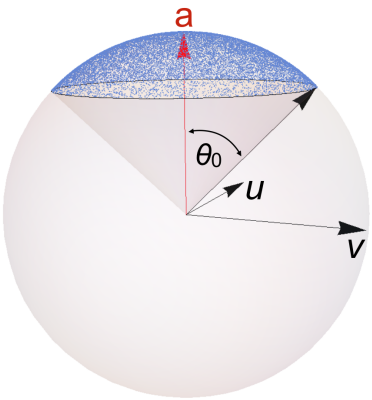

Figure 2.6: Uniformly distributed points on a spherical cone. By knowing the central axes **a** and opening angle θ_0 of the spherical cone, points can be distributed uniformly on its surface.

that generally the fundamental rule of ergodicity is violated. Therefore, this sampling method is just applicable if the behaviour of the physical system is understood well enough and allows a treatment with this algorithm.

To construct points on a spherical cone one uses two mutually–orthogonal unit vectors **u** and **v**, both of them orthogonal to the given central axis **a** of the cone, where $|\mathbf{a}| = 1$ (as shown in Fig. 2.6). We choose the polar angle ϕ uniformly in $[0, 2\pi)$, and the azimuthal angle θ on the interval $(0, \theta_0]$. Hereby, θ_0 stands for the opening angle of the spherical cone and is restricted to the interval $[0, \pi]$. θ_0 is usually decreasing with temperature and goes for the antiferromagnetic Heisenberg model on the kagome lattice as $\theta_0 \sim \sqrt{T}$ [116], in order to account for soft modes.

To find new vectors **x**, uniformly distributed on the spherical cone with $0 \leq \theta \leq \theta_0$, one might follow this recipe: Choose random numbers for z, uniformly distributed on the interval $[\cos\theta_0, 1]$, and set $\theta := \arccos(z)$. Furthermore let ϕ be uniformly distributed on $[0, 2\pi)$. Then the point

$$\mathbf{x} = \sin\theta(\cos\phi\ \mathbf{u} + \sin\phi\ \mathbf{v}) + \cos\theta\ \mathbf{a} \tag{2.64}$$

will be uniformly distributed on the corresponding spherical cone.

Over–relaxation

Another way to increase the sampling statistics of a Monte Carlo simulation, applicable for any system under consideration is provided by the powerful over–relaxation method [174, 175]. Hereby, randomly chosen spins on the lattice are rotated by an arbitrary angle $\phi \in [0, 2\pi)$ around its local exchange field

$$\mathbf{H}_i = \sum_{\delta} J_{i\delta}\ \mathbf{S}_\delta - \mathbf{h}\ , \tag{2.65}$$

where the index δ counts the sites, which are coupled via $J_{i\delta}$ to the i^{th} spin under consideration. By doing so the system energy stays constant, while allowing for a new spin configuration.

Considering the large amount of operations on large lattices, the computational cost for such a vector rotation around individual exchange–field axes are usual quite high. In order to reduce this computational cost, one would simply rotate the spin i

by a polar angle $\phi = \pi$ with the formula:

$$\mathbf{S}_i^{\pi} = 2\ (\mathbf{S}_i \cdot \mathbf{H}_i)\ \frac{\mathbf{H}_i}{|\mathbf{H}_i|} - \mathbf{S}_i\ . \tag{2.66}$$

Heat Bath

As we learned in this Section the single–spin flip Metropolis algorithm might not be sufficient for achieving proper statistical results in a numerical simulation at low temperatures. The limiting factor is the acceptance ratio, which depends on the behaviour of the system under consideration and often becomes very small at small temperatures since the system prefers to make small fluctuations about local minima of the energy. One can improve the rejection ratio by reducing the acceptance window, as e.g. shown by using the cone–approximation [see Fig. 2.6 and Eq. (2.64)], but this practically limits the extent of the phase space that can be explored.

The heat bath algorithm [176, 177] is a rejection–free algorithm, which automatically adjusts the size of a typical move as the temperature is lowered. Hereby, each spin is assumed to be in contact with a heat bath, which puts each spin into a local equilibrium in respect to the instantaneous effective field, coming from its neighbouring spins as defined in Eq. (2.65). The local Hamiltonian associated with spin $\mathbf{S}_i$ on site i is written as

$$\mathcal{H}_{loc}^{i} = \mathbf{H}_i \mathbf{S}_i = H_i S_i \cos\theta\ , \tag{2.67}$$

where θ represents the angle between the local exchange field ($H_i = |\mathbf{H}_i|$) and the local spin ($S_i = |\mathbf{S}_i|$). The probability to find the spin i in a space element of the solid angle $d\omega = \sin\theta\ d\theta\ d\phi$ is written as

$$P(\theta,\phi)\sin\theta\ d\theta\ d\phi = C\exp(-\mathcal{H}_{loc}/k_B T)\sin\theta\ d\theta\ d\phi\ , \tag{2.68}$$

where C denotes a normalisation constant of the form:

$$1/C = \int_0^{2\pi} d\phi \int_0^{\pi} \sin\theta\ d\theta\ \exp(-\mathcal{H}_{loc}/k_B T)\ , \tag{2.69}$$

since the probability of finding a new vector somewhere on the whole sphere needs to be 1. A distribution of continuous energy levels can be sampled by using a random number $R \in [0,1]$ and connect it with the Boltzmann distribution p_μ [Eq. (2.27)]

$$R = \int_1^m d\mu\ p_\mu\ . \tag{2.70}$$

Hereby R, as a random number between 0 and 1 represents the probability to find the system in state m. By the help of this correlation the azimuthal angle θ and polar angle ϕ can be sampled by:

$$R_0 = \int_0^{2\pi} d\phi' \int_0^{\theta} \sin\theta'\ d\theta'\ P(\theta',\phi')\ , \tag{2.71}$$

$$R_1 = \phi/(2\pi) \tag{2.72}$$

with R_0 and R_1 two random numbers. Note that the upper limit in Eq. (2.71) needs to be the azimuthal angle θ, which defines the maximum possible deviation from the local exchange field vector $\mathbf{H}_i$. The polar angle ϕ [Eq. (2.72)] can be arbitrarily chosen between 0 and 2π, since it will not affect the system energy.

By solving Eq. (2.71), one obtains a sampled azimuthal angle θ:

$$\cos\theta = -\frac{1}{HK}\log\left[e^{-2HK}(1-R_0)+R_0\right]-1\,, \tag{2.73}$$

where $K = S/k_BT$. It is necessary to convert the spin direction back to cartesian coordinates, such that the fields on neighbouring sites of n can be easily computed.

The physical meaning behind the heat bath algorithm is rather interesting and has been discussed in the literature [177]. This algorithm seems to mimic additional degrees of freedom, as e.g. lattice vibrations, which allow the system to fall into thermal equilibrium, while, in contrast, the Metropolis update provides simply a mathematical device to give the correct probability distribution in equilibrium.

2.2.5 Parallel tempering

The parallel tempering or exchange Monte Carlo method is a method, developed for improving the dynamical properties of conventional Monte Carlo simulations. It has been introduced the first time in 1986 by Swendsen and Wang [178] in order to solve controversies about properties of systems with quenched random interactions, such as spin glasses and random–field models. Such "hardly–relaxing" systems generally have numerous local energy minima which are separated to each other via energy barriers. In conventional, local–update Monte Carlo algorithms the characteristic time in which a system is able to escape such an energy minimum increases rapidly as temperature decreases [179].

The parallel tempering method is a parallelised Monte Carlo algorithm, which allows for temperature exchange between independent replicas — identical systems with independent starting conditions — and consequently provides rapid relaxation times. Hereby replica, which might get "stuck" in an local energy minimum, seeming to be frozen, are allowed to couple to a different heat bath at higher temperatures. Hereby induced thermal fluctuations allow the system to overcome such a local energy minimum, able to reach a larger phase space, and at some point escape the local energy minimum and relax into a possible global energy minimum.

The very strong point of this algorithm is its compatibility to any other algorithm and easy application to any type of system, even without knowing its low temperature behaviour. The computational effort is relatively modest, while distributed from a single core to many cores, in order to allow for the exchange of replicas at different temperatures, including both high and low temperature phases.

After waiting for the system to thermalise via the simple single–spin flip Monte Carlo method, replicas might be distributed around their equilibration energies in regard to the central limit theorem, as shown in the energy histogram in Fig. 2.7(a). In this configuration the Parallel tempering method allows to swap replicas of neighbouring temperatures (visible by a grey shaded overlap in the energy histogram), if

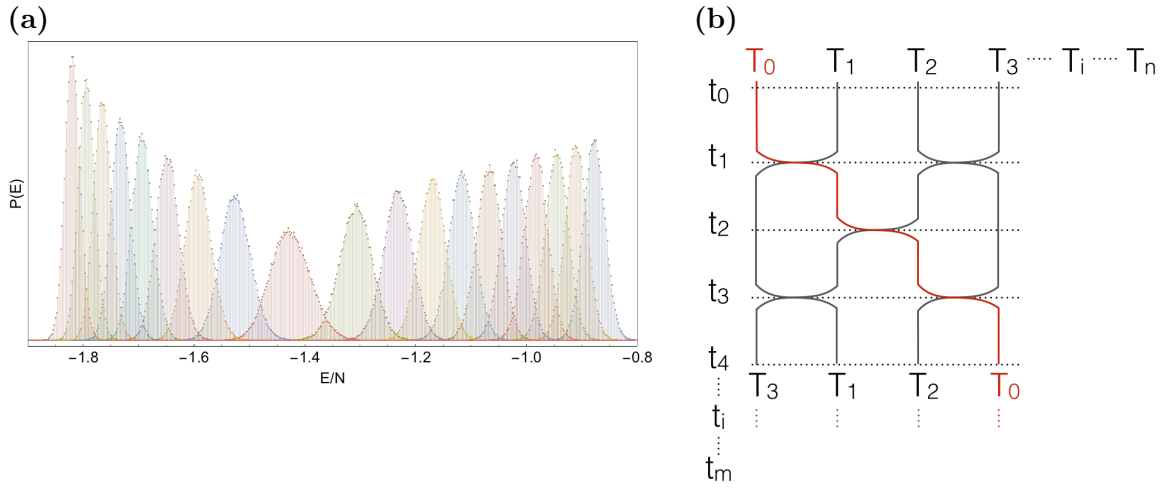

Figure 2.7: Parallel tempering on multi–core Monte Carlo simulations. (a) A schematic energy histogram shows the distribution of individual replicas, after thermal equilibration at different temperatures, following the central limit theorem. Replicas within the overlap region of neighbouring temperatures may be allowed to swap their spin–configuration and thermalise at their new temperature, in order to overcome local energy barriers. (b) The exchange of replicas with different energies are allowed by the transition probability from Eq. (2.74). Hereby n replicas, associated with their individual temperature are evaluated at n different CPU cores. After a certain amount of Monte Carlo (MC) steps (usually $t_i - t_{i-1} \approx 10 - 100$MC steps) replicas at neighbouring temperatures are allowed to swap and thermalise at their new system–temperature in order to be able to escape local energy minima in the system by thermal excitations. After t_m total sweeps, one replica should have been able to visit all available temperatures in the simulation.

their energy and temperatures satisfy the all-important Boltzmann distribution. Energies of replicas with adjacent temperatures shall be evaluated at T_{low} for the replica with lower, and T_{high} for the replica with higher temperature. By considering their corresponding energies, E_{low} and E_{high}, the replicas are allowed to be swapped by the transition probability

$$P(\text{high} \leftrightarrow \text{low}) = \begin{cases} e^{-(\beta_{\text{low}}-\beta_{\text{high}})(E_{\text{high}}-E_{\text{low}})} & \text{if } E_{\text{high}} - E_{\text{low}} > 0 \\ 1 & \text{otherwise.} \end{cases} \tag{2.74}$$

In order to be convinced that this algorithm is correct, one needs to prove ergodicity and the sufficient detailed balance condition. This is discussed in Appendix B.1.

A schematic picture visualises the whole parallel tempering process in Fig. 2.7(b), where n replicas, associated with their individual temperature T_i are evaluated at n different CPU cores. The choice of the temperature grid hereby plays an essential role for guaranteeing exchange between replicas, since the range of energies for a given temperature decreases with increasing system size as $1/\sqrt{N}$, where N is the number of sites in the system. After t_m total Monte Carlo steps, one replica should have been able to visit all available temperatures in the simulation. In such a manner a system at low temperature is allowed to visit high–temperature regions to recover ergodicity, overcome local energy minima and hopefully relax into a global energy minimum.

As a technical fact, such parallel tempering sweeps should not be performed too often, since the system needs time to thermalise at the new temperature again. Temperature sweeps immediately after each other, will not change the system configuration at all and simply correspond to a waste of computer time. In this work sweeps have been performed usually after $10 - 100$MC steps. Also, in order to optimise efficiency, one should just exchange the temperature information and not the whole spin configurations between each CPU, since this process will cost substantial computer time for very large system sizes.

The interested reader, grasping for detailed information about parallel tempering and its application in statistical mechanics shall be referred to the excellent and comprehensive book of *M. E. J. Newman and G. T. Barkema "Monte Carlo Methods in Statistical Physics"* [149] and further literature for an introduction of parallel tempering [178], its first application to spin glasses [179], its application for molecular dynamics simulations [180] and also for the successful determination for crystal structures from powder diffraction data [181]. A review on parallel tempering with its theory, applications, and new perspectives can be found in [182].

2.3 Molecular dynamics

2.3.1 Semi–classical equations of motion

The spin operator is a well–defined quantum mechanical object, which preserves commutation relations and assigns each particle a spin quantum number. However, classical Monte Carlo simulations treat those quantum objects as classical vectors; basically disentangled product states in the limit of an infinite large spin quantum number. This allows to use the quantum nature of the spins by following their commutation relations

in order to calculate their evolution in time. It turns out that this approximation gives quantitatively good results for systems containing larger spin–quantum numbers $S \geq 3/2$ and can already provide useful insights into the behaviour of quantum systems with $S = 1/2$.

The time evolution of the spin operator $\mathbf{S}_n(t)$ at site n is accessible by using the Ehrenfest theorem

$$\frac{d}{dt} S_n^\alpha(t) = \frac{1}{\mathrm{i}\hbar} \left[S_n^\alpha(t), \mathcal{H} \right] \tag{2.75}$$

$$= \frac{1}{\mathrm{i}\hbar} \sum_{\langle ij \rangle, \beta} J_{ij} \left[S_n^\alpha(t), S_i^\beta S_j^\beta \right] \tag{2.76}$$

with $\mathcal{H}$ as defined in Eq. (2.60) in the absence of an external magnetic field. Following the commutation relation for spin operators:

$$\left[S_i^\alpha, S_j^\beta \right] = \mathrm{i}\hbar \, \epsilon_{\alpha,\beta,\gamma} \, S_i^\gamma \delta_{ij} \ , \tag{2.77}$$

where i and j are the site index and α, β, γ the direction component x, y, z. $\epsilon_{\alpha,\beta,\gamma} = 1$ if α, β, γ is cyclic, and -1 if not cyclic. Each component of the spin S_n^α separately gives:

$$\frac{d}{dt} S_n^x(t) = \sum_\delta J_{n\delta} \left(S_\delta^y S_n^z - S_\delta^z S_n^y \right) \ , \tag{2.78}$$

$$\frac{d}{dt} S_n^y(t) = \sum_\delta J_{n\delta} \left(S_\delta^x S_n^z - S_\delta^z S_n^x \right) \ , \tag{2.79}$$

$$\frac{d}{dt} S_n^z(t) = \sum_\delta J_{n\delta} \left(S_\delta^y S_n^x - S_\delta^x S_n^y \right) \ , \tag{2.80}$$

which can be written in a generalised way by a cross product and the local exchange field as defined in Eq. (2.65)

$$\frac{d}{dt} \mathbf{S}_n(t) = \mathbf{H}_n \times \mathbf{S}_n(t) \ . \tag{2.81}$$

Considering the fact that Eq. (2.81) represents coupled linear differential equations, finding an analytical solution will be quite hopeless. However, as a special case, the equations of motion will be decoupled for a system, which is nearly fully polarised. In that case the $\frac{d}{dt}\mathbf{S}^z(t) \approx 0$ and allows for an analytic solution, which can be used compare numerical results. This analytical method is known as spin–wave theory and is presented for the quantum case of the antiferromagnetic square lattice in Appendix B.2.

The general solution to Eq. (2.81) just becomes accessible via numerical integration [183], which has been done in the framework of this thesis with the Runge-Kutta method of order 4.

2.3.2 Numerical integration – 4^{th} order Runge–Kutta

As the name refers to, Molecular Dynamics is used to study the dynamical properties of molecules in real time [184, 185]. This method is not just limited to molecules, but

also can be used to calculate the dynamical properties of spins on a lattice. As seen above one needs to solve coupled differential equations, which is generally not possible analytically, but can be approximated by iterative interpolation. Ordinary differential equations usually have the following form:

$$y' = f(x, y) \tag{2.82}$$

with a solution

$$y = y(X) = y_0 + \int_{x_0}^{X} f(x)dx \ . \tag{2.83}$$

By expanding Eq. (2.82) by means of a Taylor series in order to extrapolate its result, one arrives at:

$$\begin{aligned} y(x_0 + h) = y(x_0) + hf(x_0, y_0) + \frac{h^2}{2}(f_x + f_y f)(x_0, y_0) \\ + \frac{h^3}{6}(f_{xx} + 2f_{xy}f + f_x f_y + f_{yy}f^2 + f_y^2 f)(x_0, y_0) + O(4) \ , \end{aligned} \tag{2.84}$$

where h indicates the increment in x until the next point of interpolation. $f_x = \frac{\partial}{\partial x} f$ corresponds to the partial derivative of f to x.

First attempts to solve Eq. (2.82) were provided by *Euler* in 1768 in his "Institutiones Calculi Integralis" (Sectio Secunda, Caput VII) [186], giving the solution:

$$y_1 = y_0 + hf(x_0, y_0) \ . \tag{2.85}$$

Comparing this result with the solution from the Taylor series of the exact solution in Eq. (2.84), one obtains a difference Δy for the first step:

$$\Delta y = y(x_0 + h) - y_1 = \frac{h^2}{2}(f_x + f_y f)(x_0, y_0) + \dots \tag{2.86}$$

with the error correction $O(h^2)$. This formula is neither very accurate, since it uses the derivative information only at the beginning of the interval of length "h", nor very stable.

The accuracy in that sense can be increased by reducing these weak points by choosing intermediate points with the midpoint method, which allows to extrapolate the following integration step by

$$k_1 = f(x_0, y_0) \tag{2.87}$$

$$k_2 = f(x_0 + \frac{h}{2}, y_0 + \frac{h}{2}k_1) \tag{2.88}$$

$$y_1 = y_0 + hk_2 \ . \tag{2.89}$$

In order to compare the error of this method with the exact solution of Eq. (2.84) one needs to compute the Taylor expansion of y_1 in Eq. (2.89):

$$y_1 = y_0 + hf(x_0 + \frac{h}{2}, y_0 + \frac{h}{2}k_1) \tag{2.90}$$

$$= y_0 + hf(x_0, y_0) + \frac{h^2}{2}(f_x + f_y f)(x_0, y_0) \tag{2.91}$$

$$\frac{h^3}{8}(f_x x + 2f_{xy}f + f_{yy}f^2)(x_0, y_0) + \dots \ , \tag{2.92}$$

providing an error of

$$\Delta y = y(x_0 + h) - y_1 \tag{2.93}$$

$$= \frac{h^3}{24}(f_{xx} + 2f_{xy} + f_{yy}f^2 + 4(f_y f_x + f_y^2 f))(x_0, y_0) + \dots \ , \tag{2.94}$$

which provides a result one order better in accuracy than the Euler method with $O(h^3)$. Conventionally, methods are called n^{th} order if its error term is in $O(h^{n+1})$, why the midpoint method also can be referred to second–order Runge–Kutta method.

By introducing further Euler steps into the calculation, *Runge* (1895) [187] and *Heun* (1900) [188] increased the accuracy from Eq. (2.89). It was *Kutta* (1901) [189] who then formulated a general scheme for what is called the Runge–Kutta method, which looks for its 4^{th} order as:

$$k_1 = f(x_0, y_0) \tag{2.95}$$

$$k_2 = f(x_0 + \frac{h}{2}, y_0 + \frac{h}{2}k_1) \tag{2.96}$$

$$k_3 = f(x_0 + \frac{h}{2}, y_0 + \frac{h}{2}k_2) \tag{2.97}$$

$$k_4 = f(x_0 + h, y_0 + k_3) \tag{2.98}$$

$$y_1 = y_0 + \frac{1}{6}k_1 + \frac{1}{3}k_2 + \frac{1}{3}k_3 + \frac{1}{6}k_4 \ . \tag{2.99}$$

Higher order Runge–Kutta methods are in general superior to lower order Runge–Kutta methods, however its accuracy depends on the mathematical problem. To confirm satisfactory precision of the simulation, one should check the energy conservation and its error, produced during the numerical integration.

2.3.3 Application to spin systems

Dynamical properties can just be studied in systems with a continuous degree of freedom as e.g. provided by the Heisenberg model, which is seemingly the first model studied within the framework of Molecular Dynamics simulations [190, 191].

After equilibrating the system via Monte Carlo simulations, the Runge–Kutta method can be used to evaluate the time evolution of all spins on the lattice. Hereby, the time–increment $\delta t = h$ needs to be chosen sufficiently small, such that the energy of the system will be conserved with sufficiently large accuracy.

Since spin–spin correlations are directly accessible with inelastic neutron scattering (INS) experiments, one is interested in calculating the dynamical structure factor $S(\mathbf{q}, \omega)$, a comparable quantity for dynamical properties in energy and momentum space.

2.4 Correlation functions in momentum space

A general property of spin liquids is the absence of conventional order at low temperatures. This means, magnetic moments are still fluctuating and show correlations,

specific to the underlying physical nature within the spin liquid. These dynamical signatures are measured in inelastic neutron scattering (INS) experiments and can directly be compared to calculations of the dynamical structure factor $S(\mathbf{q},\omega)$.

2.4.1 Dynamical structure factor

The analysis of spin correlations in magnetic materials plays a crucial role in estimating their thermodynamic and dynamic properties. Neutrons have a spin, but no electric charge, which makes them to ideal probes for magnetic properties in crystals. Experimentally this is done in inelastic neutron scattering (INS) experiments, which measures the flux of scattered neutrons σ in a solid angle $d\Omega$ with energy dE_f This quantity is the so–called double differential cross section for magnetic scattering [192, 193] and is given by

$$\frac{d^2\sigma}{d\Omega dE_f} \propto \mathcal{F}(\mathbf{q})^2 \sum_{\alpha,\beta} \left(\delta_{\alpha\beta} - \frac{q_\alpha q_\beta}{\mathbf{q}^2}\right) S^{\alpha\beta}(\mathbf{q},\omega) \;, \tag{2.100}$$

where the signal needs to be multiplied by $\mathcal{F}(\mathbf{q})$, the magnetic form factor, since magnetic scatterers have a finite width in real space and cannot be approximated as discrete point scatterers. Neutrons only measure the magnetic field distribution perpendicular to the scattering vector, what has been taken into account by the term $(\delta_{\alpha\beta} - \frac{q_\alpha q_\beta}{\mathbf{q}^2})$. $S^{\alpha\beta}(\mathbf{q},\omega)$ is the direction–dependent dynamical structure factor, also known as the Fourier transform of the real–space spin–spin structure factor into energy and momentum space

$$S^{\alpha\beta}(\mathbf{q},\omega) = \frac{1}{\sqrt{2\pi}N} \sum_{i,j}^{N} \mathrm{e}^{\mathrm{i}\mathbf{q}(\mathbf{r}_i - \mathbf{r}_j)} \int_{-\infty}^{\infty} dt\, \mathrm{e}^{\mathrm{i}\omega t} \left\langle S_i^\alpha(0) \cdot S_j^\beta(t) \right\rangle \;, \tag{2.101}$$

with $S_i^\alpha(t)$ the time–dependent α–component of the spin at site i and $\langle \ldots \rangle$ the thermodynamic average.

In order to technically extract the Fourier transform of the spin–spin correlation function one needs to be cautious about the signal sampling in time.

2.4.2 Signal sampling in time

The time evolution of the spin component in real space, provided by the numerical integration of the semiclassical equations of motion, need to be Fourier transformed twice, once from time to energy, and secondly from real space to momentum space. Technically, such a Fourier transform can be implemented manually, however the use of libraries as provided by e.g. FFTW3 (*http://www.fftw.org*) is strongly recommended, in order to save computation time.

It is important to choose the correct values of the time increment Δt, which will be the time difference between two position vectors $\mathbf{S}_i(t)$ and $\mathbf{S}_i(t+\Delta t)$ (not to confuse with the time increment used by the Runge–Kutta method δt in the last section). The numerical integration needs to provide a sampling–rate that allows to capture all possible information provided in by the system. Hereby, the Nyquist–Shannon sampling theorem gives a sufficient condition allowing to reduce a continuous signal

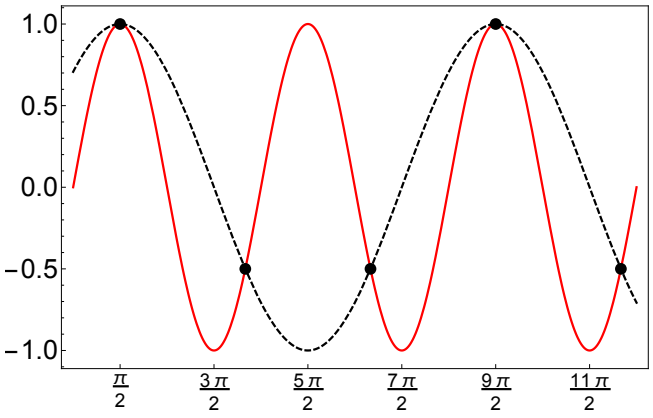

Figure 2.8: Sampling, following the Nyquist criterion. Following the Nyquist criterion, discretisation or sampling of a continuous function in time has to happen at least at twice of its maximum frequency. If this criterion is not satisfied, function reconstruction will exhibit aliasing, an effect that causes different signals to become indistinguishable when sampled, as shown for two sine functions $\sin(x)$ (red) and $\sin\left(\frac{\pi}{4}+\frac{1}{2}x\right)$ (dashed black).

into discrete steps (analog to digital signal processing) without loosing information. If the sampling is worse than in this limit, then the system will show aliasing, accompanied by unphysical patterns, as seen for the case of a simple sine function in Fig. 2.8.

Might the numerical simulation provide no frequencies higher than ω_{max}, then the whole spectrum can be captured by a series of points spaced at $1/(2\omega_{max})$ apart (perfect reconstruction will be guaranteed). To be "on the safe side" one uses usually twice as many data points as provided by the Nyguist condition.

By providing the maximum frequency ω_{max} in the system and the total number of considered time steps N_t, all necessary information for a proper Fourier transform with time increment Δt are given by the conditions

$$\Delta t = \frac{2\pi}{\omega_{max}} = N_{RK}\delta t \tag{2.102}$$

$$\Delta\omega = \frac{2\pi}{T_{max}} = \frac{2\pi}{N_t\Delta t} = \frac{2\pi}{N_t N_{RK}\delta t}\,, \tag{2.103}$$

where δt has been introduced in the previous section as the time difference between two successive Runge–Kutta steps for N_{RK} total Runge–Kutta data points. δt is fixed by the necessary accuracy of the simulation and stability of the numerical integration. Since the energy of the system should be conserved, the variation in energy over the whole numerical integration should be sufficiently low and needs to be taken as a reference to choose δt small enough.

The increment in frequency $\Delta\omega$ is indirectly proportional to the total amount of sampling time of the system T_{max}, and therefore depends on the considered time steps N_t of the simulation.

2.4.3 Numerical artefacts

With all the explanations above, one is able to calculate the dynamical properties of spin systems in momentum and energy space. However, there still is a technical issue, which needs to be solved before being able to provide proper results, comparable to

experimental measurements. The numerical integration of the time–dependent spins in the system starts at time t_0 and ends at t_{max}, and therefore provides a box function with singular points at these times. The Fourier transform of a box function is a cardinal sine function

$$\frac{1}{\sqrt{2\pi}}\int_{-\infty}^{\infty}\mathrm{rect}(t)e^{-i\omega t}dt = \frac{1}{\sqrt{2\pi}}\frac{\sin(\omega/2)}{\omega/2} = \frac{1}{\sqrt{2\pi}}\mathrm{sinc}(\omega/2)\ . \tag{2.104}$$

In order to reliably sample singular features in the spectrum, one needs an infinite number of Fourier components in the Fourier transform, which is simply not possible to calculate. The Fourier transform with a finite number of Fourier components will produce unphysical features away from the main frequency, which makes proper studies of physical objects cumbersome and difficult.

Here one can refer to a trick, by using the convolution theorem. The convolution theorem says, that the Fourier transform of two multiplied functions equals the convolution of both individual Fourier transformed functions [194]. Let $\mathfrak{F}$ be the Fourier transform acting on the independent functions f and g then the convolution theorem states that:

$$\mathfrak{F}\{f\cdot g\} = \mathfrak{F}\{f\} * \mathfrak{F}\{g\}\ , \tag{2.105}$$

where $*$ denotes the the convolution and $\cdot$ the multiplication of two functions.

This theorem is rather useful, since a simple multiplication of the time–dependent spin signal in real space by a Gaussian envelope, will produce a Gaussian convoluted signal in energy after performing a Fourier transform. In that sense the removal of information in time allows to realistically mimic INS experiments with finite–energy resolution and suppress technical artefacts from the Fourier transformation over a finite time window.

Chapter 3

Curie–law crossover: thermodynamic signatures of spin liquids

" *Was glänzt, ist für den Augenblick geboren;*
Das Echte bleibt der Nachwelt unverloren."

Faust 1, Vers 73 f. (Dichter)
Johann W. v. Goethe

For more than 100 years the Curie–Weiss law [10, 11], has been known as a mean–field estimate of magnetic properties in conventional magnets above their critical point. More recent, the Curie–Weiss law is also widely used in the field of frustrated magnetism and provides an empirical estimate for their "strength of frustration" [195]. However, mean–field approximations usually neglect fluctuations and correlations between spins, suggesting that this method does not represent an appropriate approximation for spin liquids, which are characterised by a collective cooperative behaviour already at high and intermediate temperatures.

The absence of a symmetry–breaking phase transitions, a gradual increase of correlations from a high–temperature paramagnetic into a low–temperature cooperative–paramagnetic regime and controversial fitting results in the literature motivate a detailed follow–up on the limitations of the Curie–Weiss law in spin liquids.

This Chapter presents the concept of the "Curie–law crossover" on a variety of frustrated lattices in both, two and three dimensions, by using complementary analytical and numerical techniques, namely Husimi tree calculations and Monte Carlo simulations. Spin liquids are characterised by a crossover between different high–temperature and low–temperature Curie–laws, which turns out to be a powerful signature of exotic physics in classical spin liquids, able to explain the difficulty for a precise estimate of the Curie–Weiss temperature in experiments.

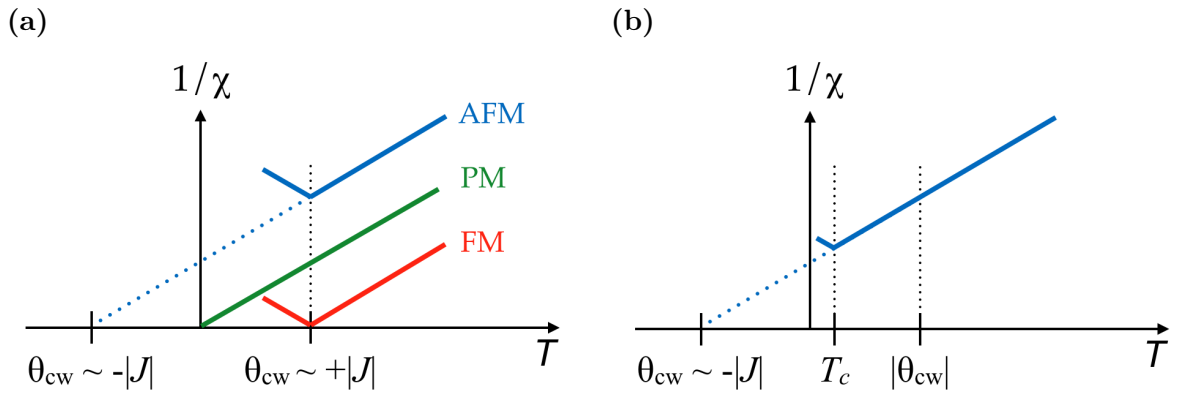

Figure 3.1: Curie–Weiss law in conventional and frustrated magnets. The inverse susceptibility $1/\chi$ allows to obtain the value of the Curie–Weiss temperature θ_{cw} in a magnetic system, as defined in Eq. (3.5). (a) Conventional magnets show values of $|\theta_{cw}| \sim |J|$, of the order of the coupling constants J. The sign θ_{cw} hereby predicts the type of dominating correlations in the system, which can be antiferromagnetic (blue), ferromagnetic (red), or negligible at the temperature of measurement (green), as in a paramagnet. The dashed line is an extrapolation of the linear term in $1/\chi$ down to negative temperatures. (b) $1/\chi$ in frustrated magnets stand out by the fact, that an ordering–temperature T_c is pushed down to temperatures much lower than $|\theta_{cw}|$. The ratio $f \equiv |\theta_{cw}|/T_c$ is often used as an empiric measure of the "strength of frustration" in the system [195].

3.1 Curie–Weiss law in conventional and unconventional magnets

3.1.1 From Curie–law to Curie–Weiss law

A common way to approximate magnetic properties in complex systems is to use a standard mean–field theory (Section 1.2.1). In the high–temperature limit, the susceptibility of decorrelated spins in a small magnetic field h is given by the Curie–law:

$$\chi_0 = \frac{N}{V}\frac{(g\mu_B)^2}{3}\frac{J(J+1)}{k_B T} \qquad \text{, for } k_B T \gg g\mu_B h \ , \tag{3.1}$$

with N spins of angular quantum number J in a volume V of the solid. The Curie–constant C takes commonly the value

$$C = \frac{N}{V}\frac{(g\mu_B)^2}{3k_B} J(J+1) \ . \tag{3.2}$$

Upon cooling, interactions within the lattice will introduce a deviation from the high–temperature paramagnetic Curie–law, which can be introduced by an effective external field within the solid

$$h_{\text{eff}} = h + \lambda m \ , \tag{3.3}$$

where λ is the Weiss–molecular field constant coupled to the magnetisation m. The susceptibility then is given by

$$\chi = \frac{\partial m}{\partial h} = \frac{\partial m}{\partial h_{\text{eff}}} \frac{\partial h_{\text{eff}}}{\partial h} = \chi_0(1 + \lambda\chi) \ , \tag{3.4}$$

where χ_0 is evaluated for the effective field h_{eff}. Far above the ordering temperature ($T \gg T_{\text{c}}$), in the limit of zero applied field, h_{eff} vanishes and χ_0 is taking the form of the Curie–law in Eq. (3.1). Near the ordering temperature ($T \approx T_{\text{c}}$), the zero–field susceptibility in the paramagnetic regime [10, 11, 28] of Eq. (3.4) gives:

$$\chi = \frac{C}{T - \theta_{cw}} \ , \tag{3.5}$$

with $\theta_{cw} \equiv \lambda C$ the Curie–Weiss temperature.

The extrapolation of a linear Curie–Weiss fit of $1/\chi$ [Fig. 3.1(a)] can be used to extract C and θ_{cw}. Hereby, θ_{cw} allows to predict the type of correlations in the system, which usually are

$$\begin{aligned} &\theta_{cw} < 0 \text{ for antiferromagnetic correlation} \ , \\ &\theta_{cw} = 0 \text{ paramagnetic phase} \ , \\ &\theta_{cw} > 0 \text{ for ferromagnetic correlations} \ . \end{aligned}$$

For conventional magnets θ_{cw} is in the order of the phase–transition temperature and coupling constant $|\theta_{cw}| \sim |T_{\text{c}}| \sim |J|$.

3.1.2 Curie–Weiss law in spin liquids

Quite commonly, the Curie–Weiss law is also used to specify the nature of correlations in frustrated magnets. In that context, the ratio

$$f \equiv \frac{|\theta_{cw}|}{T_{\text{c}}} \tag{3.6}$$

presents an empirical signature of frustration [195], where large values of f account for strong frustration in the material. T_{c} corresponds to a non–trivial ordering or freezing temperature of the system, which, for spin liquids, ideally is pushed down to zero temperature [Fig. 3.1(b)].

However, past studies pointed at the possibility of misjudgement of frustration in spin liquids by the use of an oversimplified Curie-Weiss law [196]. Independent studies on e.g. pyrochlore oxides from Bramwell *et al.* [197] and Lummen *et al.* [198] show different estimates for θ_{cw} by fitting in a different range of temperatures. For example, the Curie–Weiss temperature for $Dy_2Ti_2O_7$ ($Ho_2Ti_2O_7$) has been estimated with $\theta_{cw} \cong 1.0$ K ($\theta_{cw} \cong 2.0$ K) in [197] by fitting $1/\chi$ within a temperature window of 10–20 K (20–50 K), proposing weak ferromagnetic correlations. On the other hand, different Curie–Weiss temperatures for the same materials have been estimated with $\theta_{cw} = 2(2)$ K ($\theta_{cw} = 6(2)$ K) in [198] by fitting at temperatures above 100 K. Also, further references present deviations from the common Curie–Weiss law in the frustrated

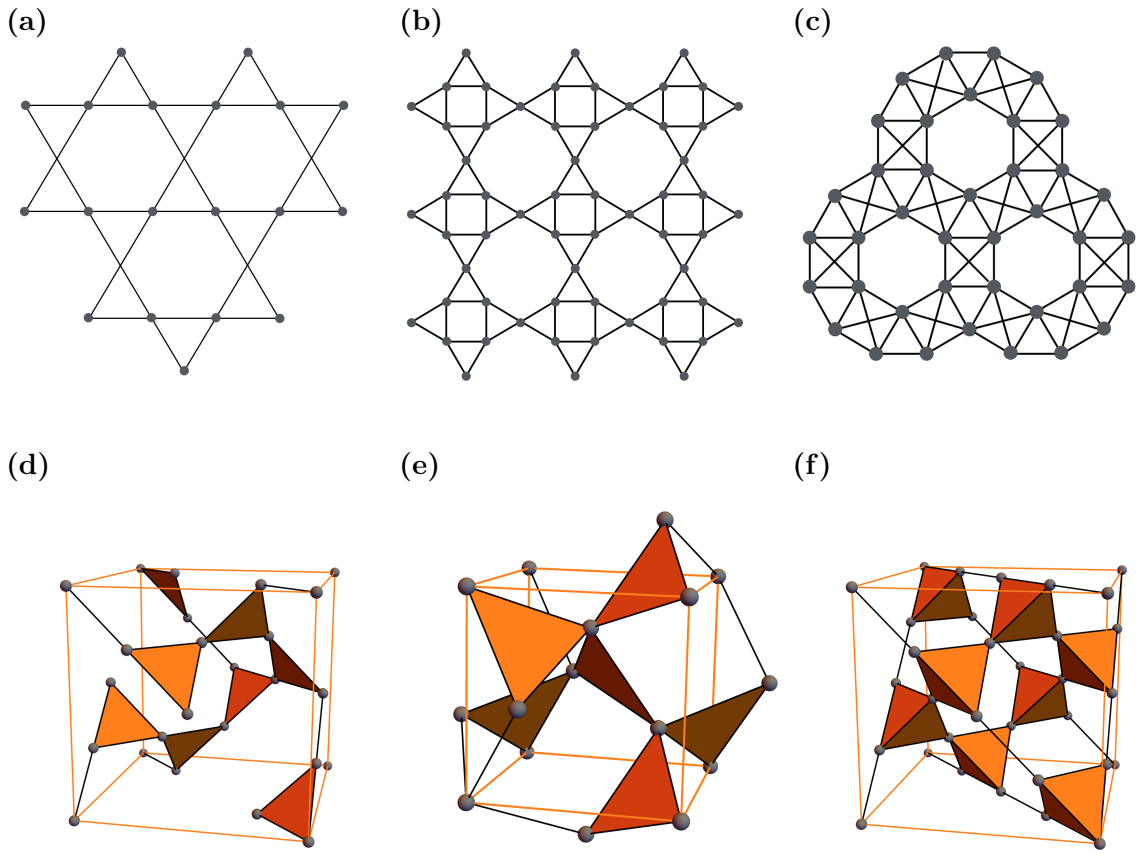

Figure 3.2: Diversity of corner sharing lattices in two and three dimensions. The antiferromagnetic Ising model [Eq. (3.7)] investigated on the two–dimensional (a) kagome, (b) shuriken and (c) ruby lattice; and the three–dimensional (d) hyperkagome, (e) trillium and (f) pyrochlore lattice.

$S = 1/2$ system Li_2VOSiO_4 [199], and the spin–orbital liquid candidate $Ba_3ZnIr_2O_9$ [196].

The absence of symmetry–breaking phase transitions, their cooperative correlations in a broad range of temperatures and controversial fitting results in the literature motivate a detailed follow–up on the limitations of using the Curie–Weiss law in spin liquids.

3.2 Curie-law crossover

Since fluctuations play a major role in frustrated magnets, one might consider an analytical method, which approximates thermodynamic properties better than in a standard mean–field theory. The Husimi tree (see Section 2.1 for technical details) provides a very powerful tool to study classical spin liquids, as shown by the successful prediction of the zero–point entropy [140] and the three–dimensional Kasteleyn transition in spin ice [200, 201], and the prediction of magnetic susceptibilities over a wide

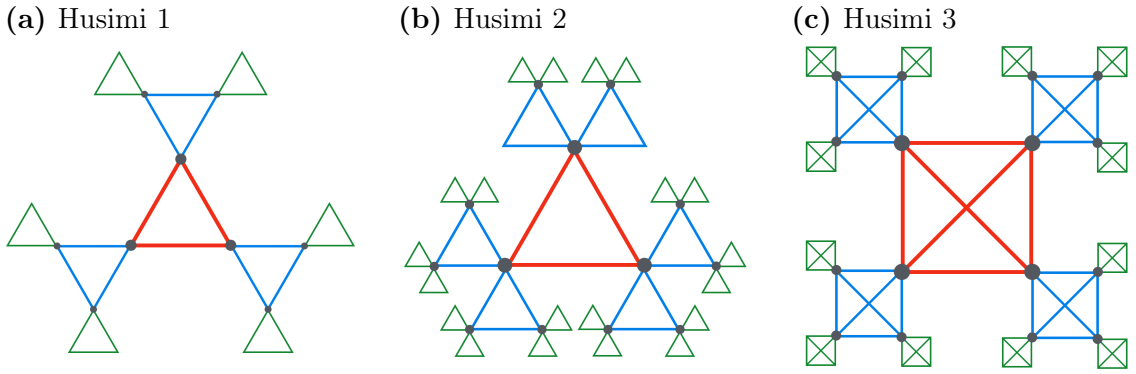

Figure 3.3: Husimi Tree on various corner sharing lattices. Frustrated unit cells from real lattices [Fig. 3.2] are arranged on the Husimi tree (HT), with the central unit in red, the 1^{st} shell in blue and the 2^{nd} shell in green. (a) HT for the kagome, hyperkagome and shuriken lattice, with corner sharing triangular plaquettes. (b) HT for the trillium lattice, were three triangular plaquettes share one corner. (c) HT for the pyrochlore and ruby lattice, which is made of corner–sharing square plaquettes, with first and second–neighbour interactions.

range of temperatures in spin ice materials [141, 142].

The following results concentrate on thermodynamic properties for the isotropic antiferromagnetic Ising model

$$\mathcal{H} = -J \sum_{\langle ij \rangle} \sigma_i \sigma_j \,, \tag{3.7}$$

on various corner–sharing lattices in two and three dimensions, as depicted in Fig. 3.2.

Hereby, an important quantity of magnetic correlations is the reduced susceptibility

$$\chi T = \frac{1}{N} \left(\sum_{i,j} \langle \sigma_i \sigma_j \rangle - \langle \sigma_i \rangle \langle \sigma_j \rangle \right), \tag{3.8}$$

$$= 1 + \frac{1}{N} \sum_{i \neq j} \langle \sigma_i \sigma_j \rangle \,, \tag{3.9}$$

which recovers the common Curie–law at high temperatures ($\chi T\big|_{T\to\infty} = 1$, compare to Eq. (3.1) & Eq. (3.2) with C = 1 for Ising spins). As one can see, deviations from the high–temperature value directly depend on the averaged correlations $\sum_{i\neq j}\langle \sigma_i \, \sigma_j \rangle$ within the system, causing $\chi T > 1$ for dominant ferromagnetic and $\chi T < 1$ for dominant antiferromagnetic correlations at low temperatures. Those correlations become important in spin liquids at already high temperatures, and are neglected in conventional mean–field theories.

In classical frustrated spin systems, the spin–liquid phase usually refers to an extensively degenerate ground state manifold at T = 0. However, for all models considered here [Fig. 3.2], the finite entropy plateau persists up to $T/|J| \sim 1$, as seen in Fig. 3.4. This entropy plateau is accompanied by a spin-liquid Curie law, followed at higher

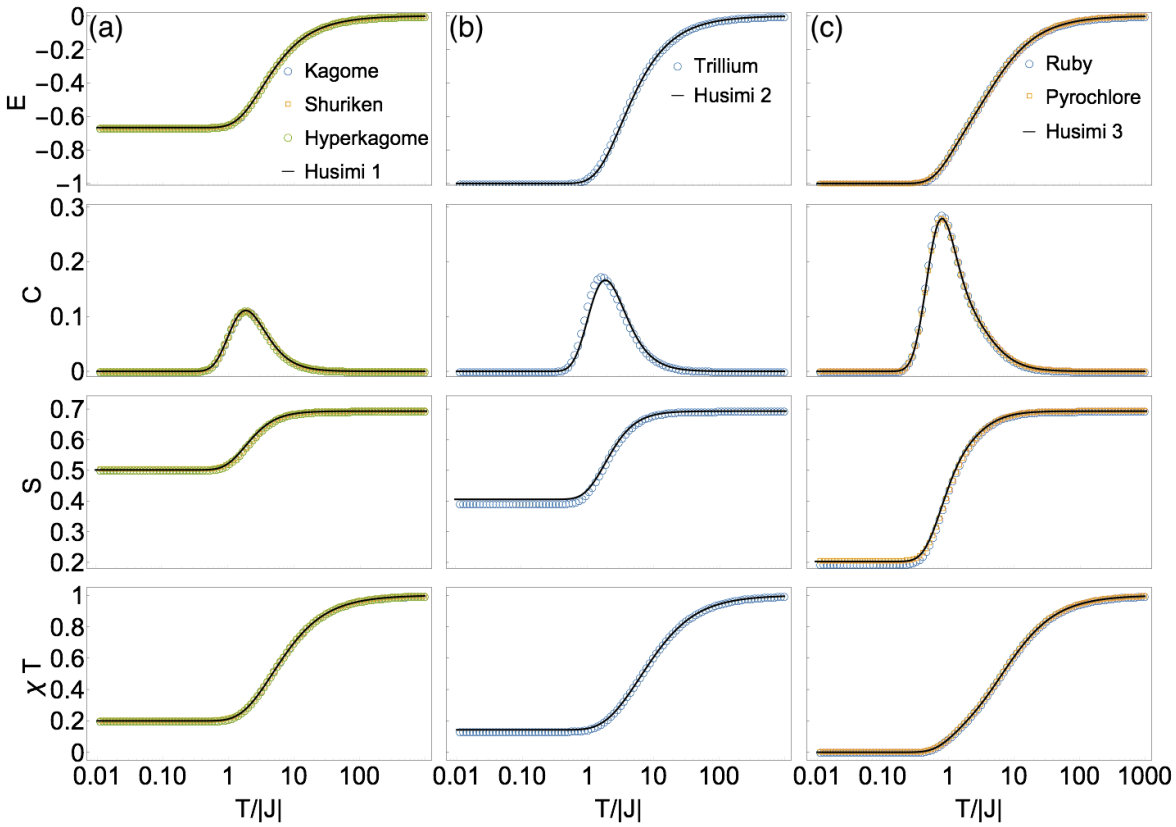

Figure 3.4: Thermodynamic properties of frustrated magnets. Comparison of energy E, specific heat C_h, entropy S and reduced susceptibility χT per spin between results from classical Monte Carlo simulations (discrete data points) on the real lattice [Fig. 3.2] and analytical calculations (solid lines) on their corresponding Husimi tree [Fig. 3.3]. (a) Results for lattices with triangular unit cells: the kagome, shuriken and hyperkagome lattice. (b) Results for lattices with three triangular plaquettes, connected on one corner as in the trillium lattice. (c) Results for lattices with checkerboard–type unit cells: the ruby and pyrochlore lattice. All systems perform a crossover from a high–temperature paramagnetic regime into a low–temperature cooperative paramagnetic (classical spin liquid) regime. This is seen by a very broad peak in the specific heat, a gradual decrease of entropy to a non–zero value at low temperatures and two different Curie–laws at high and low temperatures in the reduced susceptibility χT [Eq. (3.9)]. Monte Carlo simulations have been performed with the standard Metropolis single–spin flip algorithm for $N > 10000$ sites, and additional Worm algorithms [202] for the Ruby and Pyrochlore lattices to account for proper low–temperature equilibration.

Lattice	S ($T \to 0$)		χT ($T \to 0$)	
	Monte Carlo	Husimi Tree	Monte Carlo	Husimi Tree
Kagome	0.502(1)	0.5014	0.201(1)	1/5
Hyperkagome	0.502(1)	0.5014	0.200(1)	1/5
Shuriken	0.504(1)	0.5014	0.203(1)	1/5
Trillium	0.392(1)	0.4055	0.135(1)	1/7
Ruby	0.194(1)	0.2027	0.0	0
Pyrochlore	0.206(1)	0.2027	0.0	0

Table 3.1: Comparison of low–temperature results from Monte Carlo simulations and Husimi tree calculations. The entropy S and reduced susceptibility χT in the limit $T \to 0$ is displayed for all lattices under consideration [Fig. 3.2]. Results, obtained by Monte Carlo simulations and Husimi tree calculations match very well. While the Husimi tree usually underestimates the entropy, it does not do so for the trillium and ruby lattice. Exact results for the kagome lattice ($S = 0.50183$ [94]) and the pyrochlore lattice ($S = 0.20501$ [203]) are within the error of the Monte Carlo simulations. Monte Carlo simulations have been performed with the standard Metropolis single–spin flip algorithm for $N > 10000$ sites, and additional Worm algorithms [202] for the Ruby and Pyrochlore lattices to account for proper low–temperature equilibration.

temperature by a broad crossover (spanning one or two orders of magnitude in temperature) into the paramagnetic regime. Hereby, the specific value of χT is a direct measure of the integrated correlations between spins [Eq. (3.9)], and as such a signature of the nature of the considered spin liquid. For example, in the ground state for the Ruby and Pyrochlore lattices, χT goes to zero, as opposed to all other models [see Tab. 3.1].

Also remarkable at this point is the structure of the shuriken lattice, which allows for a reentrant phenomenon between disordered phases. As shown in Fig. 4.7 of Section 4.3 an advanced Husimi tree for the shuriken lattice (Appendix C.1) shows for a specific range of bond interactions dominating ferromagnetic correlations at high temperatures, while dominating antiferromagnetic correlations at low temperatures. A high–temperature Curie–Weiss fit would hereby provide a dramatically wrong estimate of the low–temperature physics and should be considered with special caution [196].

3.3 Validity of Husimi tree

The Husimi tree considers a frustrated model on a connected graph in which no line lies on more than one cycle. Compared to the real lattice, the Husimi tree does not account for loops larger than those, given by a single frustrated unit, which are e.g. in the case of the kagome lattice loops of size six.

However, even though its topology is very different from the real lattice, all thermodynamical quantities presented in Fig. 3.4 match between Monte Carlo simulations

and Husimi tree calculations surprisingly well over a big range of temperatures. This suggests that the correlations of the considered model drop off at length scales, shorter than the sizes of loops, which cannot be considered in the Husimi tree calculation.

To confirm this hypothesis, one can calculate the correlation length on the Husimi tree. The central spin in "Husimi 1" [Fig. 3.3(a)] is surrounded by four nearest neighbours and provides at zero temperature six out of eight total states in the ground state. The averaged spin–spin correlation to one of the four neighbours on the first shell is

$$\langle \sigma_0 \sigma_1 \rangle_{\mathrm{gs}} = -\frac{1}{3} \,. \tag{3.10}$$

One can define $\langle \sigma_0 \sigma_n \rangle$ as the correlations between the central site σ_0 and all sites σ_n on shell n

$$\begin{aligned} \langle \sigma_0 \sigma_1 \rangle &= 4\left(-\frac{1}{3}\right) \,, \\ \langle \sigma_0 \sigma_2 \rangle &= 8\left(-\frac{1}{3}\right)^2 \,, \\ \langle \sigma_0 \sigma_3 \rangle &= 16\left(-\frac{1}{3}\right)^3 \,, \\ &\vdots \\ \langle \sigma_0 \sigma_n \rangle &= 2 \cdot 2^n \left(-\frac{1}{3}\right)^n \,. \end{aligned} \tag{3.11}$$

As expected, Eq. (3.11) recovers the result for χT [Eq. (3.9)], by summing over all available correlations in the whole Husimi tree:

$$\begin{aligned} \chi T &= 1 + \sum_{n=1}^{\infty} \langle \sigma_0 \sigma_n \rangle \\ &= 1 + \sum_{n=1}^{\infty} 2 \cdot 2^n \left(-\frac{1}{3}\right)^n = 1 + 2\left[\sum_{n=0}^{\infty} \left(-\frac{2}{3}\right)^n - 1\right] \\ &= 0.2 \,. \end{aligned} \tag{3.12}$$

Considering the averaged correlation function $C(n)$ along a single path over n bonds gives

$$C(n) = \left(-\frac{1}{3}\right)^n \tag{3.13}$$

$$= (-1)^n \, e^{-n \ln 3} \,, \tag{3.14}$$

which allows to define a correlation length ξ, with $C(n) \sim e^{-\frac{n}{\xi}}$:

$$\xi = \left(\ln 3\right)^{-1} \approx 0.91 \,. \tag{3.15}$$

This result is the same for the other trees "Husimi 2" and "Husimi 3", and shows that the correlation length is of the order of a single–bond distance. Correlations decay over

short distances, such that the effect of different topology between Husimi tree and real lattice becomes negligible, allowing for such a good match between both methods.

As a remark: Results on the trillium lattice show a less good match than for other lattices [Fig. 3.4(b) and Tab. 3.1], since the smallest non–trivial loops are of size five, effectively one bond shorter than on the other lattices with triangular units.

3.4 Limit of Curie–Weiss fit and relevance to experiments

Fig. 3.4 shows a crossover between two different Curie-laws at high ($> 100|J|$) and low temperature ($< 1|J|$). Since this crossover occurs over a very wide range of temperatures, it is important to clarify the temperature window, which would allow a high–temperature Curie–Weiss fit in order to estimate low–temperature physics in spin liquids.

The inverse susceptibility can be written as a high–temperature expansion [28], resolving the Curie–Weiss law in first order

$$\frac{1}{\chi} = \frac{T}{C}\left(1 - \frac{\theta_{\mathrm{cw}}}{T}\right) . \tag{3.16}$$

The same high–temperature expansion can be done for the results of the Husimi tree calculation, where second and higher order terms will account for the deviation from the Curie–Weiss law. Results on the Husimi tree, shown in Fig. 3.3 are summarised as follows:

Husimi 1:

$$\frac{1}{\chi} = T\frac{5 - e^{-\frac{4}{T}}}{3e^{-\frac{4}{T}} + 1} = T\left(1 - \frac{-4}{T}\left(1 + \frac{1}{T} - \frac{1}{3T^2} + \dots\right)\right) , \tag{3.17}$$

$$C = 1 , \tag{3.18}$$

$$\theta_{\mathrm{cw}} = -4 , \tag{3.19}$$

$$\Delta(T) = \frac{1}{T} - \frac{1}{3T^2} + \mathcal{O}(T^3) , \tag{3.20}$$

Husimi 2:

$$\frac{1}{\chi} = T\frac{7e^{\frac{4}{T}} - 3}{e^{\frac{4}{T}} + 3} = T\left(1 - \frac{-6}{T}\left(1 + \frac{1}{T} - \frac{1}{3T^2} + \dots\right)\right) , \tag{3.21}$$

$$C = 1 , \tag{3.22}$$

$$\theta_{\mathrm{cw}} = -6 , \tag{3.23}$$

$$\Delta(T) = \frac{1}{T} - \frac{1}{3T^2} + \mathcal{O}(T^3) , \tag{3.24}$$

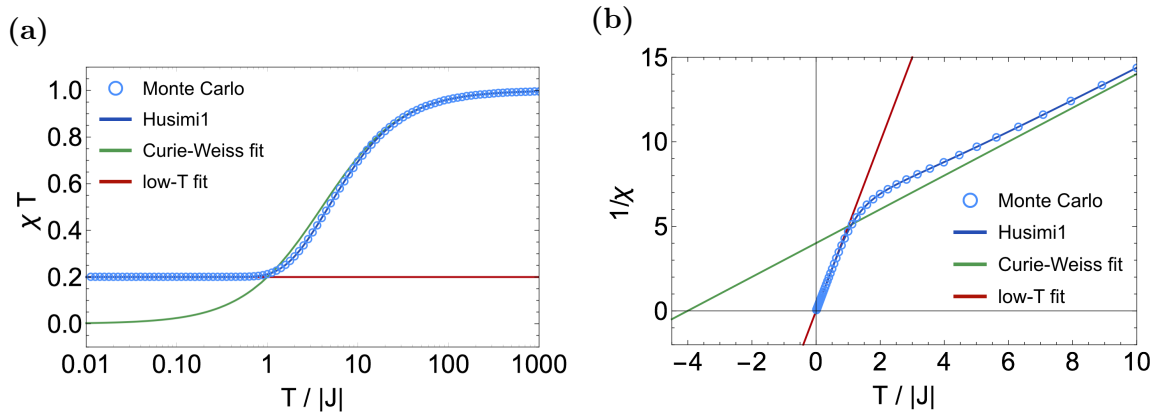

Figure 3.5: Limitations of Curie–Weiss law in spin liquids. Panel (a) shows the reduced susceptibility χT on a logarithmic scale for results of Monte Carlo simulations on the kagome lattice [Fig. 3.2(a)] (blue circles) with its corresponding results on "Husimi 1" (blue line), in comparison to their Curie–Weiss (green) and low–temperature (red) fits. Deviations from the Curie–Weiss law happen already at high temperatures at $T/|J| \sim 10$ and give qualitatively different results at temperatures below $T/|J| < 1$. Panel (b) shows the same results plotted for the inverse susceptibility $1/\chi$ on a linear plot, as commonly done to present experimental data. The exact result of "Husimi 1" shows two different slopes at high and low temperatures, corresponding to the two different Curie–laws.

Husimi 3:

$$\frac{1}{\chi} = T\frac{3e^{\frac{2}{T}} - e^{-\frac{6}{T}} + 2}{2\left(e^{-\frac{6}{T}} + 1\right)} = T\left(1 - \frac{-6}{T}\left(1 + \frac{1}{T} - \frac{4}{3T^2} + \dots\right)\right), \tag{3.25}$$

$$C = 1\,, \tag{3.26}$$

$$\theta_{\mathrm{cw}} = -6\,, \tag{3.27}$$

$$\Delta(T) = \frac{1}{T} - \frac{4}{3T^2} + \mathcal{O}(T^3)\,. \tag{3.28}$$

The deviation $\Delta(T)$ of θ_{cw} scales independently of the type of the Husimi tree with $1/T$ in leading order. However, the deviation in higher–order terms differs between Husimi trees, made of triangular plaquettes and square plaquettes.

To visually emphasise its experimental relevance, the result for "Husimi 1" has been plotted in Fig. 3.5 together with its Curie–Weiss ($T \to \infty$) and its low–temperature fits ($T \to 0$). Fig. 3.5(a) presents the reduced susceptibility χT, whereas Fig. 3.5(b) shows the inverse susceptibility $1/\chi$. From Fig. 3.5(a) it is visible that exact results for "Husimi 1" (blue curve) deviate from the Curie–Weiss fit (green curve) already at high temperatures ($T/|J| \sim 10$) and show different values at temperatures below $T/|J| \sim 1$. On the other side, the low–temperature fit (red curve) is only valid below $T/|J| \sim 1$. This effect is even more pronounced in Fig. 3.5(b), where the slope of $1/\chi$ shows two different values at high and low temperatures, indicating the two different Curie–laws.

From those comparisons it is visible that a high–temperature Curie–Weiss law does not give a proper description of the low–temperature physics in spin liquids, since it does not capture the crossover between two different Curie regimes.

3.5 Conclusions

Classical spin liquids, as discussed here for the simple Ising model on a variety of corner sharing lattices in two and three dimensions, perform a Curie–law crossover between a high–temperature paramagnetic and a low–temperature collective paramagnetic regime. Results for thermodynamic properties like entropy S and reduced susceptibility χT account for this crossover, and could be calculated consistently with analytical Husimi tree calculations and numerical Monte Carlo simulations.

The Curie–Weiss law is recovered as the first order approximation of the high–temperature expansion of Husimi–tree calculations. However, to be precise, this fit should be done at particularly high temperature. Indeed, the Curie–law crossover extends over a broad range of temperatures (one or two orders of magnitude in the systems studied here). During the crossover, the Curie–Weiss temperature is not properly defined, which is the reason, why different fitting windows within this crossover region provide different results for a Curie–Weiss fit, as often seen in experiments. In most cases, using the Curie–Weiss temperature to measure the degree of frustration of a material remains qualitatively valid, but should only be used as a rough estimate. Furthermore, it turns out that, a Curie–Weiss fit, even done at sufficiently high temperatures, does not capture the crossover into a different Curie–law at low temperatures and might estimate wrong ground state properties. A possibly more helpful way of identifying low–temperature physics in spin liquids is given by the analysis of χT, which can be compared to analytical Husimi tree calculations. Hereby, thermodynamic properties do not depend on the dimensionality of the lattice, but rather on the type of unit cell and its connectivity. Depending on those properties, S and χT will show different values at low temperatures, allowing to identify spin liquids on different lattices [Tab. 3.1].

Discussions of the Husimi tree have been presented for systems with Ising degree of freedom, but can in principal be extended to Heisenberg models [128, 129], which would allow for a comparison to a broader range of materials.

Chapter 4

The Shuriken Lattice – reentrance in a novel Spin Liquid

"*Erquickung hast Du nicht gewonnen,*
Wenn sie dir nicht aus eigner Seele quillt."

Faust 1, Vers 568 f. (Faust)
Johann W. v. Goethe

Triangular and kagome lattices are showcase examples in frustrated magnetism. It was shown that the antiferromagnetic Ising model on those lattices reveals a very large residual entropy [69, 94]

$$\text{triangular} \quad S(0) = 0.3383 \qquad \frac{S(0)}{S(\infty)} \approx 0.49 \,, \tag{4.1}$$

$$\text{kagome} \quad S(0) = 0.50183 \qquad \frac{S(0)}{S(\infty)} \approx 0.72 \,, \tag{4.2}$$

which is a direct consequence of the presence of triangular units within the lattice. Hereby the corner sharing nature of the kagome lattice reduces the constraints on magnetic lattice sites, compared to the triangular lattice even further, allowing for $\sim 72\%$ of residual entropy at zero temperature.

Another lattice made of corner sharing triangles, but with different type of short–loops, is the "shuriken" (or square–kagome) lattice, as depicted in Fig. 4.1(a). The unit cell contains six sites with two symmetrically inequivalent sublattices, which very naturally provide the opportunity to introduce bond anisotropy. A tuning of this anisotropy allows to visit regions in the phase diagram, where magnetic disorder prevails down to zero temperature, in analogy to a quantum critical point. In the vicinity of this point, multiple disordered ground states give rise to a reentrant phenomenon, where low and high–temperature regimes are less correlated than the intervening classical spin liquid.

This chapter shall provide a detailed and precise understanding of the thermodynamic properties of the anisotropic shuriken lattice, by using complementary analytical and numerical techniques as Husimi tree calculations and Monte Carlo simulations.

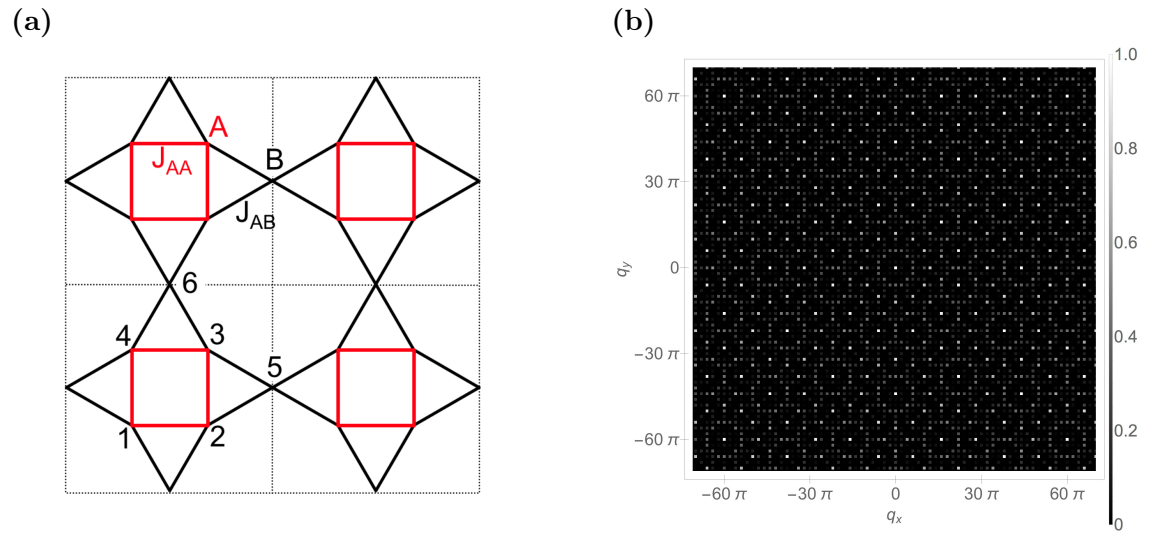

Figure 4.1: The shuriken lattice with six sites per unit cell and two sublattices A and B. (a) Exchange couplings between A sites are denoted as J_{AA} (red square plaquettes), while interactions between A and B sites are described with J_{AB} (black octagonal plaquettes). By convention the triangles have been chosen to be equilateral and therefore show irrational relative positions within the unit cell. (b) Distribution and intensity of Bragg peaks in reciprocal space $(\mathbf{q}_x, \mathbf{q}_y)$, as it would be measured in x-ray diffraction experiments on the shuriken lattice. While Bragg peaks are periodic and respect the symmetry of the shuriken lattice, their intensities do not [see explanations in Appendix C.1].

4.1 The anisotropic shuriken model

The shuriken lattice [204] – also known as square–kagome [205, 206, 207, 208, 209, 210, 211, 212], squagome [213, 214], squa–kagome [215], or L4-L8 [216] lattice – provides a model example for investigating multiple disordered phases and their competition to each other. Asymptotic limits of this asymmetry provided a promising S=1/2 zero–temperature phase diagram, ranging from bipartite long–range ordered phases to a highly degenerate ground sate of tetramer clusters of spins [215]. Even though the quantum ground states [204, 208, 212, 215] and influence of magnetic fields [206, 207, 208, 209, 204, 210, 217, 211] have been studied to some extent, knowledge about its finite–temperature properties in zero field is limited [205, 213].

The lattice structure is very similar to the celebrated kagome lattice, since it is composed of corner sharing triangles, but with the important difference of two inequivalent sub lattices and different types of smallest closed loops of size 4 and 8 [Fig. 4.1(a)]. As a consequence, the unit cell consists of six sites, where 2/3 of the spins belong to sublattice A and 1/3 to sublattice B. The coupling constants connecting the A sites on the square plaquettes are called J_{AA}, while couplings connecting the A and B sites on the octagonal plaquettes are called J_{AB}.

The Hamiltonian of the model can be written as

$$\mathcal{H} = -J_{\mathrm{AA}} \sum_{\langle ij \rangle_{\mathrm{AA}}} \sigma_i^{\mathrm{A}} \sigma_j^{\mathrm{A}} - J_{\mathrm{AB}} \sum_{\langle ij \rangle_{\mathrm{AB}}} \sigma_i^{\mathrm{A}} \sigma_j^{\mathrm{B}} \,, \tag{4.3}$$

where Ising spins take values of $\sigma_i = \pm 1$ and are coupled to their nearest neighbours.

For $J_{\mathrm{AA}} = +1$ the system does not show frustration and undergoes a phase transition with spontaneous $\mathbb{Z}_2$ symmetry breaking for $J_{\mathrm{AB}} \neq 0$. Thus the model shall be studied in the following just for $J_{\mathrm{AA}} = -1$. Energy and temperature scales are defined with respect to $|J_{\mathrm{AA}}|$, where thermodynamic properties are discussed as a function of the coupling ratio

$$x = \frac{J_{\mathrm{AB}}}{J_{\mathrm{AA}}} \,, \tag{4.4}$$

with positive and negative J_{AB}.

4.2 Finite–temperature phase diagram

This section deals with thermodynamic properties of the Ising model on the anisotropic shuriken lattice by evaluating the Hamiltonian of Eq. (4.3), which is invariant under the transformation

$$\sigma^{\mathrm{A}} \to -\sigma^{\mathrm{A}} \,, \quad J_{\mathrm{AB}} \to -J_{\mathrm{AB}} \,, \tag{4.5}$$

accounting also thermodynamic quantities such as energy E, specific heat C_h and entropy S to be invariant for a transformation between x and $-x$.

The phase diagram in Fig. 4.2(a) reveals a plethora of different phases, which shall be discussed in the following sections in detail. As a function of the coupling ratio x [Eq. (4.4)] the model supports long–range ordered ferromagnetic (FM) and ferrimagnetic (FiM) phases, with ground state configurations depicted for one unit cell respectively in Fig. 4.2(b) and (c). Two distinguishable classical spin–liquid phases (SL_1 & SL_2), are surround by a binary paramagnetic phase (BPM) which is made of antiferromagnetically ordered square plaquettes, decoupled from each other by intermediate decorrelated spins, on sublattice B [Fig. 4.2(d)].

All points in the phase diagram correspond to maxima in the specific heat. Open triangles represent crossovers, obtained from analytical Husimi tree calculations, whereas open circles correspond to phase transitions, obtained and classified by single spin flip Monte Carlo simulations. Technical details are presented in Section 2.1 and Section 2.2 respectively.

4.2.1 Long range–order: $|x| > 1$

When couplings on the octagonal plaquettes are dominating ($|x| \to \infty$), correlations between sites on the square plaquettes can be neglected. The model Hamiltonian in Eq. (4.3) transforms into a nearest–neighbour Ising model on the decorated square lattice, which is not frustrated and orders via phase transition of the 2D Ising universality class [218] by spontaneous $\mathbb{Z}_2$ symmetry breaking. The exact transition temperature

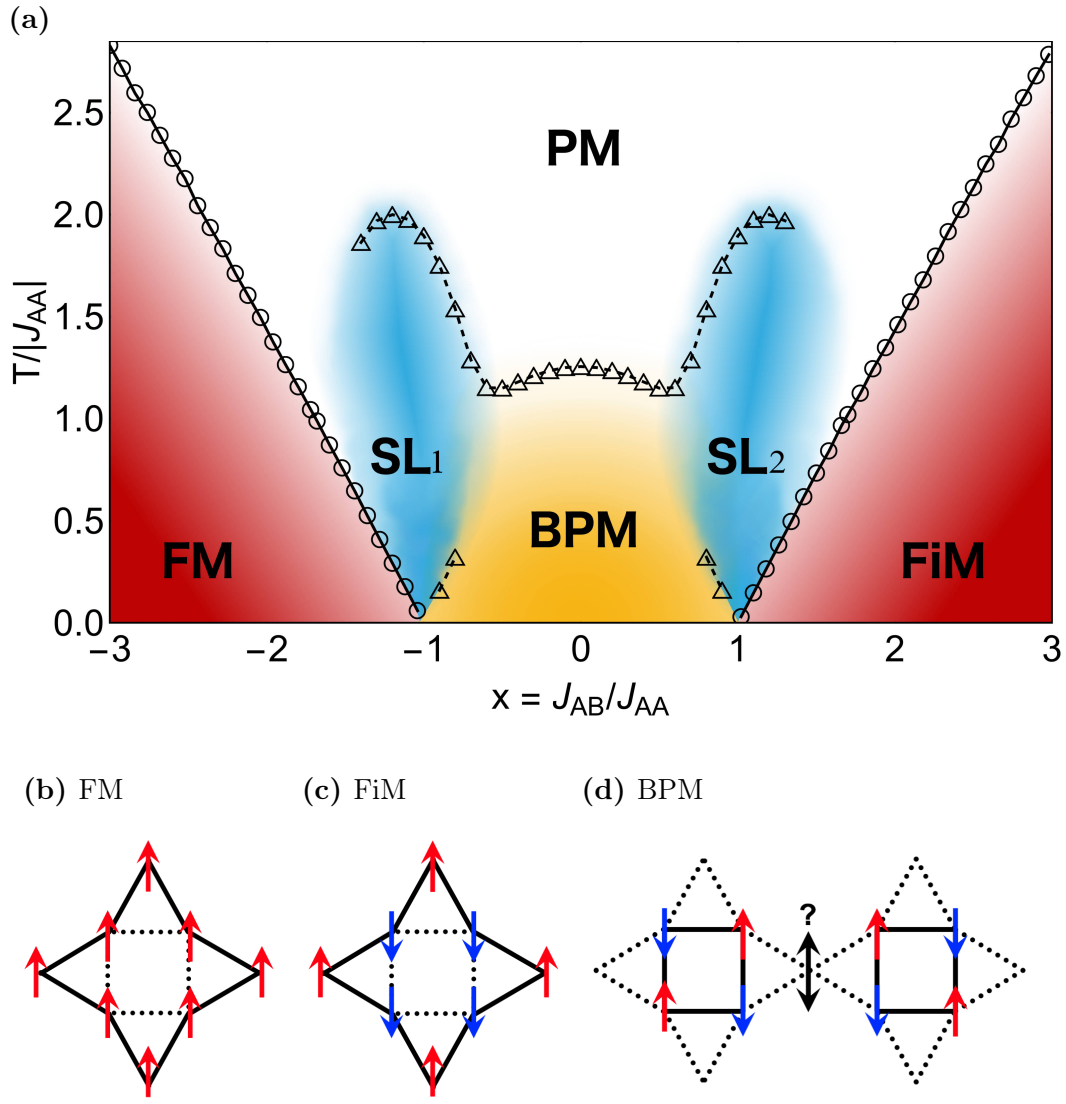

Figure 4.2: Phase diagram of the Ising model on the anisotropic shuriken lattice. (a) Circles (triangles) correspond to phase transitions (crossovers), obtained by Monte Carlo simulations (Husimi tree calculations). As a function of the coupling ratio x [Eq. (4.4)] the model supports long–ranged ordered ferromagnetic (FM) and ferrimagnetic (FiM) phases. Two classical spin liquid phases (SL_1 & SL_2) surround the binary paramagnetic phase (BPM), which is made of antiferromagnetically ordered square plaquettes, decoupled from each other by intermediate decorrelated spins, on sublattice B. (b) sample configuration of a ferromagnetic ground state. (c) sample configuration of a ferrimagnetic ground state. (d) sample configuration of a binary paramagnetic ground state.

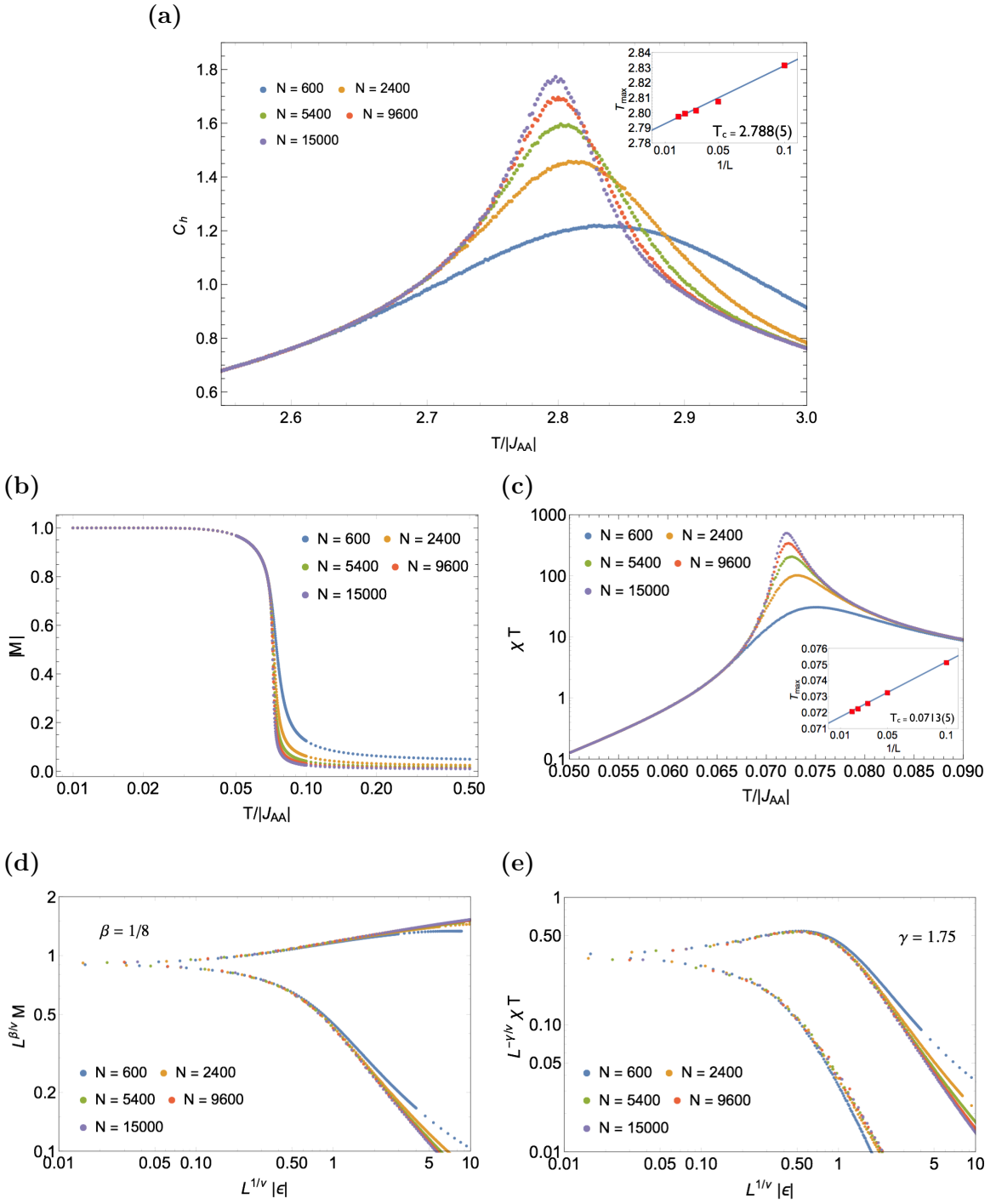

Figure 4.3: Thermodynamic properties and finite–size scaling for $x = -3$. (a) Specific heat for system sizes $N = \{600, 2400, 5400, 9600, 15000\}$. The inset presents finite–size scaling of the specific–heat maximum as a function of inverse system length $1/L$ with $L = \sqrt{N}$, allowing to estimate the phase transition temperature in the thermodynamic limit with $T_c = 2.788(5)$. (b) Magnetisation $|M|$ and (c) reduced susceptibility χT plotted for different system sizes. Respectively (d) and (e) show the scaling collapse for (b) and (c) by using critical exponents of the Ising 2D universality class [Eq. (4.9)].

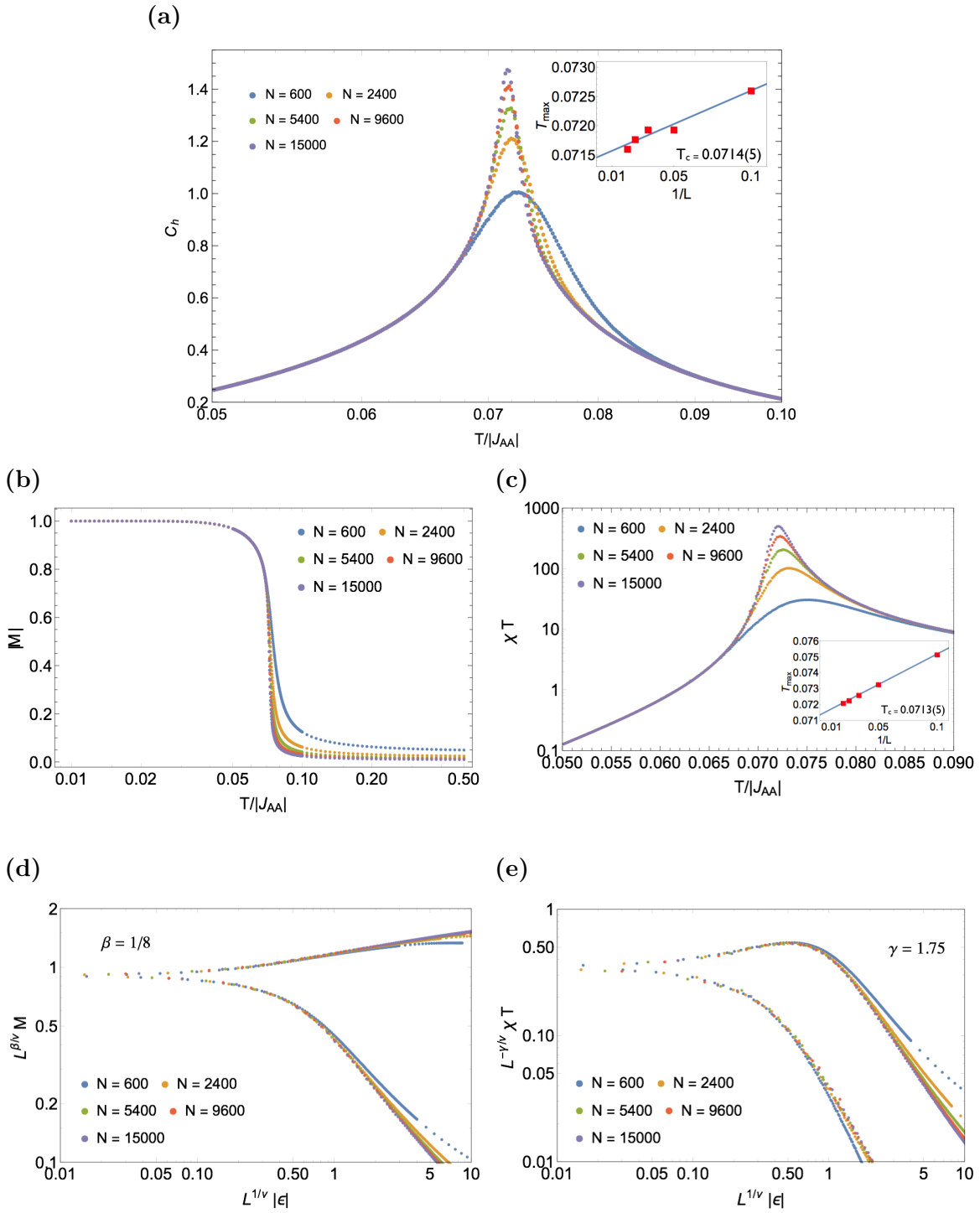

Figure 4.4: Thermodynamic properties and finite–size scaling for $x = -1.05$. (a) Specific heat for system sizes $N = \{600, 2400, 5400, 9600, 15000\}$. The inset presents finite–size scaling of the specific–heat maximum as a function of inverse system length $1/L$ with $L = \sqrt{N}$, allowing to estimate the phase transition temperature in the thermodynamic limit with $T_x = 0.0714(5)$. (b) Magnetisation $|M|$ and (c) reduced susceptibility χT plotted for different system sizes. Respectively (d) and (e) show the scaling collapse for (b) and (c) by using critical exponents of the Ising 2D universality class [Eq. (4.9)].

for this case can be calculated by using the decoration–iteration transformation [1].

$$T_{\mathrm{c}} = \frac{2J_{\mathrm{AB}}}{\ln\left(\sqrt{2}+1+\sqrt{2+2\sqrt{2}}\right)} \approx 1.30841\ J_{\mathrm{AB}}\ . \tag{4.6}$$

The 2D Ising universality class persists down to $|x| \to 1^{+}$, as shown by finite size scaling with Monte Carlo simulations at points $x = -3$ and $x = -1.05$ in Fig. 4.3 and Fig. 4.4 respectively. By symmetry of the Hamiltonian [Eq. (4.3) and Eq. (4.5)], the results also directly apply for $x > 1$.

Finite size scaling for systems sizes $N = \{600, 2400, 5400, 9600, 15000\}$ provides a phase transition temperature T_{c} of

$$x = -3 \Rightarrow T_{\mathrm{c}} = 2.788(5)\ , \tag{4.7}$$

$$x = -1.05 \Rightarrow T_{\mathrm{c}} = 0.0714(5)\ . \tag{4.8}$$

Based on T_{c} the reduced temperature $\epsilon - (T - T_{\mathrm{c}})/T_{\mathrm{c}}$ has been used to scale the absolute magnetisation $|M| = |\sum_i^N \sigma_i|$ and the magnetic susceptibility [Eq. (2.45)] as done in the literature [148]. As confirmed in Fig. 4.3 and Fig. 4.4 the phase transition belongs to the 2D Ising universality class, as shown by a scaling collapse of the magnetisation M and reduced susceptibility χT by using the critical exponents

$$\beta = 0.125\ , \quad \gamma = 1.75\ , \quad \nu = 1\ . \tag{4.9}$$

For $x < -1$ and $x > 1$ the system shows respectively ferromagnetic [Fig. 4.2(b)] and ferrimagnetic [Fig. 4.2(c)] ground states. The staggered magnetisation of the latter one comes from all A–spins on the square plaquettes pointing in one direction, whereas the other spins take an antiparallel configuration. This effect leads to the rather uncommon consequence of a finite magnetisation if both couplings J_{AA} and J_{AB} are antiferromagnetic, reminiscent of Lieb ferromagnetism [219] as presented in Ref.[215] for quantum spins.

4.2.2 Binary paramagnet: $|x| < 1$

For low temperatures the phase diagram [Fig. 4.2(a)] shows for $|x| < 1$ an extended binary paramagnetic (BPM) regime, surrounded by two spin liquid phases (SL_1 & SL_2). A sample configuration of this state is shown in Fig. 4.2(d), where antiferromagnetically ordered square–plaquettes are decorrelated via intervening spins on sublattice B. The antiferromagnetic square–plaquettes locally order in two different configurations, equivalent to a superspin Ξ with Ising degree of freedom:

$$\Xi = \sigma_1^{\mathrm{A}} - \sigma_2^{\mathrm{A}} + \sigma_3^{\mathrm{A}} - \sigma_4^{\mathrm{A}} = \pm 4\ , \tag{4.10}$$

with site indices given in Fig. 4.1(a). These superspins refer to a classical analogue of tetramer objects observed in the S=1/2 model on the shuriken lattice in Ref. [215]. Those superspins Ξ are perfectly decoupled from the B sites at zero temperature, due to the frustration on the J_{AB} bonds. The system then forms two interpenetrating square lattices, one made of super spins, the other one made of sites on the B sites. In

analogy to binary mixtures of liquids and gases, this phase shall be referred to as *binary* paramagnetic phase. While the decomposition into two independent paramagnetic phases is rather exotic, decorrelation of clusters of spins is not uncommon in frustrated systems. It is for example reminiscent of the decorrelation between one–dimensional chains in the hollandite [220] and kagome lattices [221, 222, 223], and between two–dimensional planes in the breathing pyrochlore lattice [224].

The absence of correlations beyond square plaquettes at $T \to 0$ allows to estimate the ground–state entropy in the BPM phase. Let N_{uc} be the number of unit cells with $N = 6N_{\mathrm{uc}}$ total spins in the lattice There are $2N_{\mathrm{uc}}$ decorrelated spins on the B sites per unit cell, giving rise to an extensive ground–state entropy

$$S_{\mathrm{BPM}} = k_{\mathrm{B}} \ln(2^{N_{\mathrm{uc}}} 2^{2N_{\mathrm{uc}}}) = \frac{N}{2} k_{\mathrm{B}} \ln 2 \,, \tag{4.11}$$

which turns out to be half the entropy of an Ising paramagnet. The magnetic susceptibility, measuring the normalised variance of the magnetisation in the system [Eq. (2.45)] can be written as the reduced susceptibility χT

$$\chi\, T = \frac{1}{N} \left(\sum_{i,j} \langle \sigma_i \sigma_j \rangle - \langle \sigma_i \rangle \langle \sigma_j \rangle \right) , \tag{4.12}$$

$$= 1 + \frac{1}{N} \sum_{i \neq j} \langle \sigma_i \sigma_j \rangle \,, \tag{4.13}$$

which converges to a finite value in BPM phase of

$$\lim_{T \to 0} \chi\, T \Big|_{\mathrm{BPM}} = \frac{1}{3} \,. \tag{4.14}$$

This result should be compared to the high–temperature phase $\chi\, T \Big|_{\mathrm{PM}} = 1$.

4.2.3 Classical spin liquid: $|x| \sim 1$

The Ising model on the isotropic shuriken lattice ($|x| = 1$), can be seen as a classical analogue of quantum critical points, which sit in between ordered and disordered phases, resulting in a persistence of spin–liquid behaviour at finite temperatures (blue regions) and continuously connects them to the high-temperature paramagnet.

The large entropy of the classical spin liquids SL_1 & SL_2 spreads to neighbouring regions of the phase diagram for $|x| \sim 1$ and $T > 0$. Since the model stabilises a classical spin liquid above a long–ranged ordered phase for $|x| \gtrsim 1$, the system undergoes by cooling the evolution "gas $\xrightarrow{\text{crossover}}$ liquid $\xrightarrow{\text{transition}}$ solid". Classical spin liquids generally show such properties, when adiabatically tuned away from their high–degeneracy point, as observed in e.g. Heisenberg antiferromagnets on the kagome [225] or pyrochlore [226, 227] lattice. On the other side for $|x| \lesssim 1$ the system shows a reentrant behaviour by evolving "gas $\xrightarrow{\text{crossover}}$ liquid $\xrightarrow{\text{crossover}}$ gas" upon cooling, which shall be discussed in detail in the following section.

$T \to 0^+$	Monte Carlo	Husimi tree	exact
$S(\lvert x\rvert = 1)$	0.504(1)	$\frac{1}{6}\ln\frac{41}{2} \approx 0.5034$	n/a
$\chi T(x = 1)$	0.203(1)	0.2028	n/a
$\chi T(x = -1)$	1.77(1)	1.771	n/a
$S(\lvert x\rvert < 1)$	0.347(1)	$\frac{1}{2}\ln 2 \approx 0.3466$	$\frac{1}{2}\ln 2$
$\chi T(\lvert x\rvert < 1)$	0.333(1)	$\frac{1}{3}$	$\frac{1}{3}$

Table 4.1: Entropy S and reduced susceptibilities χT for $T \to 0^+$ with coupling ratios $|x| \leq 1$. Results were obtained by numerical Monte Carlo simulations, analytical Husimi tree calculations and exact solutions for the binary paramagnet. All quantities are normalised to the number of spins N, with the Boltzmann constant $k_\mathrm{B} = 1$.

4.3 Reentrance of disorder

4.3.1 Double crossover

Fig. 4.5 shows thermodynamic properties, such as energy E, specific heat C_h, entropy S and reduced susceptibility χT [Eq. (4.13)] as a function of temperature $T/|J_{\mathrm{AA}}|$ for different points $|x| \leq 1$. The obtained results from numerical Monte Carlo simulations and analytical Husimi tree calculations agree remarkably well and confirm that the classical spin liquid and binary paramagnet persist down to zero temperature for $|x| = 1$ and $|x| = 0$ respectively.

The system shows for $|x| = 0.9$ [Fig. 4.5(b)] a double crossover, indicated by two local maxima in the specific heat C_h and a stepwise decrease of the entropy S. C_h and χT are independent of the system size in Monte Carlo simulations [Fig. 4.6], confirming with the absence of finite size effects that the system does not perform a phase transition, rather than a crossover. The crossover persists until $0.5 \leq |x| < 1$, where the system evolves upon cooling from a high–temperature paramagnet into a classical spin liquid before entering the binary paramagnet. The spin liquid provides an entropy plateau for $|x| = 0.9$ [Fig. 4.5(b)], at the same value as for the low–temperature regime for $|x| = 1$ [Fig. 4.5(a)]. All relevant thermodynamic quantities are summarised in Tab. 4.1.

The Hamiltonian is invariant via the mapping of $x \to -x$ [Eq. (4.5)] and therefore preserves energy, specific heat and entropy, but not the magnetic correlations. Correlations in classical spin liquids give rise to a Curie–law crossover (see Chapter 3) between different 1/T asymptotic regimes of the susceptibility, as also observed in

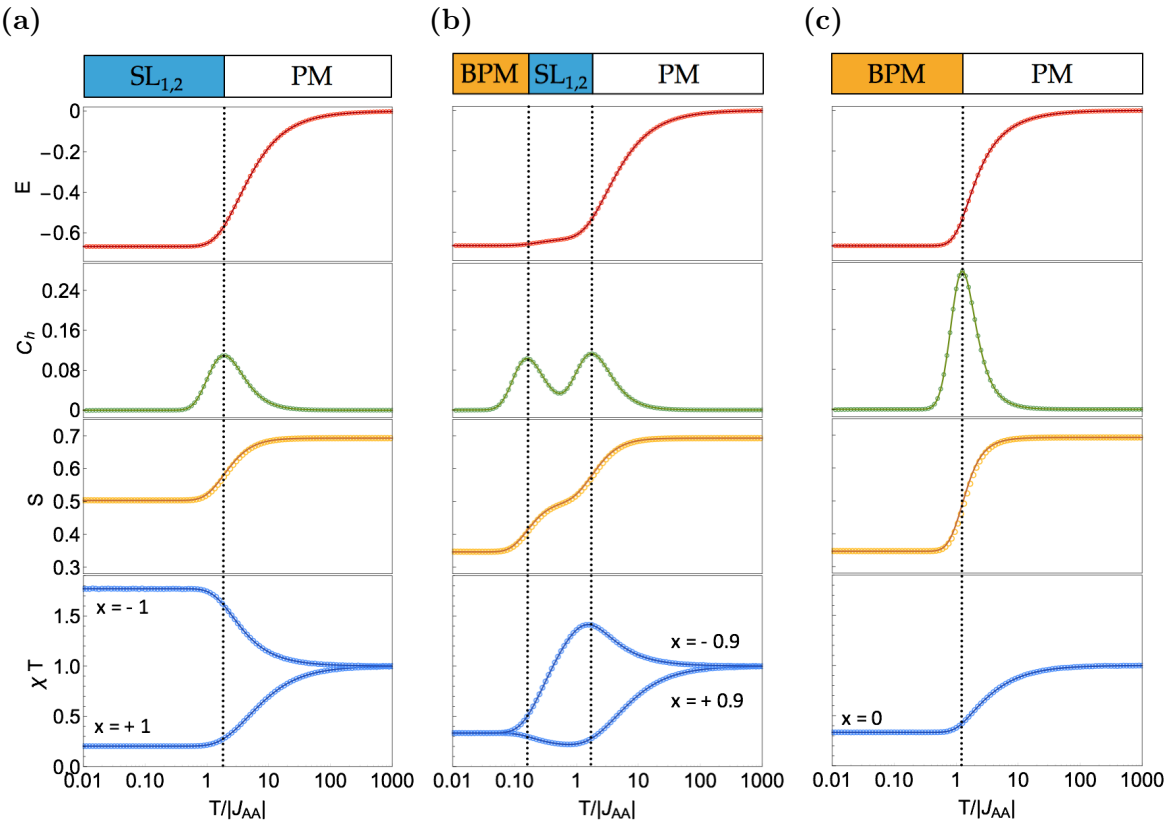

Figure 4.5: Thermodynamic properties for different coupling ratios x showing both, single and multiple Curie–law crossovers. Energy E, specific heat C_h, entropy S and reduced susceptibility χT are shown for (a) $x = \pm 1$, (b) $x = \pm 0.9$ and (c) $x = 0$. The absence of singularities (phase transitions) for this set of parameters is the reason why Monte Carlo simulations (open circles) and Husimi tree calculations (solid lines) match that well. For $|x| = 0.9$ the system shows a double crossover, where the low–temperature regime is the same as for $x = 0$. The entropy is obtained by numerical integration of C_h/N and setting $S(T \to +\infty) = \ln 2$. Vertical dotted lines represent the estimated crossover temperatures. All quantities are normalised to the number of spins N, with the Boltzmann constant $k_\mathrm{B} = 1$.

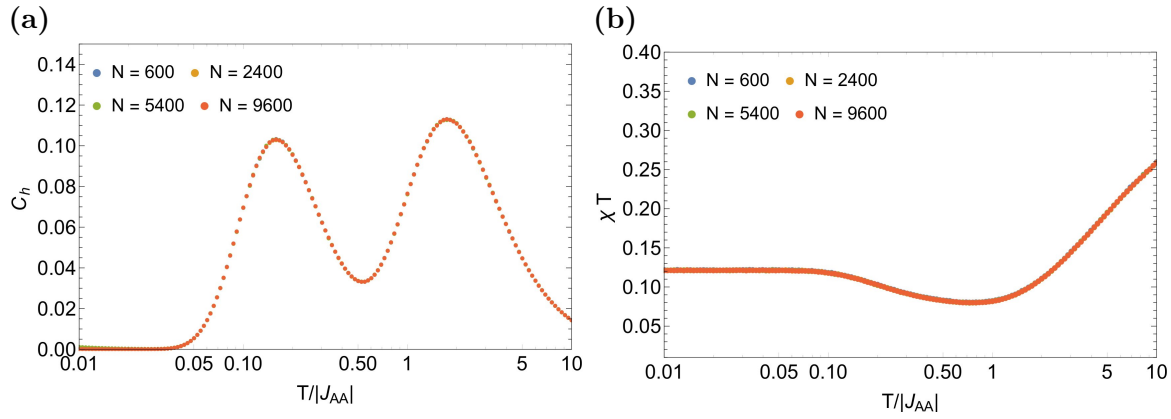

Figure 4.6: Finite–size evolution in the double–crossover region for $x = 0.9$. Absence of finite size effects in Monte Carlo simulations for different cluster sizes shown in the specific heat in (a) and reduced susceptibility (b). The system sizes used here are much bigger than the average correlation length [Fig. 4.8], which is why the numerical results for all system sizes lay on top of each other.

pyrochlore [142, 228, 229, 230], triangular [231] and kagome [231, 221, 232] systems. The same effect is also observed in the shuriken lattice for $x = \{-1, 0, 1\}$ [Fig. 4.7]. However, for $0.5 < |x| < 1$ in the double crossover region the reduced susceptibility becomes non–monotonic. χT first tend towards the values of spin liquids SL_1 (SL_2) for $x < 0$ ($x > 0$), before converging to $1/3$ for the binary paramagnet, as shown in $x = \{-0.99, -0.9, 0.9, 0.99\}$ in Fig. 4.7. In general and beyond the current problem, the multistep Curie–law crossover underlines the advantages of the reduced susceptibility to identify intermediate magnetic regimes, and the classification of different phases.

A detailed discussion about the Curie–law crossover and the limitations of the Curie–Weiss law in spin liquids took place in Chapter 3. In this context, the example of the shuriken lattice is outstanding, since non–monotonic correlations would produce a qualitatively wrong estimate of the low–temperature properties from a high–temperature Curie–Weiss fit. For example $x = -0.9$ [Fig. 4.5(b)] would predict dominating ferromagnetic correlations by taking a high–temperature Curie–Weiss fit above $> 5T/|J_{AA}|$, whereas the low–temperature physics are obviously dominated by antiferromagnetic correlations.

4.3.2 Correlation function in real and momentum space

The non–monotonic behaviour of χT goes along with a non–monotonic behaviour of the correlation length. The function C_ρ measures the correlations between a central spin σ_0 and all spins at distance ρ. One needs to distinguish between sublattice A and B, since connectivities and symmetries for both is different. Let D_ρ^X be the ensemble of sites at distance ρ from a given spin σ_0^X on the $X = \{A, B\}$ sublattice. The real–space

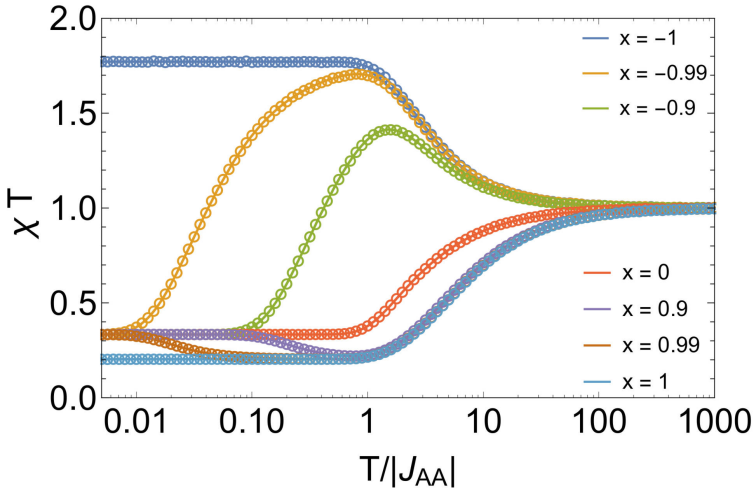

Figure 4.7: Reduced susceptibility χT for coupling ratios $x = \{0, \pm 1, \pm 0.9, \pm 0.99\}$. Results are obtained from numerical Monte Carlo simulations (circles) and analytical Husimi tree calculations (solid lines). Since the system performs a standard Curie law crossover for $x = \{\pm 1, 0\}$ seen as a monotonic behaviour of χT, the system shows a multistep behaviour for intermediate values of x due to a double crossover. The asymptotic low–temperature values for χT are given in Tab. 4.1.

correlation function is defined as

$$C_\rho^X = \frac{\sum_{i \in D_\rho^X} |\langle \sigma_0^X \sigma_i \rangle|}{\sum_{i \in D_\rho^X}} , \tag{4.15}$$

where the absolute value accounts for antiferromagnetic correlations. The energy integrated structure factor $S(\mathbf{q})$ provides information about spin–correlations in momentum space

$$S(\mathbf{q}) = \langle \sigma_{\mathbf{q}} \sigma_{-\mathbf{q}} \rangle = \left\langle \left| \frac{1}{\sqrt{N}} \sum_i^N \mathrm{e}^{\mathrm{i}\mathbf{q}\mathbf{r}_i} \sigma_i \right|^2 \right\rangle . \tag{4.16}$$

The correlation functions on both sublattices C_ρ^A and C_ρ^B are plotted in Fig. 4.8. For $x = -1.05$ [Fig. 4.8(a) and (b)] the system orders below the critical temperature $T_\mathrm{c} = 0.0714(5)$ [Fig. 4.4(a)], seen in $C_\rho = 1$ over long–length scales. Above the phase transition, the correlations decay exponentially.

At $x = -1$ [Fig. 4.8(c) and Fig. 4.8(d)] the correlations still decay exponentially, down to the lowest temperatures, as confirmed by a quantitative superimposition of data points. The correlation length reaches a maximum value of $\xi \approx 0.3$ and effectively retains this value up to $T \sim 1 J_{AA}$, until thermally excited defects destroy them. However, exponentially decaying correlations should not be confused with paramagnetic ones, as seen in their strongly inhomogeneous structure factor $S(\mathbf{q})$ [Fig. 4.9(a) and Fig. 4.9(c) and supplemental material of Ref. [1]].

Also, the $S(\mathbf{q})$ in the spin liquid regimes is aperiodic, which is uncommon for regular lattices. However, analysing the shuriken lattice structure with equilateral

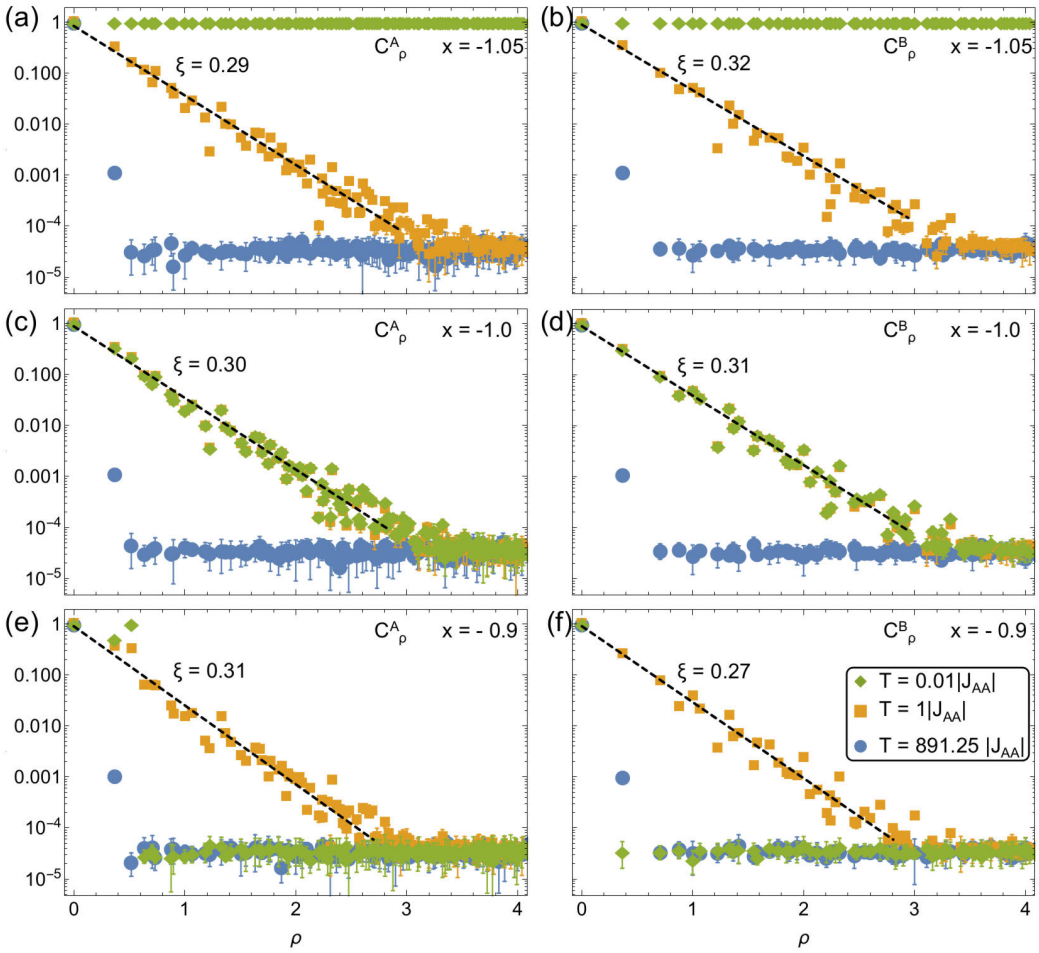

Figure 4.8: Spin–spin correlations in the vicinity of the spin liquid phases. (a) and (b) for $x = -1.05$ show order below the critical temperature [Eq. (4.8)], a finite correlation length for temperatures of the order of the coupling constant and no correlation between neighbouring sites at high temperatures. (c) and (d) for $x = -1$ show no order at any temperature, but a correlation length characteristic for the spin liquid phase, which remains constant for all temperatures below $\sim |J_{AA}|$. (e) and (f) for $x = -0.9$ show no correlations between neighbouring sites at very high (paramagnetic regime) and very low temperatures (binary paramagnetic regime). However, intermediate temperatures show a finite correlation length coming from the spin liquid regime. This non–monotonic behaviour of the correlation length illustrates the reentrant nature between paramagnetic regimes. The agglomeration of data points around $C \sim 2 \times 10^{-5}$ comes from finite size effects. The blue datapoint at $\rho \approx 0.4$ and $C \approx 0.001$ comes from the fact that the simulations were performed at high but not infinite temperatures.

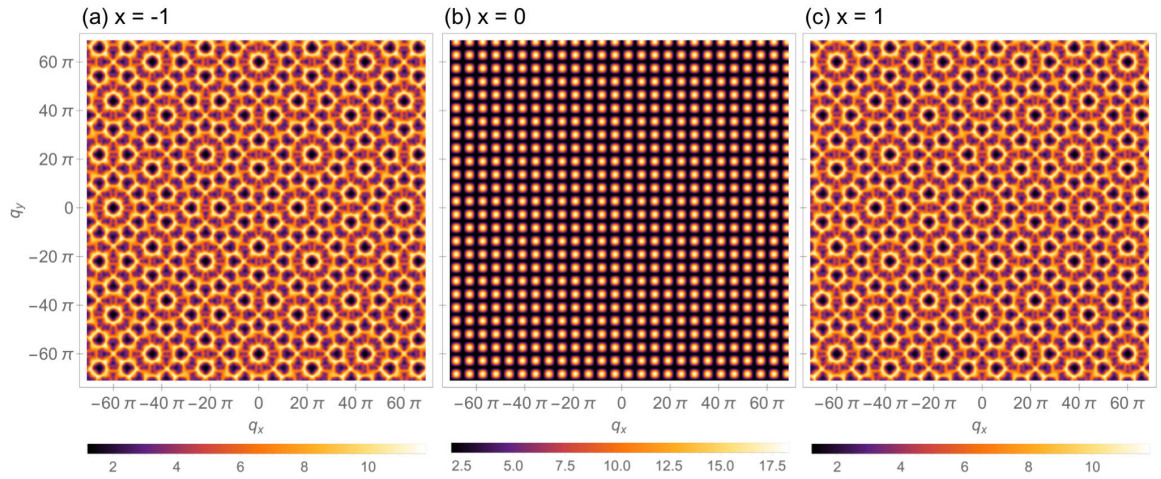

Figure 4.9: Equal–time structure factor $S(\mathbf{q})$ at zero temperature. (a) and (c) show the $S(\mathbf{q})$ for $x = \pm 1$ in the spin liquid regime, characterised by the absence of any Bragg peaks. Aperiodic features are caused by the irrational relative coordinates of sites within the unit cell of the shuriken lattice with equilateral triangles. The $S(\mathbf{q})$ for the shuriken lattice with non–equilateral triangles is presented in the Appendix C.3. The similarity of $S(\mathbf{q})$ for x = -1 and x = 1 comes from the symmetry between the two models [Eq. (4.5)]. (b) shows the $S(\mathbf{q})$ for $x = 0$ in the binary paramagnetic regime. The black background represents the absence of correlations beyond the size of the superspins, living on square plaquettes. The finite extension of superspins in real-space is reasonable to the finite extension of the dots of scattering in momentum space. To recover ergodicity, a local "multi–spin" update flipping four spins of the square plaquettes has been used. A video showing the temperature evolution of $S(\mathbf{q})$ at $x = 0.9$ is available in the supplemental material of Ref. [1].

triangles shows, that distances between lattice sites are irrational, and do not satisfy $e^{i\mathbf{q}\mathbf{r}_i} = e^{i(\mathbf{q}+\mathbf{Q})\mathbf{r}_i}$, from Eq. (4.16), with $\mathbf{Q}$ a reciprocal lattice vector. However, the $S(\mathbf{q})$ will become periodic by choosing a shuriken unit cell, which contains non-equilateral triangles as shown in Appendix C.3.

In the double–crossover region at $x = -0.9$ [Fig. 4.8(e) and (f)] the correlation function becomes non–monotonic with temperature. In the binary paramagnet the A sites show a finite cutoff after the size of a square plaquettes (super spins), where the B sites become perfectly decorrelated. This can also be seen in the $S(\mathbf{q})$ at $x = 0$ [Fig. 4.9(b)], where correlations are just restricted to a finite region in momentum space, with absence of correlations along the lattice directions.

4.3.3 Experimental realisations

The Ising model on the anisotropic shuriken lattice provides a conceptually interesting model for reentrance behaviour between disordered phases. Unfortunately, experimental realisations have not been found yet. However, several directions of possible experimental realisation are possible, each of them with their advantages and drawbacks.

The shuriken topology has been observed, albeit hidden, in the material dysprosium aluminium garnet (DAG) [233, 234] (see Ref. [235] for a review). A projection of complex coupling interactions from the three–dimensional material into the [001] direction recovers an effective Ising model on the shuriken lattice. However, its microscopic Hamiltonian does not respect the same symmetry as the model studied here [Eq. (4.3)] and shows ferrimagnetic order. Nevertheless, it shows that the shuriken topology can exist in real materials and calls for further investigations.

Cold atoms might offer an alternative way, since the necessary experimental setup for an optical shuriken lattice has been proposed in the literature [214]. However, the most promising possibility might be provided by artificial lattices, where ferromagnetic nano islands effectively behave like Ising spins. Since various lattice types can be engineered by lithography, the production of a shuriken geometry should not be an issue. Nano islands have been grown with magnetisation axis the in $\mathbf{z}$ direction, perpendicular to the lattice [236, 237, 238]. Since interactions between these islands will decay quickly in space (dipolar interactions), at a nearest neighbour level, a physical distortion of the shuriken geometry would reproduce the anisotropy of Eq. (4.3) for $x > 0$. Further nearest–neighbour interactions are expected to lift the extensive–ground state degeneracy of models for $|x| \leq 1$, giving rise to a low–temperature phase transition. Simulations for the closely related kagome lattice predict such a transition at $T/|J| \approx 0.03$ [238], which offers an appreciable temperature range to observe the phase diagram in Fig. 4.2(a) in artificial lattices.

4.4 Conclusions

The Ising model on the anisotropic shuriken lattice supports a plethora of different phases as a function of the anisotropy parameter $x = J_{\mathrm{AB}}/J_{\mathrm{AA}}$. Two long–range ordered phases (ferromagnetic and ferrimagnetic) occur for $|x| > 1$ by a continuous phase transition, as part of the 2D Ising universality class. In a broad region $|x| \lesssim 1$ three disordered phases evolve [Fig. 4.2(a)], where a binary paramagnetic (BPM) phase, composed of locally ordered square plaquettes and completely decorrelated by single spins on the B sites [Fig. 4.2(d)], is surrounded by two classical spin liquids $\mathrm{SL}_{1,2}$. Thermal fluctuations spread the classical spin liquids $\mathrm{SL}_{1,2}$ beyond the singular points $x = \pm 1$ and allow for a double crossover from a high–temperature paramagnet to a correlated spin liquid and to a binary paramagnet (BPM) for $|x| \lesssim 1$. This process can be considered as a reentrant behaviour [239, 240, 241, 242, 243] between disordered regimes, in absence of phase transitions. Such a competition of disordered phases has been quantified by a double–peak features in the specific heat, a stepwise decrease of the entropy and a multi–step Curie–law crossover [see Fig. 4.5, Fig. 4.7 and Fig. 4.8]. As such, it represents an interesting mechanism to stabilise a paramagnetic (gas–like phase) at temperatures below the regime of a classical spin–liquid phase.

Additionally the shuriken lattices showed its properties as a distorted frustrated magnet, where extended regions of magnetic disorder can be stabilised by anisotropy or further neighbour exchange, as on Cairo [216, 244], hollandite [220], kagome [221, 222, 223], and pyrochlore [245, 224, 246] lattices. Such connections are particular promising since it enlarges the possibility of experimental realisations of, e.g. Volborthite [220]

or breathing pyrochlores [247, 248].

Possible future directions of this work might involve thermodynamic and dynamic investigations of the classical Heisenberg model on the shuriken lattice, which is supposed to also provide an extensive ground state degeneracy at $|x| = 1$ [208, 215]. In analogy to the antiferromagnetic Heisenberg model on the kagome lattice, order-by-disorder effects are expected to play a role, able to form spin waves or zero–energy excitations comparable to the weather vane modes on the kagome lattice.

Applying an external magnetic field [207, 211] would provide a tool to directly break the invariance given by Eq. (4.5), making the phase diagram of Fig. 4.2(a) asymmetric.

Chapter 5

Origin of spin liquid behaviour in $Ca_{10}Cr_7O_{28}$

" *Ein jeder lernt nur, was er lernen kann;*
Doch der den Augenblick ergreift,
Das ist der rechte Mann."

Faust 1, Vers 2017 ff. (Mephistopheles)
Johann W. v. Goethe

The physical realisation of spin liquids and their fundamental understanding is a central theme in frustrated magnetism. However, despite intensive research, just few experimental candidates have been proposed.

This chapter shall present the new spin–liquid candidate $Ca_{10}Cr_7O_{28}$, a physical realisation of a S=1/2 magnet on the bilayer breathing kagome (BBK) lattice. $Ca_{10}Cr_7O_{28}$ received little attention until Balz *et al.* recently reported the possibility of a quantum spin liquid ground state, by applying a range of experimental techniques and functional renormalisation group calculations [127, 249, 250]. Next to other evidences, supporting the possibility of a spin liquid ground state, inelastic neutron scattering (INS) data show high intensity "ring" features at low energies and bow–tie–like features at finite energies.

The aim of this chapter is to deepen the understanding of the spin liquid behaviour in $Ca_{10}Cr_7O_{28}$ by comparing the dynamical signatures of INS experiments to numerical simulations of the Heisenberg model on the BBK lattice and extract their physical origin. A combination of classical Monte Carlo [Section 2.2] and molecular dynamics [Section 2.3] simulations could provide high–resolution spin–spin correlation functions, comparable to INS results of $Ca_{10}Cr_7O_{28}$. In particular, the origin of the distinct "ring" features in INS data could be identified by mapping the BBK model onto the J_1-J_2 honeycomb model. This model shows in the relevant region of the phase diagram the coexistence of different spiral phases, which allow for the emergence of a degenerate ground–state manifold. Additionally, broad bow–tie–like features at higher energies in INS data can be shown to evolve into sharp pinch–points for transverse spin excitations in finite field, similar to those of the classical antiferromagnetic Heisenberg model on the kagome lattice [Fig. 1.7(b) in Section 1.3.2].

5.1 Synthesis of $Ca_{10}Cr_7O_{28}$

$Ca_{10}Cr_7O_{28}$ is related to the quantum–dimer systems $A_3Cr_2O_8$ (A = Sr, Ba) and contains Cr ions located within oxygen tetrahedra. These Cr ions are arranged on distorted triangular bilayers, following the trigonal space group $R3c$. The first reported crystallographic study of $Ca_{10}Cr_7O_{28}$ dates back to 1981, where Gyepesová *et* al. [251] obtained the correct space group but the incorrect chemical composition $Ca_3Cr_2O_8$ in analogy to $A_3Cr_2O_8$ (A = Sr, Ba) compounds. Furthermore, partial occupancies led to the empirical formula of $Ca_{10.07}Cr_7O_{27.58}$, which provided a rather unsatisfying crystal structure model.

Arčon et al. [252] published in 1998 X-ray absorption data, which suggested a charge order of Chromium with two different valences, Cr^{5+} and Cr^{6+} in the ratio 6:1. The average valence for Cr of 5.14 was consistent with experimental observations, allowing to provide the correct formula of $Ca_{10}(Cr^{5+}O_4)_6(Cr^{6+}O_4)$. However the location of the non–magnetic Cr^{6+} could not be determined at that point.

In a recent paper from 2013, Gyepesová *et* al. revised the crystal structure of this compound and published a more detailed diffraction study [253]. However, in 2017 Balz *et* al. [250] solved the crystal structure by using x-ray diffraction on single crystals, confirming $Ca_{10}Cr_7O_{28}$ to be a mixed valence compound with ordered Cr^{6+} ions.

While Cr^{6+} is non–magnetic, the Cr^{5+} ion has a single electron in its outermost shell, providing a $S = 1/2$ moment to the magnetic properties of the system. The crystallographic lattice structure of these magnetic ions form a stacked version of kagome bilayers, which shall be investigated in more detail in Section 5.3 of this chapter. As outlined in the next section, Balz *et* al. [127, 249, 250] could confidently show the absence of long–range order down to 19 mK and provide strong evidence for $Ca_{10}Cr_7O_{28}$ to be a spin liquid.

5.2 Thermodynamic properties in $Ca_{10}Cr_7O_{28}$

Generally, it is much harder to show the absence, than the presence of order in magnetic materials. This is one of the reasons, why Balz *et* al. [127, 249, 250] needed an extensive set of experiments to comprehensively conclude the evidence for a spin liquid behaviour in $Ca_{10}Cr_7O_{28}$.

The first indication of absence of magnetic order has been seen in low–temperature specific heat measurements [127], as reproduced in Fig. 5.1(a). The heat capacity C_p shows a broad maximum at T = 3.1 K, indicating the onset of short–ranged magnetic fluctuations, comparable to a Curie–law crossover (see Chapter 3), which is followed by a weak kink at 0.46 K.

Fig. 5.1(b), reproduced from [249], shows the magnetic heat capacity divided by temperature C/T, as a function of temperature for various values of magnetic field up to 14.5 T. C/T at low temperatures is characterised by a smooth and rapid increase for low fields, while showing a change of slope at 1 T and a weak peak at $T = 0.4$ K. This peak has been interpreted as an onset of slow, persistent spin fluctuations, which could be measured with zero–field muon spectroscopy (μSR) and a.c. susceptibility [127] and suggests a crossover from a spin liquid phase into another phase at finite field

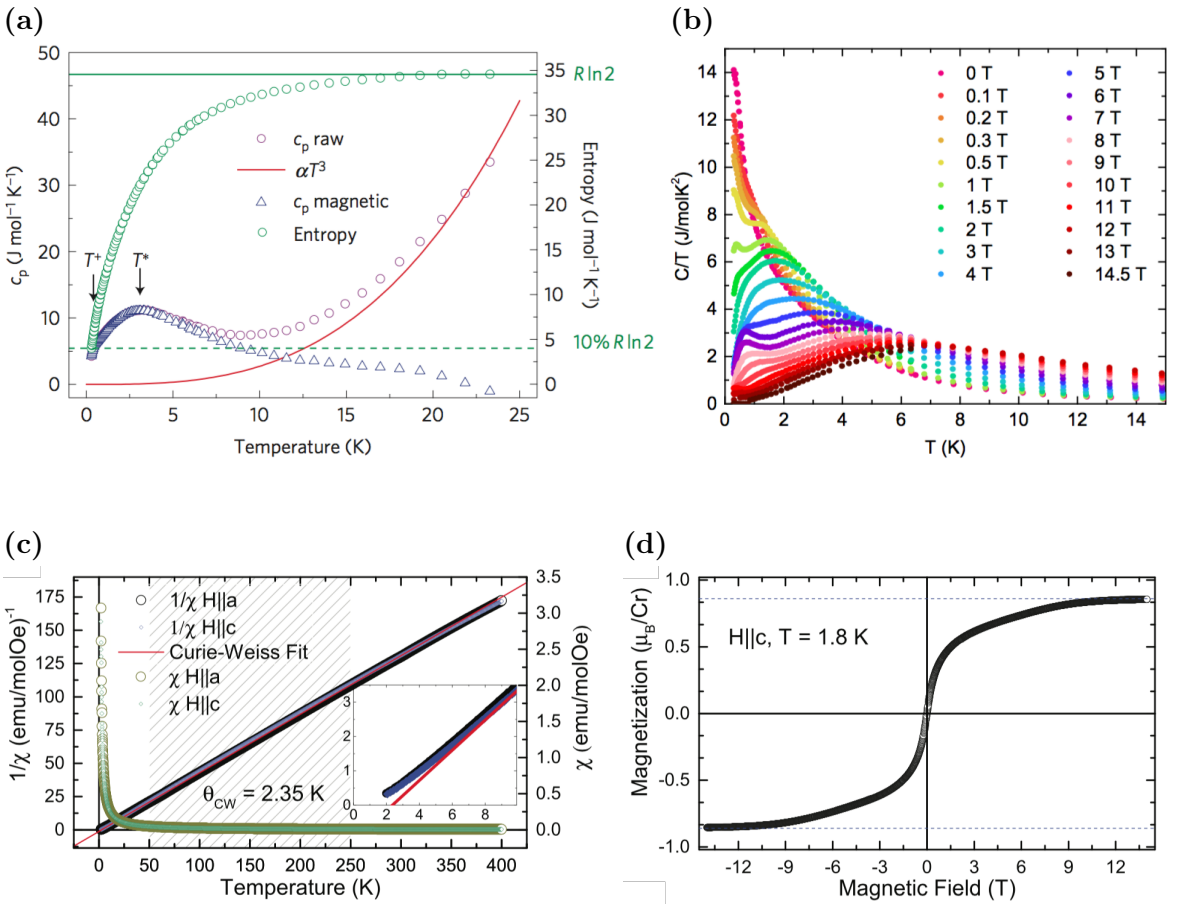

Figure 5.1: Thermodynamic properties of $Ca_{10}Cr_7O_{28}$, reproduced from [127, 249, 250]. (a) Low–temperature heat capacity with $C_p = \alpha T^3$ Debye–like phonon contribution (purple circles), and without (blue triangles). C_p for the magnetic contributions shows a broad maximum at $T^* = 3.1$ K, indicating the onset of short–range fluctuations, followed by a weak kink at $T^+ = 0.46$ K. The entropy $S = \int (C_p/T) dT$ for the magnetic contributions (green circles) has been integrated from 0.3 to 23.3 K and is plotted on the right axis. Maximum available entropy of $R \ln 2$ has been assigned to decorrelated $S = 1/2$ moments from the Cr^{5+} moments at high temperature. (b) Magnetic heat capacity C/T as a function of temperature for a range of magnetic fields. At low temperatures C/T changes slope at ~ 1 T. (c) Susceptibility (right axis) and inverse susceptibility (left axis) measured from 1.8–400 K for B = 0.1 T perpendicular and parallel to the crystallographic c axis. Inset: Curie–Weiss fit for $1/\chi$ yields $\theta_{cw} = 2.35$ K suggesting dominant ferromagnetic interactions in the material. (d) Magnetisation per Cr ion for the field applied along the crystallographic c direction at 1.8 K.

[249].

Magnetic susceptibility measurements, as reproduced from [250] and shown in Fig. 5.1(c), has been performed over a large range of temperatures in $B = 0.1$ T perpendicular and parallel to the crystallographic c axis. The linear Curie-Weiss fit for $1/\chi$ [Eq. (3.5)] reveals a Curie-temperature $\theta_{\mathrm{cw}} = 2.35$ K, suggesting dominating ferromagnetic interactions in the material, but no magnetic order down to 0.3 K.

Even though these thermodynamic properties show no magnetic order down to 0.3 K, the true ground state properties of $Ca_{10}Cr_7O_{28}$ are still unclear. To analyse the ground state properties at very low temperatures, results for the a.c. susceptibility have been carried out and could confirm that $Ca_{10}Cr_7O_{28}$ does not show any spin glass behaviour down to 0.05 K [127]. Further more, muon spin relaxation (μSR) measurements, could rule out the presence of any kind of static long–range magnetic order down to 19 mK, highly suggesting the nature of the magnetic ground state to be entirely dynamic [127].

Fig. 5.1(d), reproduced from [250] shows the magnetisation as a function of external field at 1.8 K. The magnetisation is characterised by a rapid increase up to 1T and a further increase with different slope up to saturation at around 11 T. The magnetisation is normalised to the total number of Cr ions in the lattice and shows at the saturation of $|B| \approx 12$ T a value of $6/7\mu_B = 0.857\mu_B$, since non–magnetic Cr^{6+} ions do not contribute.

5.3 The bilayer breathing kagome (BBK) model

Knowing the lattice structure for $Ca_{10}Cr_7O_{28}$ [Fig. 5.2(a)] allows to specify the model Hamiltonian, which describes magnetic properties in the material. The appropriate Hamiltonian suggested in the literature [127] considers only nearest–neighbour interactions and takes the form of a Heisenberg model

$$\mathcal{H}_{\mathsf{BBK}} = \sum_{\langle ij \rangle} J_{ij}\ \mathbf{S}_i \cdot \mathbf{S}_j - B \sum_i S_i^z\ , \tag{5.1}$$

where $\mathbf{S}_i$ are spin vector operators and J_{ij} the exchange couplings between the spins.

Fig. 5.2(b) shows the seven inequivalent nearest–neighbour interactions for the BBK model, identified from fitting of linear–spin wave (LSW) theory to INS data at high magnetic field (B = 11T) [127, 249]. The spin–wave signal along the crystallographic c direction is dispersion less, providing non–measurable coupling constants ($J_{11} = J_{12} = 0$) between the kagome bilayers. Therefore interactions between the bilayers can be ignored. This simplifies the model Hamiltonian from seven to five independent coupling constants and allows to consider a two–dimensional bilayer breathing kagome (BBK) lattice, as seen in Fig. 5.2(c), in order to simulate physical quantities for $Ca_{10}Cr_7O_{28}$.

(a)

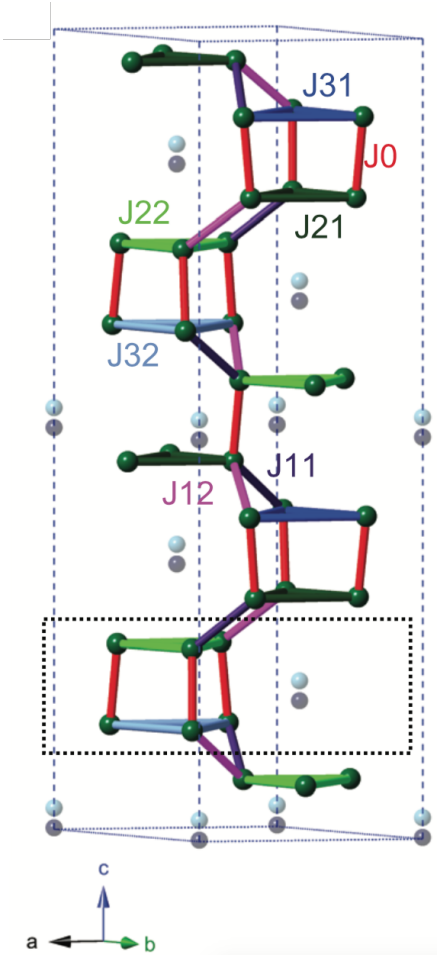

(b)

Exchange	Coupling (meV)	Type
J_0	-0.08(4)	FM
J_{11}	0	–
J_{12}	0	–
J_{21}	-0.76(5)	FM
J_{22}	-0.27(3)	FM
J_{31}	0.09(2)	AFM
J_{32}	0.11(3)	AFM

(c)

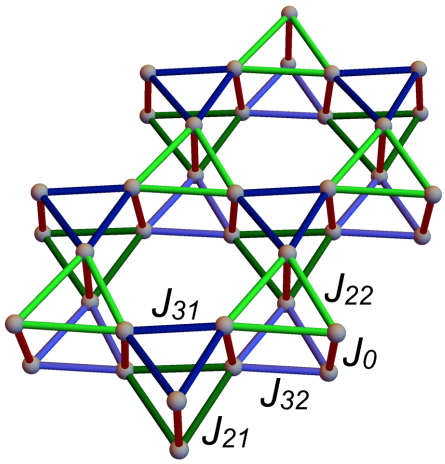

Figure 5.2: Magnetic unit cell for $Ca_{10}Cr_7O_{28}$ and simplification to the bilayer breathing kagome lattice. (a) Magnetic unit cell of $Ca_{10}Cr_7O_{28}$, reproduced from [250], revealed by x-ray and neutron diffraction consists of ABC stacked kagome bilayers of Cr^{5+} ions. Cr^{6+} ions are drawn in light and dark blue, whereas the magnetic Cr^{5+} ions are drawn in green. Magnetic Cr^{5+} ions are coupled via isotropic nearest–neighbour exchange on bonds $J_0, ..., J_{31}$. (b) Nearest–neighbour coupling parameters of the Heisenberg model on the BBK lattice taken from [127, 249]. Negative interactions are ferromagnetic (FM), while positive interactions are antiferromagnetic (AFM). Since J_{11} and J_{12} show non–measurable values, magnetic interactions in $Ca_{10}Cr_7O_{28}$ can be considered to happen just in individual, decoupled bilayer kagome layers. (c) Single layer of the bilayer breathing kagome lattice.

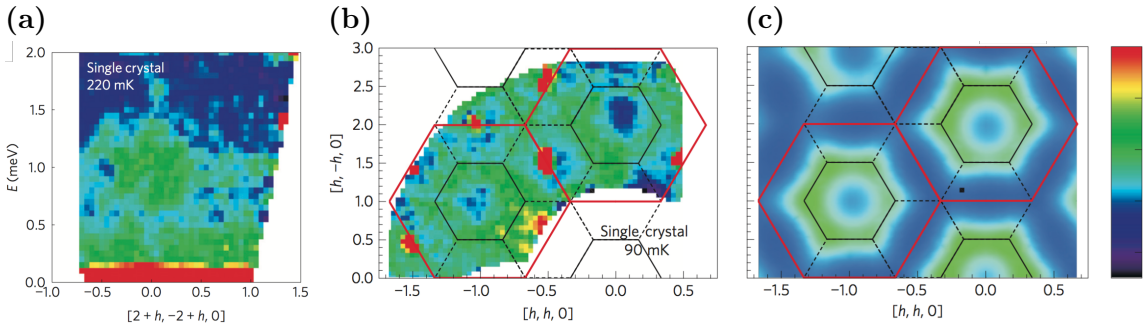

Figure 5.3: Inelastic neutron scattering data for $Ca_{10}Cr_7O_{28}$ compared to theory, reproduced from [127]. (a) Single-crystal inelastic neutron scattering (INS) data measured at zero applied field and T = 220 mK. Three energy scales appear between $0.7 - 1.3$ meV, $0.2 - 0.6$ meV and < 0.2 meV, without any signature of spin waves. No magnetic scattering has been found above 1.6 meV. (b) Energy slice of INS data from (a) at $E = 0.25$ meV and $T = 90$ mK shows broad intensities on a ring around the Brillouin centres. (c) **q**–space resolved susceptibility, calculated by a pseudofermion functional renormalisation group (PFFRG) shows no sign of order at E = 0 meV and T = 0 K. Intensities are broadly distributed around the corners of every second Brillouin, comparable to results in INS experiments (b). False colour plots present intensities with high scattering in red and low scattering in blue.

5.4 Magnetic excitations in $Ca_{10}Cr_7O_{28}$ in theory and experiment

To investigate the dynamical properties in $Ca_{10}Cr_7O_{28}$, Balz *et al.* [127] chose inelastic neutron scattering (INS) as an optimal probe for magnetic dipole excitations. Fig. 5.3(a) shows INS data on a single crystal of $Ca_{10}Cr_7O_{28}$ along the [2+h, -2+h, 0] direction (within kagome planes) in zero field, and reproduces three energy scales. Intensities are found on a high–energy scale between $0.7 - 1.3$ meV, an intermediate–energy scale between $0.2 - 0.6$ meV and a low–energy scale < 0.2 meV. Data show diffuse and dispersionless scattering, which is much broader than the instrumental resolution, and no signs of order due to the absence of magnetic Bragg peaks. The signal at low–energies comes in experiments from incoherent–quasi elastic background scattering, which, however, turns out to hide another gapless spin–wave excitation, as presented in numerical investigations in Section 5.5. Magnetic scattering above 1.6 meV has been confirmed to be absent [127].

An energy slice of the INS data in Fig. 5.3(a) at $E = 0.25$ meV and $T = 90$ is shown in Fig. 5.3(b) and contains broad intensities in the form of "ring–pattern", located around the Brillouin zone centres. Data do not show signatures of magnetic order, whereas the high–intensity peaks in red are coming from phonon excitations.

Those "rings" have also been seen by Balz *et al.* in pseudofermion functional renormalisation group (PFFRG) calculations [Fig. 5.3(c), reproduced from [127]], which measures the momentum–resolved susceptibility at E = 0 meV and T = 0 K.

Investigations with molecular dynamics simulations shall provide further insights into the dynamical properties of the three energy–regimes and the connection between the "ring"–like features at low energy with the spin–liquid behaviour in $Ca_{10}Cr_7O_{28}$.

5.4.1 Details of simulations

Considering the Heisenberg model, given in Eq. (5.1), classical Monte Carlo simulations have been used to produce a thermally–equilibrated canonical ensemble of classical vectors on the bilayer breathing kagome (BBK) lattice. Those vectors are normalised to $S = 1/2$ and shall represent spins of Cr^{5+} ions in $Ca_{10}Cr_7O_{28}$. In order to achieve satisfying statistics various Monte Carlo algorithms, such as the heat bath method, over relaxation and parallel tempering (all explained in Section 2.2) have been used.

Numerical integration of the semi–classical equations of motion (Section 2.3) has been carried out using the Runge–Kutta method of order 4 [Eq. (2.99)], followed by a Fourier transform of the time and space–dependent spin–spin correlation into energy and momentum space. Following the discussion in Section 2.4 the spin signal in time has been multiplied by a Gaussian, such that the Fourier transformed signal resolved a Gaussian convolution in energy–space. For satisfying comparison to experiments this signal has been evaluated for Eq. (2.100), by choosing a Gaussian envelope of FWHM = 0.2 meV, and the magnetic form–factor for the Cr^{5+} ions, as presented in Appendix D.1.

5.4.2 Polarised state at high field

The absence of order in $Ca_{10}Cr_7O_{28}$ below 90 mK is consistent with the absence of distinct spin–wave branches in inelastic neutron scattering (INS) experiments [Fig. 5.3(a)]. In order to confirm the validity of the semiclassical molecular–dynamics (MD) method and the quality of simulation results, a direct comparison to the fully polarised state in high magnetic field is a sensible task to do. Hereby, the quantum fluctuations will be suppressed and allow for spin–waves on top of the fully polarised state, which should provide comparable results between INS, MD and also linear spin–wave (LSW) theory.

Fig. 5.4 shows the direct comparison between INS results for $Ca_{10}Cr_7O_{28}$, reproduced from [127], and the dynamical structure factor, theoretically obtained from MD simulations and LSW theory (Appendix B.2) of the BBK model [Eq. (5.1)] at B = 11 T. Such fields have been chosen, since the magnetisation is fully saturated at B = 11 T and above, as seen in Fig. 5.1(d).

The spin–wave spectrum of $Ca_{10}Cr_7O_{28}$ and the BBK model show three distinct spin–wave branches at finite energy, visible with significant high–intensity regions at Brillouin zone centres. Two branches at high energy look quantitatively the same, however with different intensity distributions between each other. Recovering a reasonable good spin–wave dispersion is a good indication for the reliability of results from MD simulations.

LSW theory works very well for predicting excitations about the saturated state in applied magnetic field, albeit does not work well for predicting dynamical properties of a disordered state in absence or at low fields. The strength of finite temperature MD simulations is its predictive power even for non–polarised states at low magnetic fields,

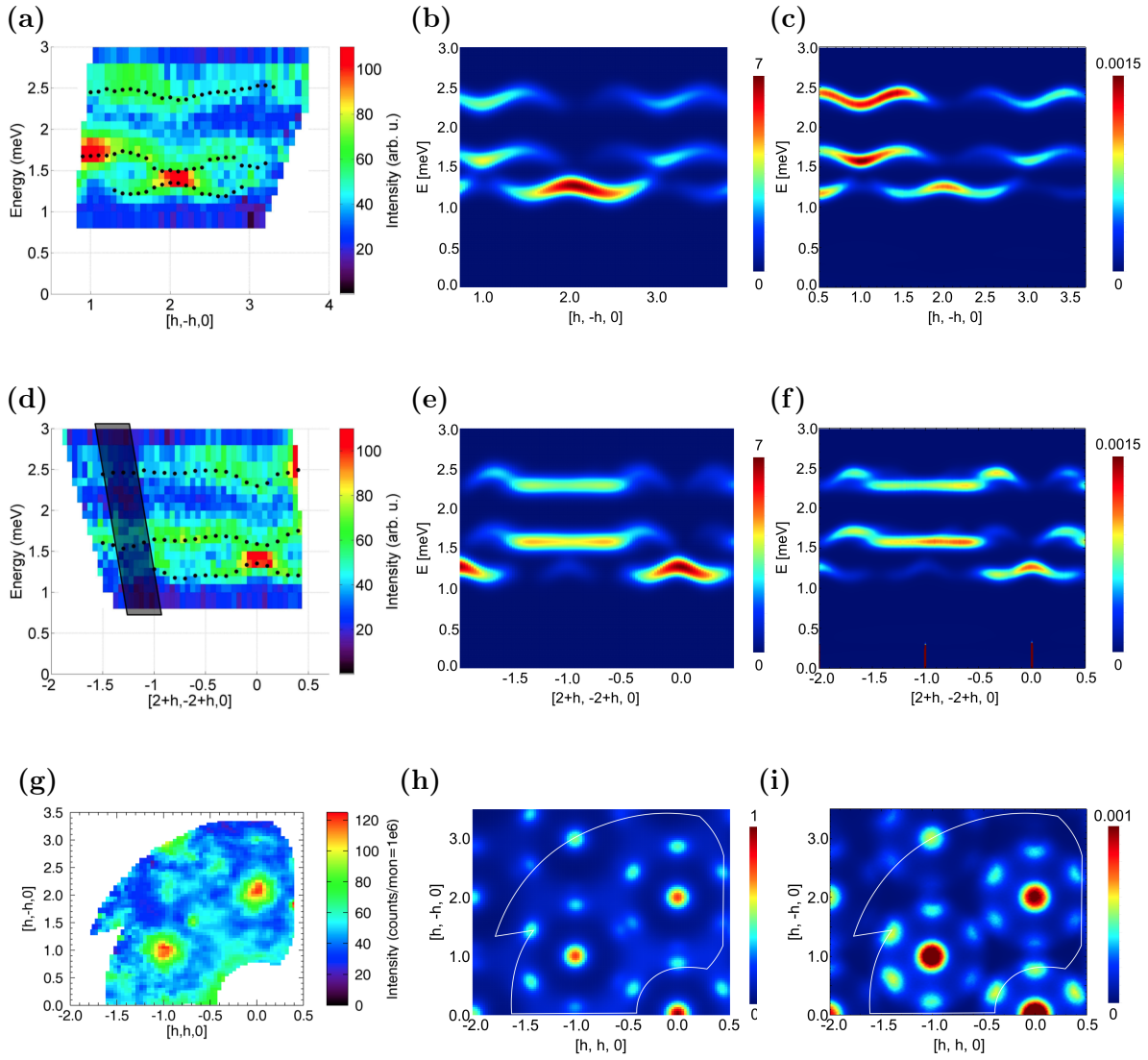

Figure 5.4: Spin dynamics of $Ca_{10}Cr_7O_{28}$ in the saturated state at B = 11 T. (a), (d), (g) Results for inelastic neutron scattering (INS) experiments, reproduced from [127, 249], are compared to (b), (e), (h) linear spin–wave (LSW) theory and (c), (f), (i) molecular dynamics (MD) results of the bilayer breathing Kagome (BBK) model $\mathcal{H}_{\mathrm{BBK}}$ [Eq. (5.1)], with parameters taken from Fig. 5.2(b). (a)–(c) Gapped, dispersing spin–wave excitations along the [h, -h, 0] direction. (d)–(f) Gapped, dispersing spin–wave excitations along the [2+h, -2 + h, 0] direction. Constant–energy cut at (g) E = 1.4 meV, and (h) and (i) E = 1.3 meV shows bright features corresponding to high intensities in the spin–wave dispersion. In order to compare to INS data, results for LSW theory and MD simulations are presented with a Gaussian convolution of FWHM = 0.2 meV. INS and MD results at $T = 90$mK, while LSW theory at T = 0.

since it is not limited to the underlying order of the system. The following section shall evaluate the evolution of the dynamical structure factor in field, and shall suggest the range of fields, where MD simulations can be expected to be reliable.

5.4.3 Evolution of the spin–wave spectrum in field

Starting from the polarised state at B = 11T, where experiments and simulations compare reasonably well, the field can be reduced in order to "trace" the behaviour of the spin–wave branches down to the point at which the excitation–gap closes. Fig. 5.5 compares the INS data for $Ca_{10}Cr_7O_{28}$, reproduced from [127], with the $S(\mathbf{q}, \omega)$ from molecular–dynamics simulations of the BBK model. Even though $Ca_{10}Cr_7O_{28}$ already leaves its fully polarised state for $B < 11$ T [Fig. 5.1(d)], a comparison between theory and experiment provides reasonable results down to $B \approx 1$ T. At such fields the lowest band touches zero energy, as shown in a later section in Fig. 5.12 and compares to a systematic change of the heat capacity, seen in Fig. 5.1(b).

At B = 0 T, a clear comparison to experiment becomes difficult, since INS data shows strong diffusive scattering in the background, which is absent in MD simulations. However, experiment and theory still show three energy–scales, which can be analysed in more detail.

5.4.4 Dynamics at zero field

The comparison of energy slices at zero field for each energy regime is presented in Fig. 5.6. The low energy signal in Fig. 5.6(e) and Fig. 5.6(f) shows "rings" in momentum space, with intensity around the corners of every second Brillouin zone. Actually, this scattering pattern stays the same for even lower energies, just increases in intensity, and is remarkably similar to pseudofermion functional renormalisation (PFFRG) [127], at E=0 meV and T=0 K [Fig. 5.3(c)]. It turns out, that the origin of those ring–like diffuse scattering signatures is originated in the coexistence of spiral ground–states with different ordering vector in momentum space. A detailed discussion is given in Section 5.5.1.

Signal at finite energies Fig. 5.6(a), (b) and (c), (d) shows broadened, "bow–tie" like features, as seen in e.g. in the Heisenberg antiferromagnet on the kagome lattice [Fig. 1.6 in Section 1.3.2] and shall be considered in more detail in Section 5.5.2.

5.5 Origin of spin liquid behaviour in the BBK model and $Ca_{10}Cr_7O_{28}$

5.5.1 Mapping onto the J_1-J_2 Honeycomb model

Dynamical correlations of $Ca_{10}Cr_7O_{28}$ show "ring features" in INS data [Fig. 5.6(e)], and MD simulations on the BBK model [Fig. 5.6(f)]. The Hamiltonian in Eq. (5.1) defined on the BBK lattice [Fig. 5.2(c)] includes five independent coupling parameters [Fig. 5.2(b)], which makes a deep understanding of the ground state properties rather

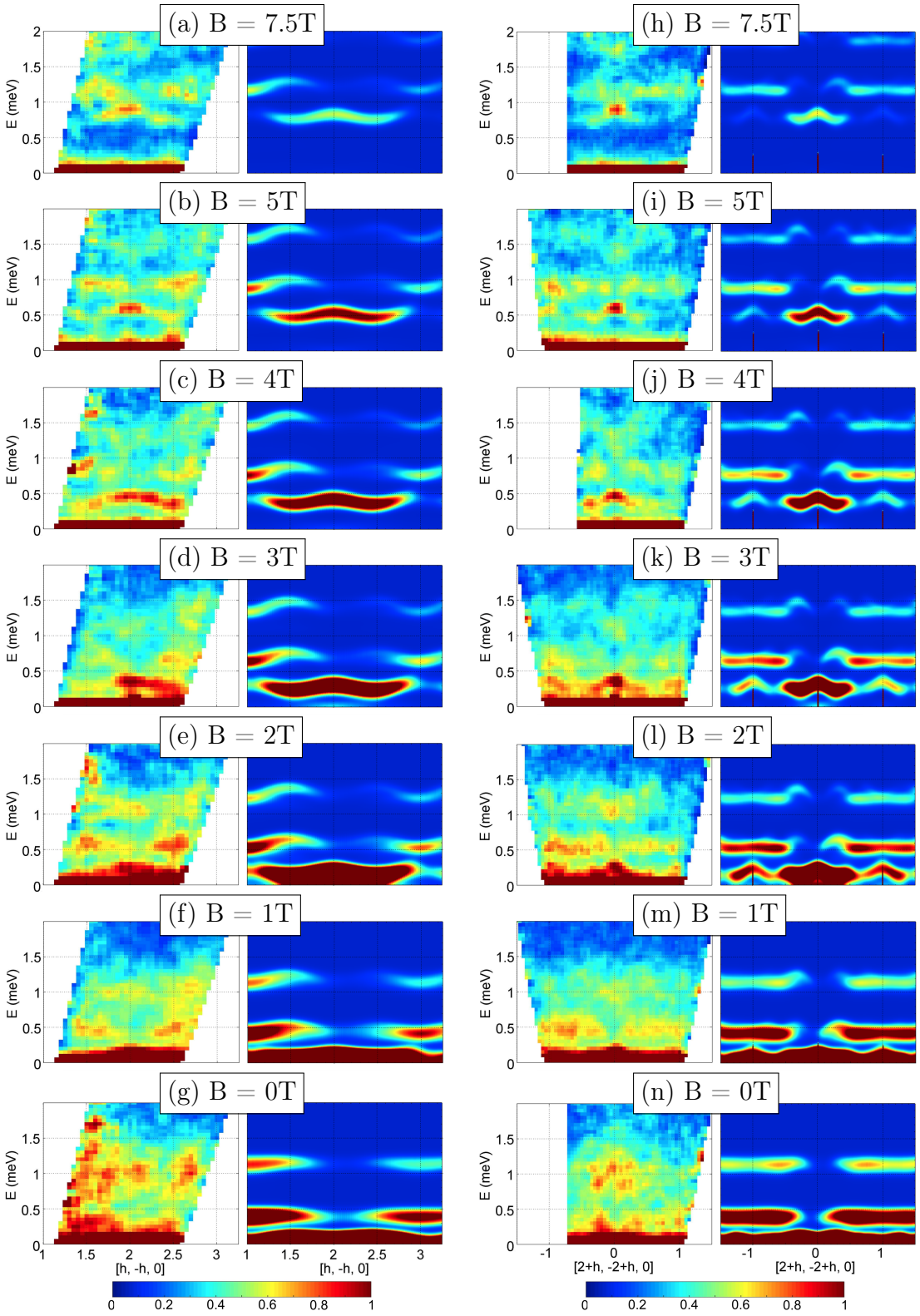

Figure 5.5: Evolution of spin excitations as a function of magnetic field. Comparison between inelastic neutron scattering results for $Ca_{10}Cr_7O_{28}$, reproduced from [249], and the dynamical structure factor $S(\mathbf{q}, \omega)$ from molecular dynamics (MD) simulations of the bilayer breathing kagome model [Eq. (5.1)]. Results are shown along the $[h, -h, 0]$ and $[2+h, -2+h, 0]$ direction, both integrated over ± 0.2 r.l.u. perpendicular to the cut in reciprocal space. MD simulations have been convoluted with a Gaussian of FWHM = 0.2 meV.

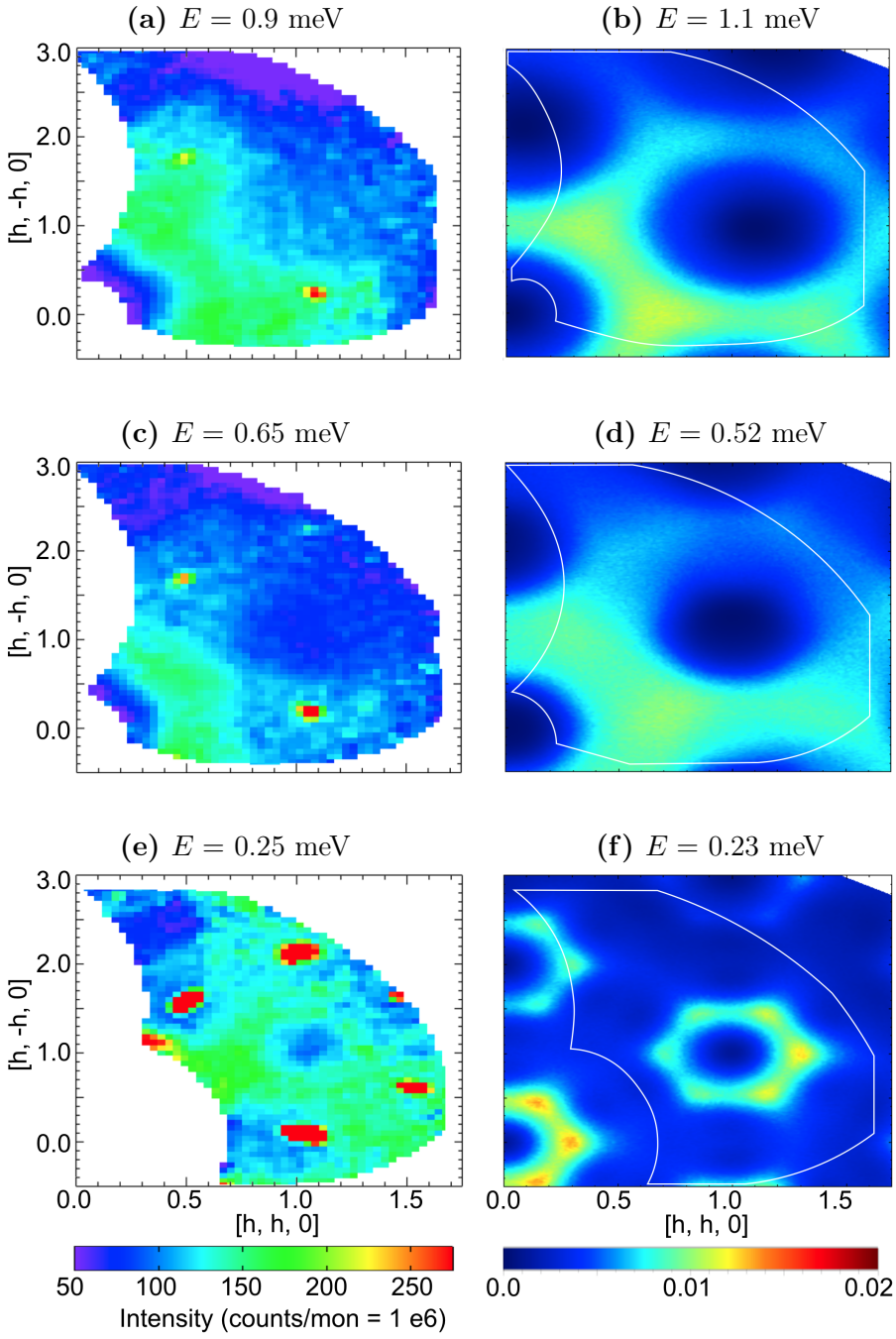

Figure 5.6: Dynamical correlations in the spin–liquid phase of $Ca_{10}Cr_7O_{28}$. (b), (c), (e) Constant–energy cuts through inelastic neutron scattering data for $Ca_{10}Cr_7O_{28}$ in zero magnetic field, reproduced from [254]. (a), (d), (f) Constant–energy cuts through the dynamical structure factor $S(\mathbf{q}, \omega)$ [Eq. (2.101)], calculated via molecular dynamics (MD) simulations of of the bilayer breathing Kagome (BBK) model $\mathcal{H}_{\text{BBK}}$ [Eq. (5.1)]. Scattering at low energies ($E \approx 0 - 0.3$ meV) shows a ring–like pattern, characteristic of the spin–liquid ground state. Scattering at higher energies show broadened, bow–tie features, of the type associated with the spin liquid in the Kagome-lattice antiferromagnet [see Fig. 5.11 and Fig. 5.10] For comparison with experiment, MD results have been convoluted in energy with a Gaussian of FWHM = 0.2 meV.

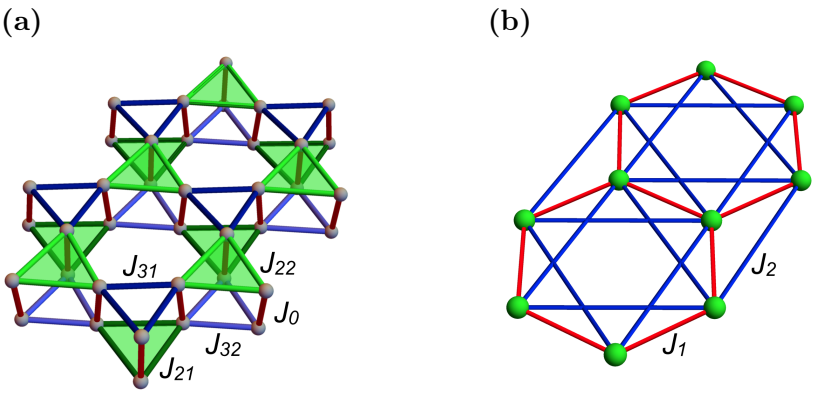

Figure 5.7: Mapping onto an effective J_1-J_2 Honeycomb model. (a) Ferromagnetic couplings on alternating triangles are dominant (shaded in green). (b) Assuming the limit of infinite strong ferromagnetic couplings (J_{21} and J_{22}) allows to contract three $S = 1/2$ sites from the triangular plaquettes onto one singular $S = 3/2$ site. The problem maps onto an effective $S = 3/2$ J_1-J_2 Heisenberg model on the Honeycomb lattice [Eq. (5.2)].

complicated. However, further simplifications of the model Hamiltonian are possible, in order to qualitatively understand the scattering pattern.

Coupling constants of the BBK model Fig. 5.2(b) provide predominantly ferromagnetic (FM) exchange interactions, also shown from a Curie-Weiss fit revealing a positive Curie-temperature $\theta_{cw} = 2.35$ K [Fig. 5.1(c)]. The dominant exchange interaction on the ferromagnetic bonds [J_{21} and J_{22} shaded as green triangles in Fig. 5.7(a)], suggests to consider their infinitely large limit. Single triangular plaquettes with ferromagnetic interactions and three spins $S = 1/2$ can be contracted to a single site with $S = 3/2$, as depicted in Fig. 5.7(b). The effective model forms a $S = 3/2$, J_1-J_2 Heisenberg model on the honeycomb lattice

$$\mathcal{H}_{\mathsf{HC}} = J_1 \sum_{\langle ij \rangle_1} \mathbf{S}_i \cdot \mathbf{S}_j + J_2 \sum_{\langle ij \rangle_2} \mathbf{S}_i \cdot \mathbf{S}_j \ , \tag{5.2}$$

where the nearly identical antiferromagnetic couplings J_{31} and J_{32} and the ferromagnetic interlayer coupling J_0 from the BBK model transform respectively into the antiferromagnetic next–nearest neighbour coupling J_2 and into the nearest–neighbour coupling J_1 of the honeycomb model.

The classical ground states of this model has been studied already in the past [126, 120] and shows various spiral ground states at zero temperature, as introduced in Section 1.3.3. In a specific region of the phase diagram, there exist a set of coexisting spiral ground states with different ordering vectors, distributed on a ring in momentum space. Fouet *et al.* conjectured that the models on this coexistence line have a RVB spin–liquid ground–state, with a small but finite gap and strong short range order [120].

Fig. 5.8(a) shows the zero–field phase diagram for the BBK model [Eq. (5.1)], as determined from the maxima in specific heat, obtained in classical Monte Carlo simulations. Simulations were carried out for parameter sets appropriate for $Ca_{10}Cr_7O_{28}$,

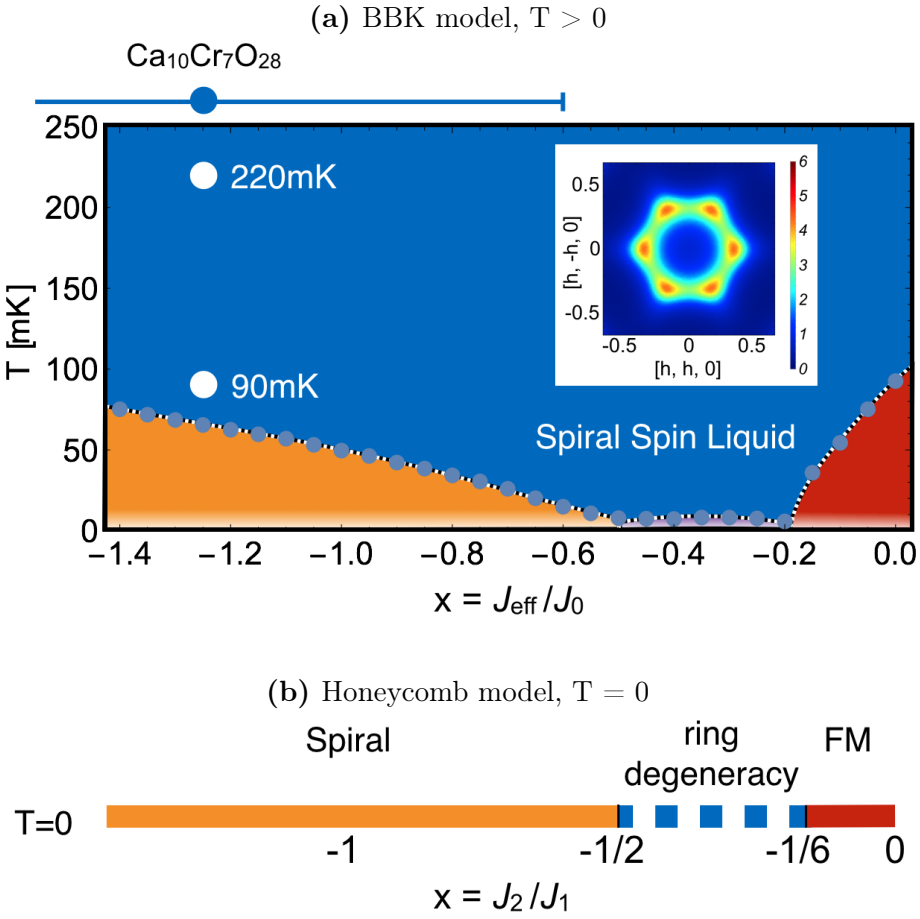

Figure 5.8: Phase diagram of the bilayer breathing kagome (BBK) and J_1-J_2 Honeycomb model. (a) Finite–temperature phase diagram of the BBK model, Eq. (5.1), as determined by classical Monte Carlo simulation, allowing $J_{\text{eff}} \equiv J_{31} = J_{32}$ to vary, with all other parameters taken from $Ca_{10}Cr_7O_{28}$. Dotted lines correspond to peaks in the specific heat $C(T)$, and indicate the onset of correlations corresponding to spiral/ferromagnetic states at low temperature. White spots show the parameter–ratio and temperatures associated with inelastic neutron–scattering experiments on $Ca_{10}Cr_7O_{28}$ [127, 249]. **Inset:** "ring" in equal–time structure factor $S(\mathbf{q})$, characteristic of the spiral spin liquid. Monte Carlo simulations have been performed for a system with $N = 13824$ sites. (b) Classical ground state of the effective honeycomb–lattice model, Eq. (5.2), following [126, 120]. The spiral spin liquid can be traced to a highly–degenerate manifold of classical ground states occurring for $-1/2 < x < -1/6$.

where the value of antiferromagnetic couplings $J_{\text{eff}} \equiv J_{31} = J_{32}$ has been been varied as $x = J_{\text{eff}}/J_0$. The low–temperature regime of the phase diagram shows spiral and ferromagnetic states, with a broad region of a spiral spin liquid at higher temperatures, providing a "ring" feature in the equal time structure factor $S(\mathbf{q})$ [see inset Fig. 5.8(a)]. The $S(\mathbf{q})$ has been calculated at (T = 222 mK), in the vicinity of a zero–temperature ordered spiral ground state and therefore shows the emergence of Bragg peaks at high–symmetry points of the Brillouin zone. Taking the parameter set from Fig. 5.2(b), $Ca_{10}Cr_7O_{28}$ can be found at $x = -1.25$ in this phase diagram. However, the error bars in this estimation of coupling parameters is quite large, allowing the material to exist in a large region of parameter space up to $x \leq -0.6$. Fig. 5.8(b) Classical zero–temperature ground state phase diagram for the J_1-J_2-J_3 Heisenberg model on the Honeycomb lattice [Eq. (5.2)], as reproduced from [126, 120], for $J_1 < 0$ and $J_3 = 0$. The spiral spin liquid can be traced to a highly–degenerate manifold of classical ground states occurring for $-1/2 < x < -1/6$.

5.5.2 Transverse and longitudinal excitations

Fig. 5.5 shows the field dependent evolution of spin–wave excitations from MD simulations and INS data. A broad energy–convolution in MD simulations makes a comparison to experiments possible, but a physical understanding of dynamical properties rather complicated. Fig. 5.9 shows MD simulations of $\mathcal{H}_{\text{BBK}}$ [Eq. (5.1)] with better resolution in energy–space than provided by experiment.

Additionally the dynamical structure factor $S(\mathbf{q}, \omega)$ has been separated into transverse and longitudinal channel, where

$$S(\mathbf{q}, \omega) = S^{\perp}(\mathbf{q}, \omega) + S^{\parallel}(\mathbf{q}, \omega) \; . \tag{5.3}$$

These quantities are defined by

$$S^{\perp}(\mathbf{q}, \omega) \;=\; \frac{1}{\sqrt{N_t}} \sum_{n}^{N_t} \mathrm{e}^{\mathrm{i}\omega \; n\delta t} \, \langle \mathbf{S}^{\perp}_{\mathbf{q}}(t) \cdot \mathbf{S}^{\perp}_{-\mathbf{q}}(0) \rangle \; , \qquad \mathbf{S}^{\perp}_i = (S^x_i, S^y_i) \; , \tag{5.4}$$

and

$$S^{\parallel}(\mathbf{q}, \omega) \;=\; \frac{1}{\sqrt{N_t}} \sum_{n}^{N_t} \mathrm{e}^{\mathrm{i}\omega \; n\delta t} \, \langle S^z_{\mathbf{q}}(t) \cdot S^z_{-\mathbf{q}}(0) \rangle \; . \tag{5.5}$$

The channel perpendicular to the external field $S^{\perp}(\mathbf{q}, \omega)$ will account for transverse spin excitations (x, y components of the spins) and represents usually the types of excitations accessible in linear spin–wave (LSW) theory.

$S^{\perp}(\mathbf{q}, \omega)$ shows six pair–wise degenerate spin–wave branches persistent for a wide range of magnetic fields. By decreasing the external field, those spin–wave branches gain intensity and shift down in energy. In fact, above $B \gtrsim 1$ T the energy for all bands depends linearly on the field, as shown in Section 5.5.3.

More surprisingly, dynamical properties of $\mathcal{H}_{\text{BBK}}$ [Eq. (5.1)] also include gapless longitudinal excitations. As seen in the longitudinal channel $S^{\parallel}(\mathbf{q}, \omega)$ of Fig. 5.9, the intensity dominates the Brillouin zone centre in form of Bragg peaks, corresponding to

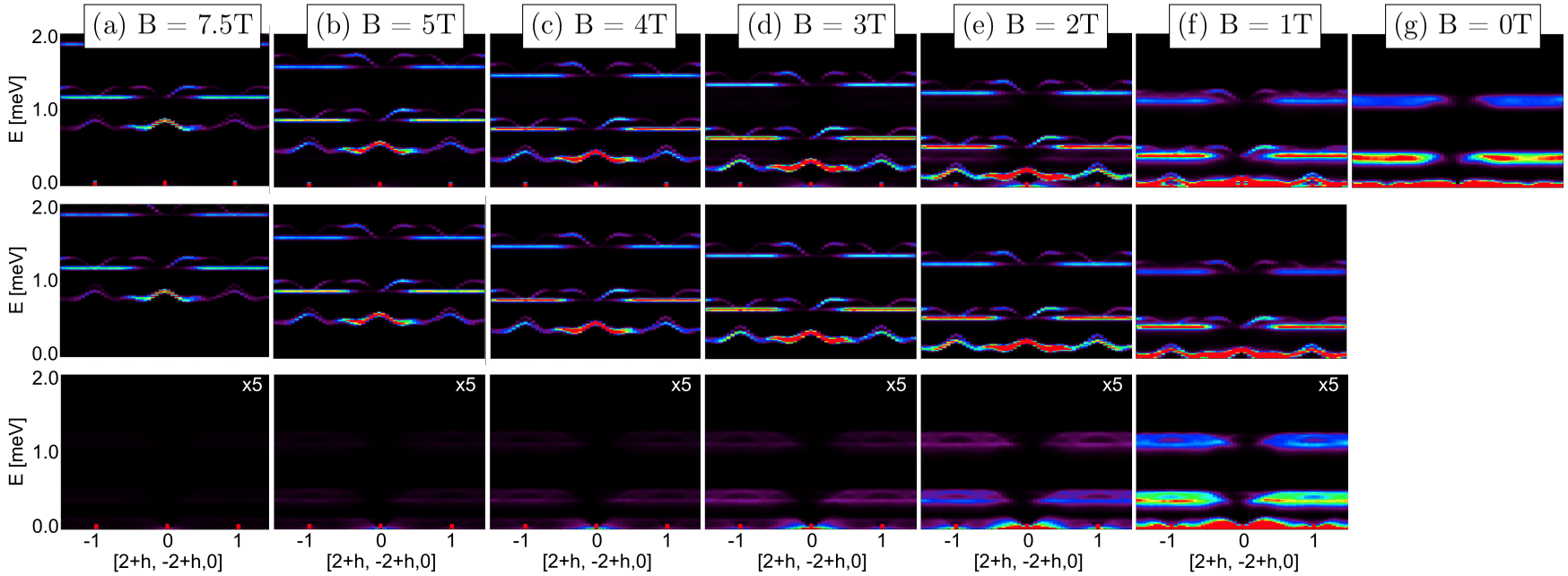

Figure 5.9: Evolution of the spin–wave spectrum for the bilayer breathing kagome model in field. *First row:* Comparable to Fig. 5.5, shows the total dynamical structure factor $S(\omega, \mathbf{q})$ [Eq. (5.3)] with maximally possible resolution in energy and momentum space. *Second row:* transverse structure factor $S^{\perp}(\omega, \mathbf{q})$ [Eq. (5.4)], *Third row:* longitudinal structure factor $S^{\parallel}(\omega, \mathbf{q})$ [Eq. (5.5)]. While transverse spin–excitations increase linearly in energy as a function of field, the longitudinal spin excitations do not. Decreasing magnetic field will increase the longitudinal signal, and lower the energy for the transverse signal. For low enough fields both transverse and longitudinal spin–excitations coexist at the same energy. The magnetic form factor for Cr^{5+} ions has not been included, system temperature is $T = 222$ mK.

the field induced polarisation of the spins. In addition, three bands of diffuse weekly–dispersing longitudinal excitations are visible for fields below 4T. Those bands stay constant in energy and therefore suggest excitations of multiple spins, with total spin S=0, which do not couple to an external magnetic field. The lowest band is tight to zero energy and becomes nearly flat at 1T, when the band–gap in the transverse channel closes.

Transverse excitations

Fig. 5.10(a) shows transverse spin–wave branches in $S^{\perp}(\mathbf{q},\omega)$ at T = 222 mK and B=2 T. Energy slices along the low–energy band shows "ring" features [Fig. 5.10(g)], a signature of the spin–liquid ground state of the BBK model, understandable by a mapping to the further–neighbour Heisenberg model on the honeycomb lattice (details are discussed in Section 5.5.1).

Intermediate and high energy bands in $S^{\perp}(\mathbf{q},\omega)$ show quantitatively the same spin–wave branches. Those branches are considered to correspond to dynamics within each breathing–kagome layer, but happen at different energy scales and different intensity, since ferromagnetic couplings within the layers [Table of Fig. 5.2(b)] are different. Energy slices along the flat mode at $S^{\perp}(\mathbf{q},\omega = 0.54$ meV) in Fig. 5.10(e) show bow–tie features of strong scattering intensity which are connected via pinch–points, located at the Brillouin–zone centres. Those features are comparable to dynamical properties in the cooperative paramagnetic regime of the classical antiferromagnetic Heisenberg model on the kagome lattice [Fig. 1.6(c) in Section 1.3.2] and suggest a spin liquid ground state with emergent Coulomb gauge structure. Hereby, additional features, which would correspond to the development of $\sqrt{3} \times \sqrt{3}$ coplanar order [compare to Fig. 1.6(b) and Fig. 1.7(a)] have not be seen at the considered temperature.

Energy slices at slightly higher energy [Fig. 5.10(c)], compared to the flat band reveal structure in the form of "half moons", corresponding to the development of spin–wave branches out of the flat band, as seen in Fig. 1.7(b) in Section 1.3.2 for the the antiferromagnetic Heisenberg model on the kagome lattice.

Longitudinal excitations

Fig. 5.10(b) shows diffuse weakly–dispersing longitudinal bands in $S^{\parallel}(\omega,\mathbf{q})$ at B=2 T and T = 222 mK. The lowest band is tight to zero energy and shows, next to Bragg peaks at the Brillouin zone centres, also intensity, which is circularly distributed around every second Brillouin zone centre [Fig. 5.10(h)].

Energy slices along the flat mode at $S^{\perp}(\mathbf{q},\omega = 0.39$meV) in Fig. 5.10(f) show a broad and weak distribution of intensity with zero weight in a small circular region around every second Brillouin centre. Those longitudinal excitations cause a broadening of the pinch–point features in the transverse channel, as shown for lower fields in Fig. 5.11. Energy slices at slightly higher energy [Fig. 5.10(d)], show broad intensity distributions similar to the shape of a honeycomb lattice.

The origin of those longitudinal modes has not been clarified yet, but suggest important physical insights for a qualitative interpretation of the broadening of bow–tie features seen in INS data [Fig. 5.6(a) and Fig. 5.6(b)].

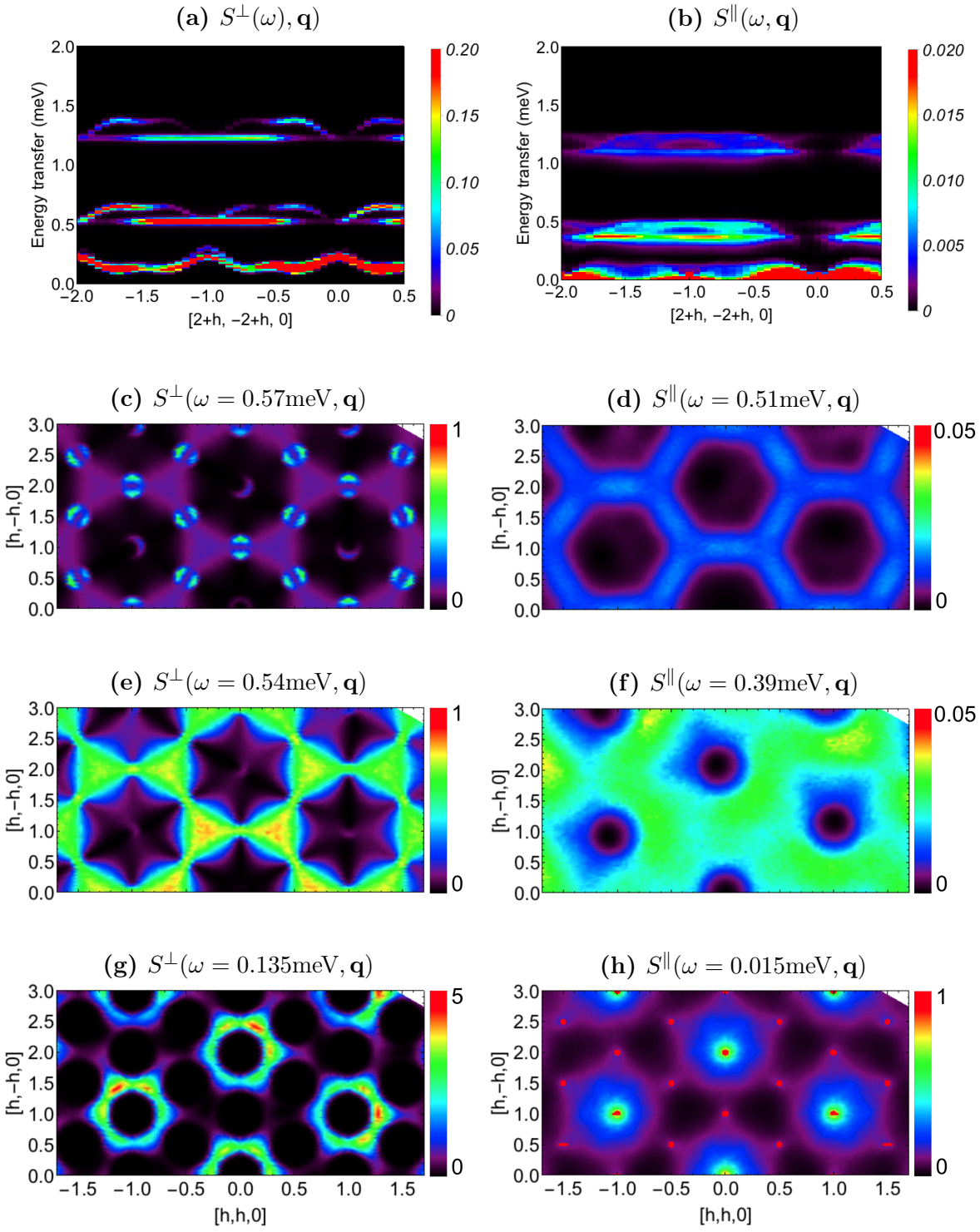

Figure 5.10: Spin dynamics in field show transverse and longitudinal excitations. (a) Simulation results for $S^{\perp}(\omega, \mathbf{q})$ [Eq. (5.4)] at B = 2T and T = 222 mK, show six distinct branches of transverse spin–wave excitations. Constant energy–line cuts can be seen in (c), (e) and (g). (b) Simulation results for $S^{\parallel}(\omega, \mathbf{q})$ [Eq. (5.5)], showing gapless, longitudinal spin excitations with weak signal. The magnetic form factor for Cr^{5+} ions has not been included.

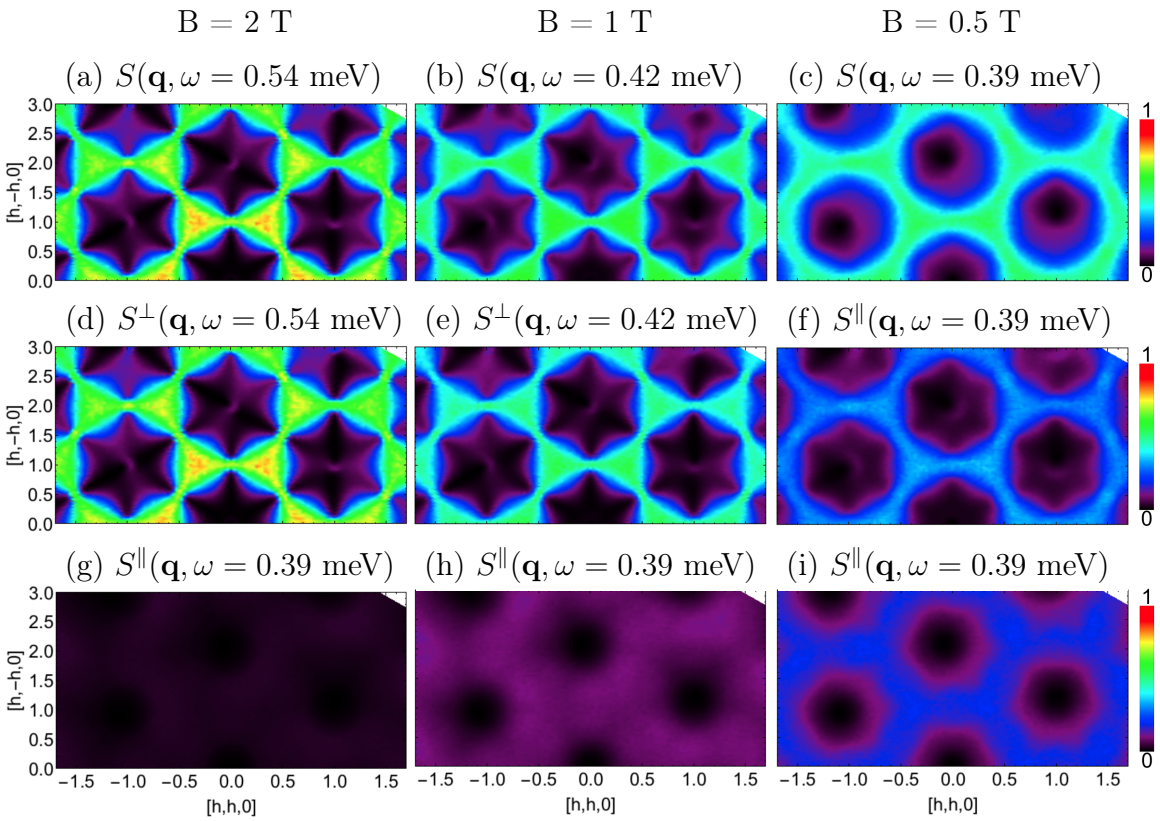

Figure 5.11: Field dependency of transverse and longitudinal spin–excitations at high–energy. Transverse and longitudinal spin excitations separate for fields $B \geq 1$ T and show at line cuts along the flat band in Fig. 5.10(a) pinch–points, comparable to those in the classical antiferromagnetic Heisenberg model on the kagome lattice [90, 115]. Decreasing magnetic field will increase the longitudinal signal, and lower the energy for the transverse signal. For low enough fields both spin excitations coexist at the same energy, which causes the broadening of pinch–points seen as in (c), comparable to experimental INS data in Fig. 5.6(a).

Broadening of pinch-points

The evolution of the pinch–points down to low magnetic fields is shown in Fig. 5.11. A decreasing magnetic field will increase the intensity signal of the longitudinal spin excitations, while lowering the energy for the transverse excitations. For low enough fields both spin excitations coexist at the same energy, which causes the broadening of pinch–points seen as in Fig. 5.11(c). These signatures are comparable to experimental INS data, as presented in Fig. 5.6(c) and Fig. 5.6(a).

5.5.3 Band–gap opening at $B = 1$ T

Analysing results obtained by MD simulations, as presented in Fig. 5.9 for dynamics in the transverse channel [Eq. (5.4)] allows to make qualitative statements about the closing of the lowest–lying band–gap in the model. Fig. 5.12 shows the minimal energy Δ of the lowest lying band as a function of applied field B, determined by MD simu-

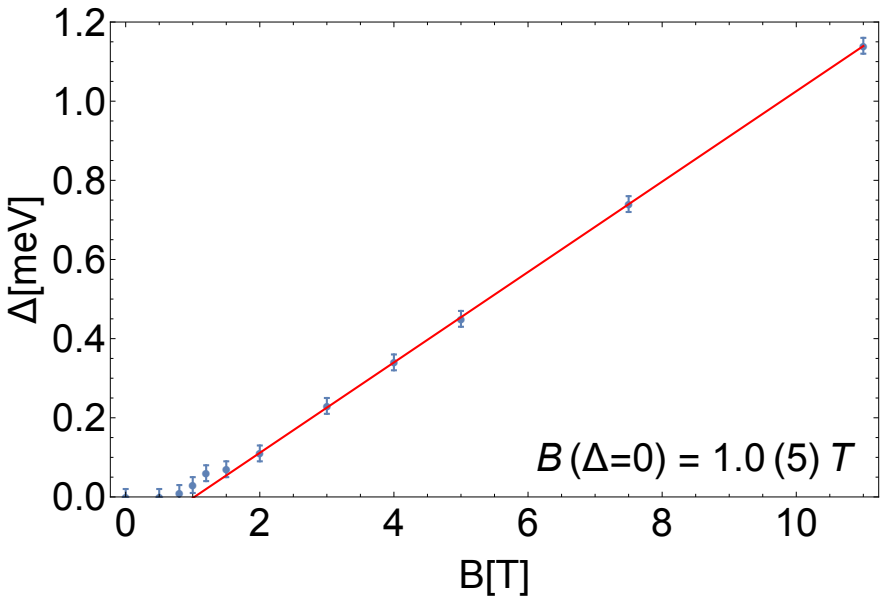

Figure 5.12: Gap to transverse spin excitations as a function of applied magnetic field. Estimation of the field–dependent energy–minimum of the lowest band in the transverse channel $S^{\perp}(\omega, \mathbf{q})$ [Eq. (5.4)], obtained from molecular dynamics simulations of $\mathcal{H}_{\text{BBK}}$ [Eq. (5.1)] for parameters of $Ca_{10}Cr_7O_{28}$. Linear fit at high fields provides the estimate of a bandgap touching at $B = 1.0(5)$ T, which is consistent with a systematic change of the heat–capacity measurements at 1 T in $Ca_{10}Cr_7O_{28}$ [Fig. 5.1(b)].

lations. A linear interpolation of Δ at high fields shows, that the lowest band touches zero energy $B \approx 1$ T. This result is consistent with experimental measurements of the specific heat as a function of field, presented in [249].

5.5.4 Spin–liquid scenario in $Ca_{10}Cr_7O_{28}$

$Ca_{10}Cr_7O_{28}$ provides a new example of a gapless, two–dimensional spin liquid. The lowest band shows "ring" features, seen and compared between inelastic neutron scattering experiments for $Ca_{10}Cr_7O_{28}$, pseudofermion functional renormalisation group calculations and molecular dynamics simulations [Fig. 5.3 and Fig. 5.6].

The origin of this signature can be understood by a mapping of the bilayer breathing kagome model onto the J_1-J_2 honeycomb model. For a specific parameter region in the phase diagram, relevant to $Ca_{10}Cr_7O_{28}$, this model allows for coexisting spiral ground states with different momentum ordering $\mathbf{q}$-vector. Highly degenerate ground states with continuously varying momentum on a ring emerge and give rise to the spin–liquid behaviour, seen in $Ca_{10}Cr_7O_{28}$. In fact, such a class of spin liquids is referred to as "spiral spin liquids" and showed already its presence, next to the J_1-J_2 Heisenberg model on the honeycomb lattice [81] also e.g. in the the J_1-J_2-J_3 model on the square lattice [82] and the J_1-J_2 model on the diamond lattice [255, 256].

The analysis of the spin–wave spectrum could reveal a condensation of the lowest

band to zero energy at $B \approx 1$ T, consistent with a change of slope in the specific heat for $Ca_{10}Cr_7O_{28}$, seen in Fig. 5.1(b).

$Ca_{10}Cr_7O_{28}$ also provides signatures of a Coulombic spin liquid at finite energies. Higher energy bands show broad bow–tie features, which develop into pinch–points in magnetic field, comparable to those in the classical antiferromagnetic Heisenberg model on the kagome lattice [90, 114, 115]. However, at zero field, those transverse excitations are "smeared" out in momentum space due to its coexistence with longitudinal spin–excitations.

Longitudinal excitations form diffusive, weakly–dispersing gapless bands. The energy of those bands does not move in field, suggesting excitations of multiple spins, with total spin S=0, which do not couple to an external magnetic field. This may be linked to the fact that the magnetisation for $Ca_{10}Cr_7O_{28}$, seen in Fig. 5.1(d) shows two changes of slopes, at ≈ 1 T, and at around 11 T. The system seems not to be fully polarised at intermediate fields, rather than seemingly to enter another phase between 1 and 11 T, where other excitations suppress the system's magnetisation. Such an effect, even though at much larger field, has already be seen in $LiCuVO_4$ [257] suggesting the presence of a spin–nematic phase.

5.6 Conclusions

The aim of this chapter was to present a deeper understanding of the dynamical properties and signatures of the new spin–liquid candidate $Ca_{10}Cr_7O_{28}$, a physical realisation of a S=1/2 magnet on the bilayer breathing kagome (BBK) lattice. Experimental results, provided by Balz *et al.* [127, 249, 250] for the a.c. susceptibility and muon spin relaxation showed that $Ca_{10}Cr_7O_{28}$ is neither a spin glass, nor contains partial order, down to 19 mK, which strongly suggests a spin–liquid ground state. Single crystal inelastic neutron scattering experiments show at zero field three excitation energy scales with "ring" features at low energies and broad bow–tie features at higher energies [127].

In this work, a combination of classical Monte Carlo and molecular dynamics simulations of the Heisenberg model on the BBK lattice could provide high–resolution dynamical structure factors, comparable to previously measured inelastic neutron scattering (INS) results of $Ca_{10}Cr_7O_{28}$ at finite fields. In field, the dynamical structure factor could be separated into transverse and longitudinal channels, whereas the transverse channel shows six doubly–degenerate spin–wave branches and the longitudinal channel shows diffusive, weakly dispersing excitations of low intensity.

It has been shown that the ground state of $Ca_{10}Cr_7O_{28}$ forms a spiral spin–liquid coming from highly degenerate ground states with continuously varying momentum on a ring. $Ca_{10}Cr_7O_{28}$ also shows a Coulombic spin–liquid at finite energies and field, characterised by pinch–points, comparable to those in the classical antiferromagnetic Heisenberg model on the kagome lattice.

One of the remaining challenges is to explain the two changes of slope in the magnetisation at ~ 1 T, and at ~ 11 T [Fig. 5.1(d)]. A possible explanation is the formation of magnon pairs, which could form a quasiparticle with effective S = 0, not coupling to the magnetic field and suppressing the system's magnetisation.

Another interesting suggestion for future work could point at the investigation of

"doped" $Ca_{10}Cr_7O_{28}$, where the Ca ions are exchanged with e.g. K for hole and Sc for electron doping and possibly allow for superconducting properties. Also, chemical pressure could shift the material within the classical phase diagram [Fig. 5.8(a)] to regions, where the spin–liquid regime persists to even lower temperatures.

Chapter 6

Conclusions

" *Natürlich, wenn ein Gott sich erst sechs Tage plagt,*
Und selbst am Ende bravo sagt,
Da muss es was Gescheites werden."

Faust 1, Vers 2441 ff. (Mephistopheles)
Johann W. v. Goethe

Collective electron interactions in spin liquids suppress conventional ordering mechanisms and make their identification and classification in experiments rather complicated. However, spin liquids do show thermodynamic and dynamic signatures, which allow to distinguish them from each other due to their underlying physical nature. In this thesis we tried to make a small contribution to the vast field of highly–frustrated magnetism, by analysing thermodynamic and dynamic signatures of novel spin liquids on kagome–like lattices.

We have first explored a simple Ising model on a variety of corner–sharing lattices in two and three dimensions, by complementary analytical Husimi tree and numerical Monte Carlo simulation techniques. The emerging phenomenon of a Curie–law crossover, reflecting a crossover between Curie–laws for a high–temperature paramagnet and a low–temperature collective paramagnet, turns out to be a unique fingerprint of exotic physics in classical spin liquids, and explains the difficulty of making a precise estimate of the Curie–Weiss temperature in experiments.

Describing the Curie–law crossover of spin liquids in the framework of a Husimi tree calculation allows to validate the deviation of the susceptibility from the high–temperature Curie–Weiss fit. It turns out, that the error for estimating the Curie–Weiss temperature θ_{cw} increases significantly at low temperatures, where materials show their spin–liquid properties. Also, some spin liquids are able to show a succession of Curie–law crossovers, due to a non–monotonic behaviour of correlations, which produces a qualitatively wrong estimate of the sign of θ_{cw} and therefore the type of dominant interactions in the system.

An example of multiple Curie–law crossovers in spin liquids provides the anisotropic Ising model on the shuriken, a.k.a. square–kagome lattice, which is characterised by

a rich phase diagram with multiple disordered phases, surviving down to zero temperatures [1]. Here a binary paramagnetic (BPM) phase, composed of completely decorrelated, locally ordered square plaquettes is surrounded by two classical spin liquids. Thermal fluctuations spread the spin liquid phases into neighbouring regions of the phase diagram, allowing for models which perform a double crossover from a high–temperature paramagnet into a correlated spin liquid and back into a low–temperature paramagnet (BPM phase). This process can be considered as a reentrant behaviour [239, 240, 241, 242, 243] between disordered regimes, in absence of phase transitions, representing an interesting mechanism to stabilise a paramagnetic (gas–like phase) at temperatures below the regime of a classical spin liquid phase.

Possible future directions of this work might involve thermodynamic and dynamic investigations of the classical Heisenberg model on the shuriken lattice, which is supposed to also provide an extensive ground state degeneracy in the isotropic case [208, 215]. Order by disorder effects are expected to occur and form zero–energy fluctuations, comparable to the "weather vane" modes found in the antiferromagnetic Heisenberg model on the kagome lattice. It would also be interesting to extend the Husimi tree formalism to Heisenberg spins and verify its validity by a comparison to Monte Carlo simulations. Results should be comparable in cooperative–paramagnetic regimes, but should give different results at very low temperatures due to characteristic loop–dynamics, which might not be accessible in Husimi tree calculations.

Pointing the focus to dynamical properties in spin liquids, we also studied the low–temperature physics of the nearest–neighbour Heisenberg model on the bilayer breathing kagome lattice, which has been motivated by very recent experiments on $Ca_{10}Cr_7O_{28}$ [127, 249, 250]. Semi–classical molecular–dynamics simulations, allowed us to reproduce many features seen in inelastic neutron scattering experiments, and provide a first explanation of the origin of a spin liquid phase in $Ca_{10}Cr_7O_{28}$. Surprisingly, we find that the magnetic excitations of $Ca_{10}Cr_7O_{28}$ encode not one, but two types of spin liquids; a gapless "spiral spin liquid", with origin in an extensive ground state degeneracy, understandable by a mapping onto the J_1-J_2 honeycomb model; and, at finite energy, a coulombic spin liquid, familiar from the kagome–lattice antiferromagnet.

A mapping of the bilayer breathing kagome model onto the J_1-J_2 honeycomb model provides the missing pice of the puzzle, for an explanation of the "ring" features, seen in inelastic neutron scattering experiments for $Ca_{10}Cr_7O_{28}$, pseudofermion functional renormalisation group calculations and molecular dynamics simulations. For a specific parameter region in the phase diagram, relevant to $Ca_{10}Cr_7O_{28}$, this model allows for two coexisting spiral ground states with different momentum ordering **q**-vectors. Highly degenerate ground states with continuously varying momentum on a ring emerge and give rise to the spin–liquid behaviour, seen in $Ca_{10}Cr_7O_{28}$.

Higher energy bands show broad bow–tie features, which develop into pinch points in magnetic field, comparable to those in the classical antiferromagnetic Heisenberg model on the kagome lattice. However, at zero field, those transverse excitations are "smeared" out in momentum space due to their coexistence with longitudinal spin excitations.

Longitudinal excitations form diffusive, weakly dispersing gapless bands. Their

energy does not move in field, suggesting excitations of multiple spins in form of magnon pairs with total spin S=0, which do not couple to an external magnetic field. This might link to the fact that the magnetisation for $Ca_{10}Cr_7O_{28}$ shows two changes of slope at $\sim$ 1 T and $\sim$ 11T, indicating a transition between different phases. Such an effect, even though at much larger fields, has already be seen in $LiCuVO_4$ [257], suggesting the presence of a spin–nematic phase.

Further investigations of quantum models on the bilayer breathing kagome lattice with exact diagonalization, field theories and the formulation of tensor product states in two dimensions might provide the methods to resolve missing pieces in understanding the magnetic properties in $Ca_{10}Cr_7O_{28}$ completely. Further suggestions for future work on the experimental side, could point at the investigation of doped $Ca_{10}Cr_7O_{28}$, where the Ca ions are exchanged with e.g. K for hole and Sc for electron doping and possibly allow for superconducting properties. Also, chemical pressure could shift the material within the classical phase diagram to regions, where the spin–liquid regime persists to even lower temperatures.

To conclude, this thesis presented various thermodynamic and dynamic signatures in novel spin liquids on kagome–like lattices. Since spin liquids behave very different from conventional magnets, a comprehensive understanding of their physical nature helps to identify and classify them in theory and experiment.

Because spin liquids do not order or freeze, they show strong correlation effects even at very low temperatures. The nature of those correlations can be directly used to identify and classify them, as seen by single and multiple crossovers between high– and low–temperature Curie–laws. Signatures of different spin liquids can be revealed in spin–structure factors, as shown for a Coulombic spin liquid by pinch–point singularities and a spiral spin liquid by ring signatures, both combined in one material: $Ca_{10}Cr_7O_{28}$.

The knowledge of such signatures hopefully allows to find and identify new spin–liquid materials in the future. Such signatures might not only be important to spin liquids, but possibly also to superconducting materials, which require magnetic fluctuating ground states. Large–scale Monte Carlo simulations might be improved by parallelisation techniques available in GPU programming, and possibly can also be extended to quantum models.

Appendix A

Supplementary Information for Chapter 1

A.1 Thermodynamics of classical oscillators

At low temperatures ordered magnets allow excitations to propagate through the lattice. In the classical limit ($S \to \infty$) these excitations can be treated as classical oscillators with an energy

$$E = \frac{p^2}{2m} + \frac{1}{2}\kappa_2 q^2 + \frac{1}{4!}\kappa_4 q^4 \ . \tag{A.1}$$

Without loss of generality, the mass can be set to $m = 1$ and one writes:

$$E = \frac{1}{2}(p^2 + \omega_0^2 q^2) + \frac{\kappa_4}{4!}q^4 \ , \tag{A.2}$$

where ω_0 is the frequency of the oscillator. The energy considers also higher–order terms in the expansion of the momentum–dependent energy in form of an quartic term. The partition function will give

$$\mathcal{Z} = \frac{1}{2\pi}\int dp e^{-\frac{\beta}{2}p^2}\int dq e^{-\frac{\beta}{2}\omega_0^2 q^2} e^{-\frac{\beta}{4!}\kappa_4 q^4} \ . \tag{A.3}$$

Considering first the general case with $\kappa_4 = 0$ gives the unperturbed partition function

$$\mathcal{Z} = \frac{T}{4T_0} \ , \tag{A.4}$$

The internal energy and specific heat is

$$\mathcal{E}_0 = T^2\frac{\partial}{\partial T}\ln \mathcal{Z} = T \tag{A.5}$$

$$\mathcal{C}_0 = \frac{\partial}{\partial T}\mathcal{E}_0 = 1 \ , \tag{A.6}$$

where one directly can see that the specific heat is insensitive of the oscillation frequency ω_0. Note that the free energy

$$\mathcal{F}_0 = -T\ln \mathcal{Z} \tag{A.7}$$

$$= -T\ln T + T\ln 4\omega_0 \ , \tag{A.8}$$

and the entropy

$$\mathcal{S}_0 = -\left(\frac{\partial \mathcal{F}_0}{\partial T}\right) \tag{A.9}$$

$$= \ln T + 1 - \ln 4\omega_0 \tag{A.10}$$

explicitly depends on ω_0. That means that low frequency oscillations play a crucial role in minimising the free energy of the system. Modes with very small frequencies $\omega < 1/4$ will raise the system's entropy, and therefore reduce the free energy $\mathcal{F}_0$, a typical order by disorder effect, where small oscillations in the system are preferred. Small ω_0 make the harmonic term in Eq. (A.2) vanish, which is why the consideration of next–order anharmonic terms are essential.

In the case of anharmonic contributions in the energy, the partition function will be

$$\mathcal{Z} = \frac{1}{4}\frac{T}{T_0}\left[1 - \frac{T}{2T_0}\right] \tag{A.11}$$

where $T_0 = 4\omega^4/\kappa_4$ can be seen as an effective, mean–field treatment of interactions between different oscillator modes. The anharmonic term will modify physical observables as

$$\mathcal{C} = T - \frac{T}{T_0}\,, \tag{A.12}$$

$$\mathcal{F} = -T\ln T + T\ln 4\omega_0 + \frac{T^2}{2T_0}\,, \tag{A.13}$$

$$\mathcal{S} = \ln T + 1 - \ln 4\omega_0 - \frac{T}{T_0}\,. \tag{A.14}$$

Deviation away from $\mathcal{C} = 1$ will count the number of modes in the system, which explicitly in the case of the Heisenberg antiferromagnet on the kagome lattice is 11/12. The case $\omega_0 = 0$ needs to be treated separately, since ln will diverge in this limit. Also, this arguments do not depend on energy and can be seen in static spin configurations as well.

Appendix B

Supplementary Information for Chapter 2

B.1 Detailed balance in parallel tempering

In order to show that the parallel tempering algorithm, presented in Section 2.2.5 with Eq. (2.74) is correct, one needs to prove ergodicity and the sufficient detailed balance condition. Parallel tempering, as a multicanonical sampling method just accounts for the exchange of replicas, due to their energy and temperature properties. It does not actively sample new spin configurations, which is why the ergodicity of the algorithm is defined by the ergodicity of every individual joint Monte Carlo algorithm, as e.g. the single–spin flip Metropolis algorithm, which is assumed to satisfy ergodicity and detailed balance.

The detailed balance condition needs slightly more careful considerations. One consider the joint probability $p_{\mu\nu}$, stating that the system will be for the low temperature T_{low} in state μ and for the high temperature T_{high} in state ν. This joint probability needs to respect the Boltzmann distribution

$$p_{\mu\nu} = \frac{1}{Z_{\text{low}} Z_{\text{high}}} e^{-\beta_{\text{low}} E_\mu} e^{-\beta_{\text{high}} E_\nu} \ , \tag{B.1}$$

where Z_{low} and Z_{high} are the partition functions of the two systems. Following the detailed balance condition from Eq. (2.26) one can formulate:

$$\frac{P(\mu\nu \to \mu'\nu')}{P(\mu'\nu' \to \mu\nu)} = \frac{p_{\mu'\nu'}}{p_{\mu\nu}} = \frac{e^{-\beta_{\text{low}} E_{\mu'}} e^{-\beta_{\text{high}} E_{\nu'}}}{e^{-\beta_{\text{low}} E_\mu} e^{-\beta_{\text{high}} E_\nu}} \ . \tag{B.2}$$

Three kinds of moves will occur in such a system. Two of them will be simple Monte Carlo single–spin flip moves, one for the high temperature and one for the low temperature system, where the third one will be the swap between these systems. The sing–spin flip Monte Carlo moves respect detailed balance, which can be shown for the case that in the low temperature system the state transforms from $\mu \to \mu'$, while the high temperature system dos not transform ($\nu \to \nu$). Using Eq. (B.2) one can write:

$$\frac{P(\mu\nu \to \mu'\nu)}{P(\mu'\nu \to \mu\nu)} = \frac{e^{-\beta_{\text{low}} E_{\mu'}}}{e^{-\beta_{\text{low}} E_\mu}} \ , \tag{B.3}$$

which is the simple detailed balance condition, provided by Eq. (2.29). Any single–spin flip Monte Carlo move will satisfy this condition and therefore detailed balance. The proof for the high–temperature system is identical.

In order to show, that the swapping move respects detailed balance as well, one needs to consider the final states $\mu' = \nu$ and $\nu' = \mu$ since we exchanged the high with the low temperature system. Hereby one gets

$$\frac{P(\mu\nu \to \nu\mu)}{P(\nu\mu \to \mu\nu)} = \frac{e^{-\beta_{\text{low}} E_\nu} e^{-\beta_{\text{high}} E_\mu}}{e^{-\beta_{\text{low}} E_\mu} e^{-\beta_{\text{high}} E_\nu}} = e^{-(\beta_{\text{low}} - \beta_{\text{high}})(E_\nu - E_\mu)} \,, \tag{B.4}$$

which is the condition, provided by Eq. (2.74). Therefore each of the three moves respects detailed balance and therefore also does the whole algorithm.

B.2 Linear spin–wave theory

Spin–wave theory is a very useful tool to study the magnetic excitation spectrum on top of an ordered ground state. The basic concept of linear spin–wave theory shall be visualised on the example of the antiferromagnetic Heisenberg model on the square lattice and can be looked up in detail in the literature [258, 43]. Classically this model shows a Néel–long range ordered ground state, while quantum fluctuations allow to reduce its energy even further. The common Heisenberg model from Eq. (1.23) can be rewritten for the specific case of the bipartite square lattice as

$$\begin{aligned} \mathcal{H} &= J \sum_{i \in A, \delta}^{N/2} \mathbf{S}_i \mathbf{S}_{i+\delta} \,, \\ &= J \sum_{i \in A, \delta} \left[\mathbf{S}_i^z \mathbf{S}_{i+\delta}^z + \frac{1}{2} \left(\mathbf{S}_i^+ \mathbf{S}_{i+\delta}^- + \mathbf{S}_i^- \mathbf{S}_{i+\delta}^+ \right) \right] , \end{aligned} \tag{B.5}$$

where the sum has been performed just over the sublattice A, and $\mathbf{S}^+ = S^x + iS^y$ and $\mathbf{S}^- = S^x - iS^y$ are the spin–ladder operators.

Magnons created on top of the classical ordered ground state can be described by Holstein–Primakoff bosons with a distinction between different sublattice

	Sublattice A	Sublattice B
$\hat{S}^z$	$S - \hat{a}^\dagger \hat{a}$	$-S + \hat{b}^\dagger \hat{b}$
$\hat{S}^+$	$\sqrt{2S}\ \hat{a}$	$\sqrt{2S}\ \hat{b}^\dagger$
$\hat{S}^-$	$\sqrt{2S}\ \hat{a}^\dagger$	$\sqrt{2S}\ \hat{b}$

This description corresponds to the linear order, specifying the theory to linear spin–wave theory.

A Fourier transform of the bosonic operators into momentum space

$$\hat{a}_i^\dagger = \frac{1}{\sqrt{N}} \sum_k^N e^{-i\mathbf{r}_i \mathbf{k}} \hat{a}_k^\dagger \,, \tag{B.6}$$

$$\hat{a}_i = \frac{1}{\sqrt{N}} \sum_k^N e^{i\mathbf{r}_i \mathbf{k}} \hat{a}_k \,, \tag{B.7}$$

allows to express Eq. (B.5) in momentum space

$$\mathcal{H} = \mathcal{H}_0 + \mathcal{H}_1 \ ,$$
$$\mathcal{H}_0 = -2JS^2N \ , \tag{B.8}$$
$$\mathcal{H}_1 = 4JS \sum_k \left[\gamma_{\mathbf{k}} \left(\hat{a}_k \hat{b}_{-k} + \hat{a}^\dagger_{-k} \hat{b}^\dagger_k \right) + \left(\hat{a}^\dagger_k \hat{a}_k + \hat{b}^\dagger_k \hat{b}_k \right) \right] \ , \tag{B.9}$$

where $\mathcal{H}_0$ corresponds to the classical Néel–ordered ground state energy and $\mathcal{H}_1$ to the Hamiltonian describing spin excitations on top of it. The geometrical factor depends on the real space lattice and is defined as

$$\gamma_{\mathbf{k}} = \frac{1}{4} \sum_\delta e^{i\mathbf{k}\delta} \ . \tag{B.10}$$

However, this is not the end of the game yet. Unfortunately Eq. (B.9) does not show a diagonal form, as it would be necessary to calculate its energy dispersion. Occupation numbers of $\hat{a}_k$ and $\hat{b}_k$ are not conserved, in fact they mix.

In order to express Eq. (B.9) in an orthogonal basis, one needs to perform a Bogoliubov transformation.

$$\hat{a}_k = u_{\mathbf{k}} \hat{\alpha}_{\mathbf{k}} + v_{\mathbf{k}} \hat{\beta}^\dagger_{-\mathbf{k}} \ , \qquad \hat{a}^\dagger_k = u_{\mathbf{k}} \hat{\alpha}^\dagger_{\mathbf{k}} + v_{\mathbf{k}} \hat{\beta}_{-\mathbf{k}} \ , \tag{B.11}$$
$$\hat{b}_k = u_{\mathbf{k}} \hat{\beta}_{\mathbf{k}} + v_{\mathbf{k}} \hat{\alpha}^\dagger_{-\mathbf{k}} \ , \qquad \hat{b}_k = u_{\mathbf{k}} \hat{\beta}^\dagger_{\mathbf{k}} + v_{\mathbf{k}} \hat{\alpha}_{-\mathbf{k}} \ . \tag{B.12}$$

Hereby, the introduced operators $\hat{\alpha}^\dagger, \hat{\alpha}$ and $\hat{\beta}^\dagger, \hat{\beta}$, are defined on sublattice A and B respectively and satisfy boson commutation relations

$$[\hat{\alpha}_k, \hat{\alpha}^\dagger_{k'}] = \delta_{k,k'} \ , \tag{B.13}$$
$$[\hat{\beta}_k, \hat{\beta}^\dagger_{k'}] = \delta_{k,k'} \ , \tag{B.14}$$

and the pre–factors $u_{\mathbf{k}}$ and $v_{\mathbf{k}}$ are constrained, such

$$u^2_{\mathbf{k}} - v^2_{\mathbf{k}} = 1 \ . \tag{B.15}$$

Rewriting Eq. (B.9) in its symmetric form according to $\sum_{\mathbf{k}} = (\sum_{\mathbf{k}} + \sum_{-\mathbf{k}})/2$ allows to obtain the an equation for $\mathcal{H}$, which is diagonal in the occupation number

$$\mathcal{H} = -2NS(S+1) + 4JS \sum_{\mathbf{k}} \sqrt{1-\gamma^2_{\mathbf{k}}} \left[\left(\hat{\alpha}^\dagger_{\mathbf{k}} \hat{\alpha}_{\mathbf{k}} + \frac{1}{2} \right) + \left(\hat{\beta}^\dagger_{\mathbf{k}} \hat{\beta}_{\mathbf{k}} + \frac{1}{2} \right) \right] \ , \tag{B.16}$$

with the spin–wave dispersion

$$\omega_{\mathbf{k}} = 4JS\sqrt{1-\gamma^2_{\mathbf{k}}} \ . \tag{B.17}$$

The spin–wave dispersion energy is hereby two–fold degenerate, since $\hat{\alpha}^\dagger$ and $\hat{\beta}^\dagger$ in Eq. (B.16) create magnons on each sublattice . In the long–wavelength limit $\sqrt{1-\gamma^2_{\mathbf{k}}} \approx |\mathbf{k}|a$, whit a the lattice constant, thus the spectrum shows no presence of a excitation gap

$$\omega_{\mathbf{k}} \approx 4JSa|\mathbf{k}| \ , \tag{B.18}$$

and shows the presence of Goldstone modes. The ground state energy

$$E_0 = -2JNS^2 + 4JS \sum_{\mathbf{k}} \left(\sqrt{1 - \gamma_{\mathbf{k}}} - 1 \right) \tag{B.19}$$

shows a value smaller than provided for the classical ground state $\mathcal{H}_0$ in Eq. (B.8), due to the presence of quantum fluctuations.

Appendix C

Supplementary Information for Chapter 4

C.1 The shuriken lattice in Monte Carlo simulations

The definition of the shuriken lattice, as shown in Fig. 4.1(a) considers equilateral triangles within the unit cell, whereas the site coordinates are

$$\begin{aligned} \mathbf{r}_1 &= (-\alpha, -\alpha)a, & \mathbf{r}_2 &= (\alpha, -\alpha)a, \\ \mathbf{r}_3 &= (\alpha, \alpha)a, & \mathbf{r}_4 &= (-\alpha, \alpha)a, \\ \mathbf{r}_5 &= (1/2, 0)a, & \mathbf{r}_6 &= (0, 1/2)a, \end{aligned} \tag{C.1}$$

where the irrational number

$$\alpha = \frac{1}{4}(\sqrt{3} - 1) \tag{C.2}$$

is used to define the positions of sites within the unit cells. The origin of the unit cells form a square lattice, with lattice constant a.

The structure factor for the lattice sites is defined as

$$I(\mathbf{q}) = \frac{1}{N_{uc}} \Big| \sum_i e^{-i\mathbf{q}\cdot\mathbf{r}_i} \Big|^2 , \tag{C.3}$$

which sums over all N_{uc} unit cells within the whole lattice. Since the shuriken lattice corresponds to a Bravais square lattice with six sites per unit cell, its structure factor will also form a square lattice in reciprocal space with Bragg peaks located at

$$\mathbf{q} = (q_x, q_y) = \frac{2\pi}{a}(n, m), \qquad n, m \in \mathbb{Z}. \tag{C.4}$$

As a function of n and m (set $a = 1$), the intensity of the structure factor will be modulated as

$$I\left(\mathbf{q} = 2\pi(n, m)\right) = N_{uc} \Big| 4 \cos\left(\frac{\pi\, n}{1+\sqrt{3}}\right) \cos\left(\frac{\pi\, m}{1+\sqrt{3}}\right) + (-1)^n + (-1)^m \Big|^2 . \tag{C.5}$$

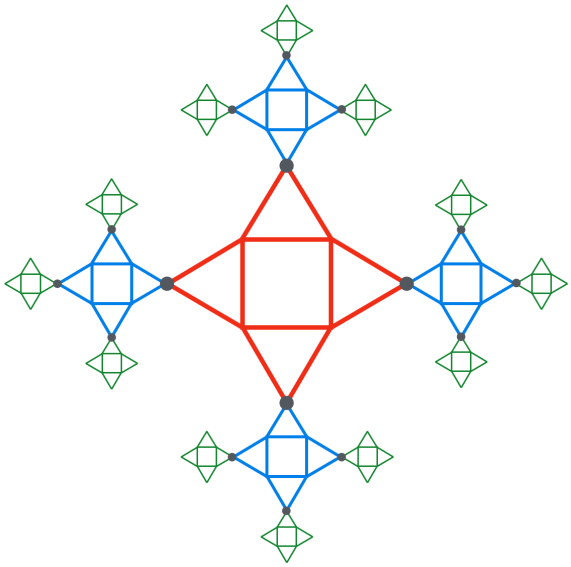

Figure C.1: The Husimi tree for the shuriken lattice. The Husimi tree is made of shuriken unit cells and shows tow successive layers, which are connected via sites on the B sublattice (same colour code of shell as in Fig. 2.2 of Section 2.1). Even though closed loops of size 8 and beyond do not exist.

Since the relative coordinates of the lattice sites within the unit cell are irrational [Eq. (C.1)], the phase factor in Eq. (C.5) will modulate $I(\mathbf{q})$ such that it becomes aperiodic, when restricted to the grid allowed $\mathbf{q}$–values [Eq. (C.4)] in momentum space. Such a behaviour causes the aperiodic pattern seen in the structure factor for the lattice sites in Fig. 4.1(b) and also in the spin–spin correlation function in momentum space, shown in Fig. 4.9(a) and Fig. 4.9(c). These complications due to the irrationality of α disappear for non-equilateral triangles as shown in Appendix C.3.

C.2 The shuriken lattice on the Husimi tree

Fig. C.1 shows the Husimi tree for the shuriken lattice in the same convention as used in Fig. 2.2 of Section 2.1. Branches from the central shell (red) do just evolve from the B sites and do not allow for loops of size 8 and beyond. Following Eq. (2.12) the partition function the A sites and B sites within the central shell will provide the energy and entropy

$$E = -\frac{2}{3}\,\frac{1+6\psi\phi+2\phi\psi^3-\psi^4}{1+6\psi^2+\psi^4} \tag{C.6}$$

$$S = \frac{1}{6}\ln 8 \;+\; \frac{1}{6}\ln(1+6\psi^2+\psi^4) + \;\frac{2\beta}{3}\,\frac{2\psi(\psi-\phi)(3+\psi^2)}{1+6\psi^2+\psi^4}$$

where

$$\kappa = 16\,e^{4\beta}\left(1+6\psi^2+\psi^4\right)\;, \tag{C.7}$$

$$\psi = e^{-2\beta}\,\cosh(2\beta x)\;, \tag{C.8}$$

$$\phi = e^{-2\beta}\,x\,\sinh(2\beta x)\;, \tag{C.9}$$

and where we set $k_B = 1$ with x defined in Eq. (4.4). The specific heat C_h is obtained by a differentiation of the energy with respect to the temperature at zero magnetic field. The susceptibility χ is obtained from evaluating Eq. (2.11) for the A and B sites in the unit cell.

C.3 The non–equilateral shuriken lattice

The relative positions of sites in the shuriken lattice [Fig. 4.1(a)] are irrational and therefore cause very complex aperiodic structure factors [Fig. 4.1(b) and Fig. 4.9]. A modification of the shuriken lattice, by transforming the equilateral triangles into non–equilateral triangles reproduces a lattice as shown in Fig. C.2(a). It transforms into a decorated square or Lieb lattice with nearest–neighbour interactions J_{AB} and specific further–neighbour interactions J_{AA}.

The structure factor of the lattice sites [Fig. C.2(b)] reproduces the symmetry of the square lattice in momentum space with a phase modulation affecting the intensity $I(\mathbf{q})$ [Eq. (C.3)] for the allowed $\mathbf{q}$–points [Eq. (C.4)]. Spin–spin correlation functions $S(\mathbf{q})$ for Fig. C.2(c) x=-1, and (e) x = 1 show a simpler structure factor compared to Fig. 4.9(a) and Fig. 4.9(b).

Since the length of the J_{AA} bonds (red) in Fig. C.2(a) are not modified, and B sites decorrelate ordered square plaquettes in the binary paramagnet phase (as discussed in Section 4.2.2), the $S(\mathbf{q})$ for (d) x = 0 shows the same pattern as in the shuriken lattice with equilateral triangles [Fig. 4.9(b)].

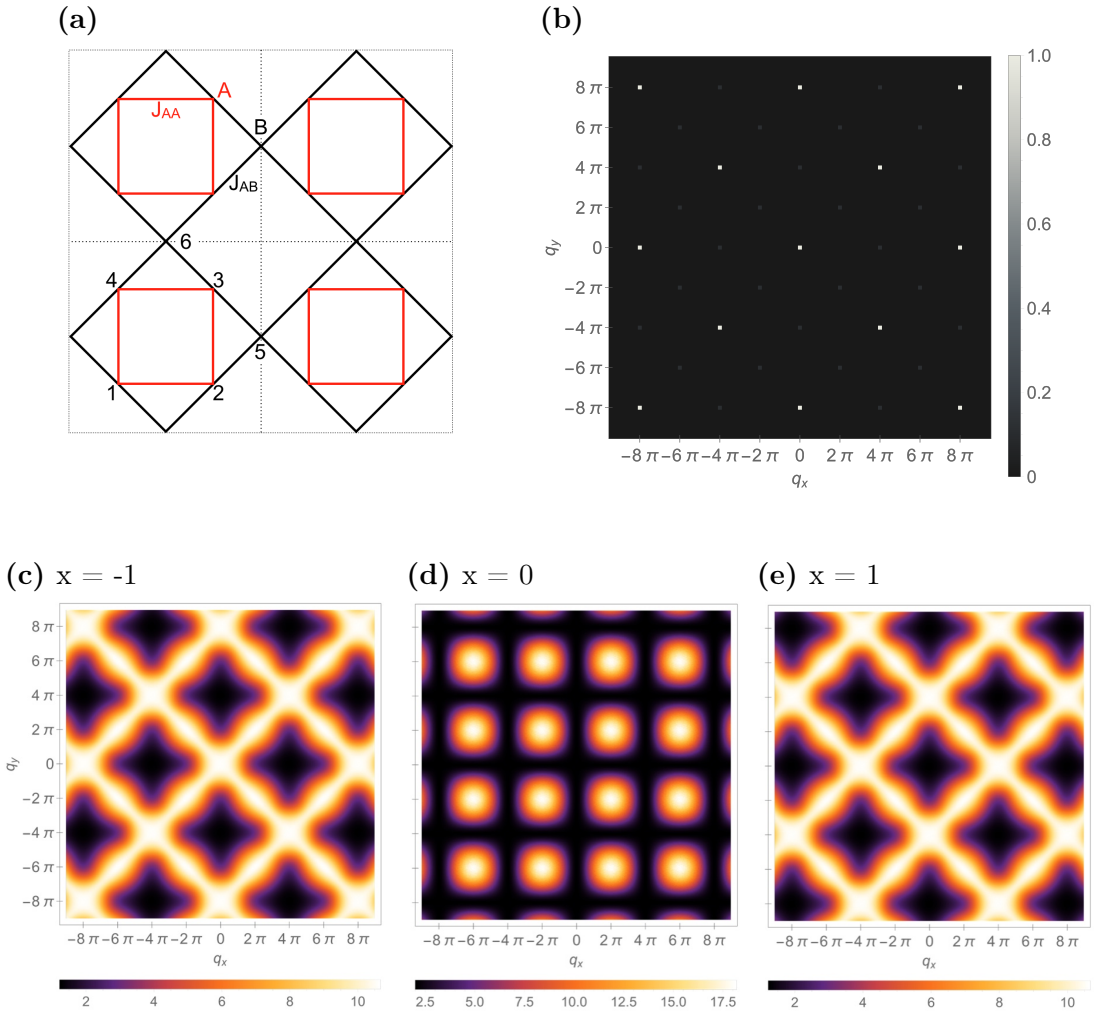

Figure C.2: Non–equilateral triangles in the shuriken lattice. (a) The shuriken lattice with non–equilateral triangles, forming a decorated square/Lieb lattice with specific next–nearest neighbour interactions J_{AA}. (b) Distribution and intensity of Bragg peaks in reciprocal space, reproduces the symmetry of the square lattice in momentum space. (c)–(e) Static structure factors for $x = 0, \pm 1$ in order to compare with Fig. 4.9(a)–(c).

Appendix D

Supplementary Information for Chapter 5

D.1 Magnetic form factor of Cr^{5+}

In order to compare molecular dynamics simulations of the Heisenberg model on the breathing kagome bilayer (BBK) model [Eq. (5.1)] to inelastic neutron scattering experiments of $Ca_{10}Cr_7O_{28}$, one needs to take the magnetic form–factor $\mathcal{F}(\mathbf{q})$ [see Eq. (2.100) in Section 2.4.1] of the magnetic Cr^{5+} into account.

$\mathcal{F}(\mathbf{q})$ for 3-d transition metal ions is given by [259]:

$$\mathcal{F}(\mathbf{k}) = \langle j_0 \rangle(\mathbf{k}) + \left(1 - \frac{2}{g}\right) \langle j_2 \rangle(\mathbf{k}) \,, \tag{D.1}$$

where the gyromagnetic ratio is assumed to be $g = 2$. The necessary quantity is $\langle j_0 \rangle$, which is given as

$$\langle j_0 \rangle(\mathbf{k}) = A e^{-a\mathbf{k}^2} + B e^{-b\mathbf{k}^2} + C e^{-c\mathbf{k}^2} + D \tag{D.2}$$

From private communication with *Christian Balz*, coefficients in Eq. (D.2) have been assigned to

$$A = -0.2602 \,, \quad B = 0.33655 \,, \quad C = 0.90596 \,, \quad D = 0.0159 \tag{D.3}$$

$$a = 0.03958 \,, \quad b = 15.24915 \,, \quad c = 3.2568 \,. \tag{D.4}$$

Comparison of INS data has been done via Eq. (2.100) for $\mathbf{k} = |\mathbf{q}|/4\pi$.

Bibliography

[1] R. Pohle, O. Benton, and L. D. C. Jaubert, "Reentrance of disorder in the anisotropic shuriken ising model," *Phys. Rev. B*, vol. 94, p. 014429, Jul 2016.

[2] L. Balents, "Spin liquids in frustrated magnets," *Nature*, vol. 464, pp. 53–107, 03 2010.

[3] C. Lacroix, P. Mendels, and F. Mila, *Introduction to Frustrated Magnetism: Materials, Experiments, Theory*. Springer Series in Solid-State Sciences, Springer Berlin Heidelberg, 2011.

[4] P. W. Anderson, "Coherent excited states in the theory of superconductivity: Gauge invariance and the meissner effect," *Phys. Rev.*, vol. 110, pp. 827–835, May 1958.

[5] P. W. Anderson, "Random-phase approximation in the theory of superconductivity," *Phys. Rev.*, vol. 112, pp. 1900–1916, Dec 1958.

[6] P. W. Anderson, "Superconductivity: Higgs, anderson and all that," *Nat Phys*, vol. 11, p. 93, 2015.

[7] C. Castelnovo, R. Moessner, and S. L. Sondhi, "Magnetic monopoles in spin ice," *Nature*, vol. 451, pp. 42–45, 2008.

[8] L. D. C. Jaubert and P. C. W. Holdsworth, "Signature of magnetic monopole and dirac string dynamics in spin ice," *Nat Phys*, vol. 5, pp. 258–261, 2009.

[9] Q. L. He, L. Pan, A. L. Stern, E. C. Burks, X. Che, G. Yin, J. Wang, B. Lian, Q. Zhou, E. S. Choi, K. Murata, X. Kou, Z. Chen, T. Nie, Q. Shao, Y. Fan, S.-C. Zhang, K. Liu, J. Xia, and K. L. Wang, "Chiral majorana fermion modes in a quantum anomalous hall insulator–superconductor structure," *Science*, vol. 357, no. 6348, pp. 294–299, 2017.

[10] P. Curie, *Propriétés magnétiques des corps à diverses températures*. PhD thesis, à la faculté des sciences de Paris, 1895.

[11] P. Weiss, "L'hypothèse du champ moléculaire et la propriété ferromagnétique," *J. Phys. Theor. Appl.*, vol. 6, no. 1, pp. 661–690, 1907.

[12] D. Mattis, *The Theory of Magnetism Made Simple: An Introduction to Physical Concepts and to Some Useful Mathematical Methods*. World Scientific, 2006.

[13] W. Lowrie, *Fundamentals of Geophysics.* Cambridge, University Press, 2 ed., 2007.

[14] P. P. de Maricourt, "The letter of petrus peregrinus on the magnet, a.d. 1269." New York: McGraw publishing company, 1904.

[15] W. Gilbert, *De Magnete.* Dover Publications Inc., New York, 1958.

[16] H. C. Ørsted, *Selected Scientific Works of Hans Christian Ørsted.* Princeton University Press, 1998.

[17] J. C. Maxwell, "On physical lines of force." Philosophical Magazine, 1861.

[18] J. C. Maxwell, "A dynamical theory of the electromagnetic field," *Phil. Trans. R. Soc. Lond.*, vol. 155, pp. 459–512, January 1865.

[19] J. C. Maxwell, *A treatise on electricity and magnetism.* Oxford : Clarendon Press, 1873.

[20] M. Planck, *The Theory of Heat Radiation.* Philadelphia, P. Blakiston's Son & Co, 1914.

[21] A. Einstein, "Über einen die erzeugung und verwandlung des lichtes betreffenden heuristischen gesichtspunkt," *Ann. Phys.*, vol. 17, pp. 132–148, 1905.

[22] N. Bohr, "I. on the constitution of atoms and molecules," *Philosophical Magazine Series 6*, vol. 26, no. 151, pp. 1–25, 1913.

[23] W. Gerlach and O. Stern, "Der experimentelle nachweis der richtungsquantelung im magnetfeld," *Zeitschrift für Physik*, vol. 9, no. 1, pp. 349–352, 1922.

[24] A. H. Compton, "The magnetic electron," *Journal of the Franklin Institute*, vol. 192, no. 2, pp. 145 – 155, 1921.

[25] G. E. Uhlenbeck and S. Goudsmit, "Ersetzung der hypothese vom unmechanischen zwang durch eine forderung bezüglich des inneren verhaltens jedes einzelnen elektrons," *Die Naturwissenschaften*, vol. 13, no. 47, pp. 953–954, 1925.

[26] L. de Broglie, "Ondes et quanta," *C. R. Acad. Sci. (Paris)*, vol. 177, pp. 507–510, 1923.

[27] E. Schrödinger, "An undulatory theory of the mechanics of atoms and molecules," *Phys. Rev.*, vol. 28, pp. 1049–1070, Dec 1926.

[28] C. Kittel, *Introduction to Solid State Physics.* John Wiley & Sons, Inc, 8 ed., 2005.

[29] N. Ashcroft and N. Mermin, *Solid State Physics.* HRW international editions, Holt, Rinehart and Winston, 1976.

[30] J. H. de Boer and E. J. W. Verwey, "Semi-conductors with partially and with completely filled 3 d -lattice bands," *Proceedings of the Physical Society*, vol. 49, no. 4S, p. 59, 1937.

[31] N. F. Mott, "The basis of the electron theory of metals, with special reference to the transition metals," *Proceedings of the Physical Society. Section A*, vol. 62, no. 7, p. 416, 1949.

[32] M. Imada, A. Fujimori, and Y. Tokura, "Metal-insulator transitions," *Rev. Mod. Phys.*, vol. 70, pp. 1039–1263, Oct 1998.

[33] P. A. Lee, N. Nagaosa, and X.-G. Wen, "Doping a mott insulator: Physics of high-temperature superconductivity," *Rev. Mod. Phys.*, vol. 78, pp. 17–85, Jan 2006.

[34] N. F. Mott, *Metal–insulator Transitions.* Taylor & Francis Ltd, London, 1974.

[35] T. V. Ramakrishnan, *Metal Insulator Transitions*, p. 23. Taylor & Francis, London, 1985.

[36] N. Bohr, "ii. the doctor's dissertation (text and translation)," *Niels Bohr Collected Works*, vol. 1, pp. 163 – 393, 1972.

[37] H.-J. Van Leeuwen, "Problèmes de la théorie électronique du magnétisme," *J. Phys. Radium*, vol. 2, no. 12, pp. 361–377, 1921.

[38] M. C. Gutzwiller, "Effect of correlation on the ferromagnetism of transition metals," *Phys. Rev. Lett.*, vol. 10, pp. 159–162, Mar 1963.

[39] J. Kanamori, "Electron correlation and ferromagnetism of transition metals," *Progress of Theoretical Physics*, vol. 30, no. 3, p. 275, 1963.

[40] J. Hubbard, "Electron correlations in narrow energy bands," *Proceedings of the Royal Society of London A: Mathematical, Physical and Engineering Sciences*, vol. 276, no. 1365, pp. 238–257, 1963.

[41] J. Hubbard, "Electron correlations in narrow energy bands. ii. the degenerate band case," *Proceedings of the Royal Society of London A: Mathematical, Physical and Engineering Sciences*, vol. 277, no. 1369, pp. 237–259, 1964.

[42] J. Hubbard, "Electron correlations in narrow energy bands. iii. an improved solution," *Proceedings of the Royal Society of London A: Mathematical, Physical and Engineering Sciences*, vol. 281, no. 1386, pp. 401–419, 1964.

[43] P. Fazekas, *Lecture Notes on Electron Correlation and Magnetism.* World Scientific, 1999.

[44] J. Spatek and A. Oles, "Ferromagnetism in narrow s-band with inclusion of intersite correlations," *Physica B+C*, vol. 86, pp. 375 – 377, 1977.

[45] J. Spałek, "Effect of pair hopping and magnitude of intra-atomic interaction on exchange-mediated superconductivity," *Phys. Rev. B*, vol. 37, pp. 533–536, Jan 1988.

[46] Y. A. Izyumov, "Strongly correlated electrons: the t-j model," *Physics-Uspekhi*, vol. 40, no. 5, p. 445, 1997.

[47] P. A. Lee, N. Nagaosa, T.-K. Ng, and X.-G. Wen, "Su(2) formulation of the $t-j$ model: Application to underdoped cuprates," *Phys. Rev. B*, vol. 57, pp. 6003–6021, Mar 1998.

[48] I. Dzyaloshinsky, "A thermodynamic theory of "weak" ferromagnetism of antiferromagnetics," *Journal of Physics and Chemistry of Solids*, vol. 4, no. 4, pp. 241 – 255, 1958.

[49] T. Moriya, "Anisotropic superexchange interaction and weak ferromagnetism," *Phys. Rev.*, vol. 120, pp. 91–98, Oct 1960.

[50] L. P. Kadanoff, "More is the same; phase transitions and mean field theories," *Journal of Statistical Physics*, vol. 137, no. 5, p. 777, 2009.

[51] L. Onsager, "Crystal statistics. i. a two-dimensional model with an order-disorder transition," *Phys. Rev.*, vol. 65, pp. 117–149, Feb 1944.

[52] H. A. Bethe, "Statistical theory of superlattices," *Proceedings of the Royal Society of London A: Mathematical, Physical and Engineering Sciences*, vol. 150, no. 871, pp. 552–575, 1935.

[53] M. Plischke and B. Bergersen, *Equilibrium Statistical Physics*. World Scientific, 3rd ed., 2007.

[54] M. Ostilli, "Cayley trees and bethe lattices: A concise analysis for mathematicians and physicists," *Physica A: Statistical Mechanics and its Applications*, vol. 391, no. 12, pp. 3417 – 3423, 2012.

[55] R. J. Baxter, *Exactly Solved Models in Statistical Mechanics*. Dover books on physics, Courier Corporation, 1982.

[56] L. Landau, "On the theory of phase transitions," *Zh. Eksp. Teor. Fiz.*, vol. 7, pp. 19–32, 1937.

[57] J.-C. Tolédano, *The Landau theory of phase transitions : application to structural, incommensurate, magnetic, and liquid crystal systems*. World Scientific lecture notes in physics ; vol. 3, Singapore : World Scientific, 1987.

[58] V. L. Ginzburg and L. D. Landau, "On the theory of superconductivity," *Zh. Eksp. Teor. Fiz.*, vol. 20, pp. 1064–1082, 1950.

[59] "73 - on the theory of superconductivity," in *Collected Papers of L.D. Landau* (D. T. Haar, ed.), pp. 546 – 568, Pergamon, 1965.

[60] M. Cyrot, "Ginzburg-landau theory for superconductors," *Reports on Progress in Physics*, vol. 36, no. 2, p. 103, 1973.

[61] M. Tinkham, *Introduction to Superconductivity*. Dover Books on Physics Series, Dover Publications, 2 ed., 1996.

[62] B. Rosenstein and D. Li, "Ginzburg-landau theory of type ii superconductors in magnetic field," *Rev. Mod. Phys.*, vol. 82, pp. 109–168, Jan 2010.

[63] P. Hohenberg and A. Krekhov, "An introduction to the ginzburg–landau theory of phase transitions and nonequilibrium patterns," *Physics Reports*, vol. 572, pp. 1 – 42, 2015.

[64] J. D. Bernal and R. H. Fowler, "A theory of water and ionic solution, with particular reference to hydrogen and hydroxyl ions," *The Journal of Chemical Physics*, vol. 1, no. 8, pp. 515–548, 1933.

[65] L. Pauling, "The structure and entropy of ice and of other crystals with some randomness of atomic arrangement," *Journal of the American Chemical Society*, vol. 57, no. 12, pp. 2680–2684, 1935.

[66] G. Toulouse, J. Vannimenus, and J. M. Maillard, "Spin glasses and roughening transition," *J. Physique Lett.*, vol. 38, no. 22, pp. 459–461, 1977.

[67] J. Villain, "Spin glass with non–random interactions," *Journal of Physics C: Solid State Physics*, vol. 10, no. 10, p. 1717, 1977.

[68] R. Houtappel, "Order-disorder in hexagonal lattices," *Physica*, vol. 16, no. 5, pp. 425 – 455, 1950.

[69] G. H. Wannier, "Antiferromagnetism. the triangular ising net," *Phys. Rev.*, vol. 79, 1950.

[70] P. W. Anderson, "Ordering and antiferromagnetism in ferrites," *Phys. Rev.*, vol. 102, pp. 1008–1013, May 1956.

[71] V. Cannella and J. A. Mydosh, "Magnetic ordering in gold-iron alloys," *Phys. Rev. B*, vol. 6, pp. 4220–4237, Dec 1972.

[72] S. F. Edwards and P. Anderson, "Theory of spin glasses," *Journal of Physics F: Metal Physics*, vol. 5, no. 5, p. 965, 1975.

[73] K. Binder and A. P. Young, "Spin glasses: Experimental facts, theoretical concepts, and open questions," *Rev. Mod. Phys.*, vol. 58, pp. 801–976, Oct 1986.

[74] J. Villain, "Insulating spin glasses," *Zeitschrift für Physik B Condensed Matter*, vol. 33, no. 1, pp. 31–42, 1979.

[75] J. S. Gardner, M. J. P. Gingras, and J. E. Greedan, "Magnetic pyrochlore oxides," *Rev. Mod. Phys.*, vol. 82, pp. 53–107, Jan 2010.

[76] B. Kaufman, "Crystal statistics. ii. partition function evaluated by spinor analysis," *Phys. Rev.*, vol. 76, pp. 1232–1243, Oct 1949.

[77] B. Kaufman and L. Onsager, "Crystal statistics. iii. short-range order in a binary ising lattice," *Phys. Rev.*, vol. 76, pp. 1244–1252, Oct 1949.

[78] L. Pauling, "A resonating-valence-bond theory of metals and intermetallic compounds," *Proceedings of the Royal Society of London A: Mathematical, Physical and Engineering Sciences*, vol. 196, no. 1046, pp. 343–362, 1949.

[79] P. Anderson, "Resonating valence bonds: A new kind of insulator?," *Materials Research Bulletin*, vol. 8, no. 2, pp. 153 – 160, 1973.

[80] P. W. Anderson, *RVB Theory of High Tc Superconductivity*, pp. 295–299. Boston, MA: Springer US, 1987.

[81] S. Okumura, H. Kawamura, T. Okubo, and Y. Motome, "Novel spin-liquid states in the frustrated heisenberg antiferromagnet on the honeycomb lattice," *Journal of the Physical Society of Japan*, vol. 79, no. 11, p. 114705, 2010.

[82] L. Seabra, P. Sindzingre, T. Momoi, and N. Shannon, "Novel phases in a square-lattice frustrated ferromagnet : $\frac{1}{3}$-magnetization plateau, helicoidal spin liquid, and vortex crystal," *Phys. Rev. B*, vol. 93, p. 085132, Feb 2016.

[83] R. Moessner and J. T. Chalker, "Properties of a classical spin liquid: The heisenberg pyrochlore antiferromagnet," *Phys. Rev. Lett.*, vol. 80, pp. 2929–2932, Mar 1998.

[84] R. Moessner and J. T. Chalker, "Low-temperature properties of classical geometrically frustrated antiferromagnets," *Phys. Rev. B*, vol. 58, pp. 12049–12062, Nov 1998.

[85] J. Villain, R. Bidaux, J.-P. Carton, and R. Conte, "Order as an effect of disorder," *Journal de Physique*, vol. 41, no. 11, pp. 1263–1272, 1980.

[86] E. Shender, "Antiferromagnetic garnets with fluctuationally interacting sublattices," *JETP*, vol. 56, p. 178, July 1982.

[87] H. Kawamura and S. Miyashita, "Phase transition of the two-dimensional heisenberg antiferromagnet on the triangular lattice," *Journal of the Physical Society of Japan*, vol. 53, no. 12, pp. 4138–4154, 1984.

[88] C. L. Henley, "Ordering due to disorder in a frustrated vector antiferromagnet," *Phys. Rev. Lett.*, vol. 62, pp. 2056–2059, Apr 1989.

[89] J. T. Chalker, P. C. W. Holdsworth, and E. F. Shender, "Hidden order in a frustrated system: Properties of the heisenberg kagomé antiferromagnet," *Phys. Rev. Lett.*, vol. 68, pp. 855–858, Feb 1992.

[90] M. E. Zhitomirsky, "Octupolar ordering of classical kagome antiferromagnets in two and three dimensions," *Phys. Rev. B*, vol. 78, p. 094423, Sep 2008.

[91] Z. Hiroi, H. Yoshida, Y. Okamoto, and M. Takigawa, "Spin-1/2 kagome compounds: Volborthite vs herbertsmithite," *Journal of Physics: Conference Series*, vol. 145, no. 1, p. 012002, 2009.

[92] M. P. Shores, E. A. Nytko, B. M. Bartlett, and D. G. Nocera, "A structurally perfect s = 1/2 kagomé antiferromagnet," *Journal of the American Chemical Society*, vol. 127, no. 39, pp. 13462–13463, 2005.

[93] I. Syôzi, "Statistics of kagomé lattice," *Progress of Theoretical Physics*, vol. 6, no. 3, p. 306, 1951.

[94] K. Kanô and S. Naya, "Antiferromagnetism. the kagomé ising net," *Progress of Theoretical Physics*, vol. 10, no. 2, p. 158, 1953.

[95] X. Obradors, A. Labarta, A. Isalgué, J. Tejada, J. Rodriguez, and M. Pernet, "Magnetic frustration and lattice dimensionality in $SrCr_8Ga_4O_{19}$," *Solid State Communications*, vol. 65, no. 3, pp. 189 – 192, 1988.

[96] A. S. Wills, A. Harrison, S. A. M. Mentink, T. E. Mason, and Z. Tun, "Magnetic correlations in deuteronium jarosite, a model S = 5/2 kagomé antiferromagnet," *EPL (Europhysics Letters)*, vol. 42, no. 3, p. 325, 1998.

[97] M. Nishiyama, S. Maegawa, T. Inami, and Y. Oka, "Magnetic ordering and spin dynamics in potassium jarosite: A heisenberg kagomé lattice antiferromagnet," *Phys. Rev. B*, vol. 67, p. 224435, Jun 2003.

[98] D. Grohol, K. Matan, J.-H. Cho, S.-H. Lee, J. W. Lynn, D. G. Nocera, and Y. S. Lee, "Spin chirality on a two-dimensional frustrated lattice," *Nat Mater*, vol. 4, pp. 323–328, 2005.

[99] A. S. Wills, V. Dupuis, E. Vincent, J. Hammann, and R. Calemczuk, "Aging in a topological spin glass," *Phys. Rev. B*, vol. 62, pp. R9264–R9267, Oct 2000.

[100] M. R. Norman, "Colloquium," *Rev. Mod. Phys.*, vol. 88, p. 041002, Dec 2016.

[101] A. Fukaya, Y. Fudamoto, I. M. Gat, T. Ito, M. I. Larkin, A. T. Savici, Y. J. Uemura, P. P. Kyriakou, G. M. Luke, M. T. Rovers, K. M. Kojima, A. Keren, M. Hanawa, and Z. Hiroi, "Muon spin relaxation and susceptibility studies of the pure and diluted spin $\frac{1}{2}$ kagomé-like lattice system $(Cu_xZn_{1-x})_3V_2O_7(OH_2)$ $2H_2O$," *Phys. Rev. Lett.*, vol. 91, p. 207603, Nov 2003.

[102] P. Mendels, F. Bert, M. A. de Vries, A. Olariu, A. Harrison, F. Duc, J. C. Trombe, J. S. Lord, A. Amato, and C. Baines, "Quantum magnetism in the paratacamite family: Towards an ideal kagomé lattice," *Phys. Rev. Lett.*, vol. 98, p. 077204, Feb 2007.

[103] M. B. Sanders, K. M. Baroudi, J. W. Krizan, O. A. Mukadam, and R. J. Cava, "Synthesis, crystal structure, and magnetic properties of novel 2d kagome materials $RE_3Sb_3Mg_2O_{14}$ (RE=La, Pr, Sm, Eu, Tb, Ho): Comparison to $RE_3Sb_3Zn_2O_{14}$ family," *physica status solidi (b)*, vol. 253, no. 10, pp. 2056–2065, 2016.

[104] W. Schweika, M. Valldor, and P. Lemmens, "Approaching the ground state of the kagomé antiferromagnet," *Phys. Rev. Lett.*, vol. 98, p. 067201, Feb 2007.

[105] B. Fåk, F. C. Coomer, A. Harrison, D. Visser, and M. E. Zhitomirsky, "Spin-liquid behavior in a kagomé antiferromagnet: Deuteronium jarosite," *EPL (Europhysics Letters)*, vol. 81, no. 1, p. 17006, 2008.

[106] S. Buhrandt and L. Fritz, "Spin-liquid phase and order by disorder of classical heisenberg spins on the swedenborgite lattice," *Phys. Rev. B*, vol. 90, p. 020403, Jul 2014.

[107] S. Buhrandt and L. Fritz, "Antiferromagnetic ising model on the swedenborgite lattice," *Phys. Rev. B*, vol. 90, p. 094415, Sep 2014.

[108] T. S. Sikkenk, K. Coester, S. Buhrandt, L. Fritz, and K. P. Schmidt, "Emergence of a two-dimensional macrospin liquid in a highly frustrated three-dimensional quantum magnet," *Phys. Rev. B*, vol. 95, p. 060401, Feb 2017.

[109] D. A. Huse and A. D. Rutenberg, "Classical antiferromagnets on the kagomé lattice," *Phys. Rev. B*, vol. 45, pp. 7536–7539, Apr 1992.

[110] A. B. Harris, C. Kallin, and A. J. Berlinsky, "Possible néel orderings of the kagomé antiferromagnet," *Phys. Rev. B*, vol. 45, pp. 2899–2919, Feb 1992.

[111] I. Ritchey, P. Chandra, and P. Coleman, "Spin folding in the two-dimensional heisenberg kagomé antiferromagnet," *Phys. Rev. B*, vol. 47, pp. 15342–15345, Jun 1993.

[112] J. N. Reimers and A. J. Berlinsky, "Order by disorder in the classical heisenberg kagomé antiferromagnet," *Phys. Rev. B*, vol. 48, pp. 9539–9554, Oct 1993.

[113] A. Keren, "Dynamical simulation of spins on kagomé and square lattices," *Phys. Rev. Lett.*, vol. 72, pp. 3254–3257, May 1994.

[114] J. Robert, B. Canals, V. Simonet, and R. Ballou, "Propagation and ghosts in the classical kagome antiferromagnet," *Phys. Rev. Lett.*, vol. 101, p. 117207, Sep 2008.

[115] M. Taillefumier, J. Robert, C. L. Henley, R. Moessner, and B. Canals, "Semi-classical spin dynamics of the antiferromagnetic heisenberg model on the kagome lattice," *Phys. Rev. B*, vol. 90, p. 064419, Aug 2014.

[116] C. L. Henley, "Long-range order in the classical kagome antiferromagnet: Effective hamiltonian approach," *Phys. Rev. B*, vol. 80, p. 180401, Nov 2009.

[117] D. A. Garanin and B. Canals, "Classical spin liquid: Exact solution for the infinite-component antiferromagnetic model on the kagomé lattice," *Phys. Rev. B*, vol. 59, pp. 443–456, Jan 1999.

[118] G.-W. Chern and R. Moessner, "Dipolar order by disorder in the classical heisenberg antiferromagnet on the kagome lattice," *Phys. Rev. Lett.*, vol. 110, p. 077201, Feb 2013.

[119] S. Schnabel and D. P. Landau, "Fictitious excitations in the classical heisenberg antiferromagnet on the kagome lattice," *Phys. Rev. B*, vol. 86, p. 014413, Jul 2012.

[120] J. Fouet, P. Sindzingre, and C. Lhuillier, "An investigation of the quantum $J_1 - J_2 - J_3$ model on the honeycomb lattice," *The European Physical Journal B - Condensed Matter and Complex Systems*, vol. 20, no. 2, pp. 241–254, 2001.

[121] P. H. Y. Li, R. F. Bishop, and C. E. Campbell, "A frustrated spin-1 J_1-J_2 heisenberg antiferromagnet: An anisotropic planar pyrochlore model," *Journal of Physics: Conference Series*, vol. 529, no. 1, p. 012008, 2014.

[122] L. Capriotti and S. Sorella, "Spontaneous plaquette dimerization in the J_1-J_2 heisenberg model," *Phys. Rev. Lett.*, vol. 84, pp. 3173–3176, Apr 2000.

[123] V. N. Kotov, J. Oitmaa, O. P. Sushkov, and Z. Weihong, "Low-energy singlet and triplet excitations in the spin-liquid phase of the two-dimensional J_1-J_2 model," *Phys. Rev. B*, vol. 60, pp. 14613–14616, Dec 1999.

[124] N. Shannon, B. Schmidt, K. Penc, and P. Thalmeier, "Finite temperature properties and frustrated ferromagnetism in a square lattice heisenberg model," *The European Physical Journal B - Condensed Matter and Complex Systems*, vol. 38, pp. 599–616, Apr 2004.

[125] B. Danu, G. Nambiar, and R. Ganesh, "Extended degeneracy and order by disorder in the square lattice $J_1 - J_2 - J_3$ model," *Phys. Rev. B*, vol. 94, p. 094438, Sep 2016.

[126] E. Rastelli, A. Tassi, and L. Reatto, "Non-simple magnetic order for simple Hamiltonians," *Physica B+C*, vol. 97, pp. 1–24, July 1979.

[127] C. Balz, B. Lake, J. Reuther, H. Luetkens, R. Schonemann, T. Herrmannsdorfer, Y. Singh, A. T. M. Nazmul Islam, E. M. Wheeler, J. A. Rodriguez-Rivera, T. Guidi, G. G. Simeoni, C. Baines, and H. Ryll, "Physical realization of a quantum spin liquid based on a complex frustration mechanism," *Nat. Phys.*, vol. 12, pp. 942–949, 10 2016.

[128] P. Chandra and B. Doucot, "Spin liquids on the husimi cactus," *Journal of Physics A: Mathematical and General*, vol. 27, no. 5, p. 1541, 1994.

[129] H. J. Liao, Z. Y. Xie, J. Chen, X. J. Han, H. D. Xie, B. Normand, and T. Xiang, "Heisenberg antiferromagnet on the husimi lattice," *Phys. Rev. B*, vol. 93, p. 075154, Feb 2016.

[130] P. Erdö and A. Rényi, "On random graphs i.," *Publ. Math. Debrecen*, vol. 6, pp. 290–297, 1959.

[131] R. Albert and A.-L. Barabási, "Statistical mechanics of complex networks," *Rev. Mod. Phys.*, vol. 74, pp. 47–97, Jan 2002.

[132] S. N. Dorogovtsev and J. F. F. Mendes, *Evolution of Networks: From Biological Nets to the Internet and WWW (Physics)*. New York, NY, USA: Oxford University Press, Inc., 2003.

[133] A. C. Esq., "VII. on the theory of groups, as depending on the symbolic equation $\theta^n = 1$," *Philosophical Magazine Series 4*, vol. 7, no. 42, pp. 40–47, 1854.

[134] P. Cayley, "Desiderata and suggestions: No. 2. the theory of groups: Graphical representation," *American Journal of Mathematics*, vol. 1, no. 2, pp. 174–176, 1878.

[135] M. Dehn, "Über die topologie des dreidimensionalen raumes. (mit 16 figuren im text)," *Mathematische Annalen*, vol. 69, pp. 137–168, 1910.

[136] M. Dehn, "Über unendliche diskontinuierliche gruppen. (mit 5 figuren im text).," *Mathematische Annalen*, vol. 71, pp. 116–144, 1912.

[137] L. K. Runnels, "Phase transition of a bethe lattice gas of hard molecules," *Journal of Mathematical Physics*, vol. 8, no. 10, pp. 2081–2087, 1967.

[138] T. P. Eggarter, "Cayley trees, the ising problem, and the thermodynamic limit," *Phys. Rev. B*, vol. 9, pp. 2989–2992, Apr 1974.

[139] J. Müller-Hartmann, E.and Zittartz, "Phase transitions of continuous order: Ising model on a cayley tree," *Zeitschrift für Physik B Condensed Matter*, vol. 22, no. 1, pp. 59–67, 1975.

[140] S. ichi Yoshida, K. Nemoto, and K. Wada, "Application of the cluster variation method to spin ice systems on the pyrochlore lattice," *Journal of the Physical Society of Japan*, vol. 71, no. 3, pp. 948–954, 2002.

[141] L. Bovo, L. D. C. Jaubert, P. C. W. Holdsworth, and S. T. Bramwell, "Crystal shape-dependent magnetic susceptibility and curie law crossover in the spin ices $Dy_2Ti_2O_7$ and $Ho_2Ti_2O_7$," *Journal of Physics: Condensed Matter*, vol. 25, no. 38, p. 386002, 2013.

[142] L. D. C. Jaubert, M. J. Harris, T. Fennell, R. G. Melko, S. T. Bramwell, and P. C. W. Holdsworth, "Topological-sector fluctuations and curie-law crossover in spin ice," *Phys. Rev. X*, vol. 3, p. 011014, Feb 2013.

[143] M. Udagawa, H. Ishizuka, and Y. Motome, "Quantum melting of charge ice and non-fermi-liquid behavior: An exact solution for the extended falicov-kimball model in the ice-rule limit," *Phys. Rev. Lett.*, vol. 104, p. 226405, Jun 2010.

[144] F. Harary and G. Uhlenbeck, "On the number of husimi trees: I.," *Proceedings of the National Academy of Sciences of the United States of America*, vol. 39, no. 4, pp. 315–322, 1953.

[145] K. Husimi, "Note on mayers' theory of cluster integrals," *The Journal of Chemical Physics*, vol. 18, no. 5, pp. 682–684, 1950.

[146] D. P. Kroese, T. Brereton, T. Taimre, and Z. I. Botev, "Why the monte carlo method is so important today," *Wiley Interdisciplinary Reviews: Computational Statistics*, vol. 6, no. 6, pp. 386–392, 2014.

[147] W. Krauth, *Statistical Mechanics: Algorithms and Computations*. Oxford : Oxford University Press, 2006.

[148] B. K. Landau, David P., *A Guide to Monte-Carlo Simulations in Statistical Physics*. Cambridge University Press, 3 ed., 2009.

[149] M. E. J. Newman and B. G. T., *Monte Carlo Methods in Statistical Physics*. Clarendon Press, illustrated, reprint ed., 2010.

[150] M. Michel, S. C. Kapfer, and W. Krauth, "Generalized event-chain monte carlo: Constructing rejection-free global-balance algorithms from infinitesimal steps," *The Journal of Chemical Physics*, vol. 140, no. 5, p. 054116, 2014.

[151] M. Michel, J. Mayer, and W. Krauth, "Event-chain monte carlo for classical continuous spin models," *EPL (Europhysics Letters)*, vol. 112, no. 2, p. 20003, 2015.

[152] Y. Nishikawa, M. Michel, W. Krauth, and K. Hukushima, "Event-chain algorithm for the heisenberg model: Evidence for $z \simeq 1$ dynamic scaling," *Phys. Rev. E*, vol. 92, p. 063306, Dec 2015.

[153] Y. Nishikawa and K. Hukushima, "Phase transitions and ordering structures of a model of a chiral helimagnet in three dimensions," *Phys. Rev. B*, vol. 94, p. 064428, Aug 2016.

[154] J. W. Gibbs, "Elementary principles in statistical mechanics," 1902.

[155] N. Metropolis, "Equation of state calculations by fast computing machines," *The Journal of Chemical Physics*, vol. 21, no. 6, pp. 1087–1092, 1953.

[156] S. Carnot, *Réflexions sur la puissance motrice du feu et sur les machines propres à développer atte puissance*. Bachelier Libraire (in French), 1824.

[157] M. C. Clapeyron, "Mémoire sur la puissance motrice de la chaleur," *Journal de l'École polytechnique (in French)*, vol. 23, pp. 153–190, 1834.

[158] R. Peierls, "On ising's model of ferromagnetism," *Mathematical Proceedings of the Cambridge Philosophical Society*, vol. 32, no. 3, p. 477?481, 1936.

[159] E. Ising, "Beitrag zur theorie des ferromagnetismus," *Zeitschrift für Physik*, vol. 31, pp. 253–258, 1924.

[160] R. Wielinga, H. Blöte, J. Roest, and W. Huiskamp, "Specific heat singularities of the ising antiferromagnets $CoCs_3Cl_5$ and $CoCs_3Br_5$," *Physica*, vol. 34, no. 2, pp. 223 – 240, 1967.

[161] J. C. Wright, H. W. Moos, J. H. Colwell, B. W. Mangum, and D. D. Thornton, "$DyPO_4$: A three-dimensional ising antiferromagnet," *Phys. Rev. B*, vol. 3, pp. 843–858, Feb 1971.

[162] W. H. Press, S. A. Teukolsky, W. T. Vetterling, and B. P. Flannery, *Numerical Recipes 3rd Edition: The Art of Scientific Computing*. New York, NY, USA: Cambridge University Press, 3rd ed., 2007.

[163] U. Wolff, "Collective monte carlo updating for spin systems," *Phys. Rev. Lett.*, vol. 62, pp. 361–364, Jan 1989.

[164] R. H. Swendsen and J.-S. Wang, "Nonuniversal critical dynamics in monte carlo simulations," *Phys. Rev. Lett.*, vol. 58, pp. 86–88, Jan 1987.

[165] D. Sherrington and S. Kirkpatrick, "Solvable model of a spin-glass," *Phys. Rev. Lett.*, vol. 35, pp. 1792–1796, Dec 1975.

[166] R. B. Potts, "Some generalized order-disorder transformations," *Mathematical Proceedings of the Cambridge Philosophical Society*, vol. 48, no. 1, p. 106?109, 1952.

[167] J. D. M. Champion, A. S. Wills, T. Fennell, S. T. Bramwell, J. S. Gardner, and M. A. Green, "Order in the heisenberg pyrochlore: The magnetic structure of $Gd_2Ti_2O_7$," *Phys. Rev. B*, vol. 64, p. 140407, Sep 2001.

[168] J. R. Stewart, G. Ehlers, A. S. Wills, S. T. Bramwell, and J. S. Gardner, "Phase transitions, partial disorder and multi- k structures in $Gd_2Ti_2O_7$," *Journal of Physics: Condensed Matter*, vol. 16, no. 28, p. L321, 2004.

[169] S. V. Isakov, J. M. Hopkinson, and H.-Y. Kee, "Fate of partial order on trillium and distorted windmill lattices," *Phys. Rev. B*, vol. 78, p. 014404, Jul 2008.

[170] H. Kawamura, "Spin- and chirality-orderings of frustrated magnets stacked-triangular anti-ferromagnets and spin glasses," *Canadian Journal of Physics*, vol. 79, no. 11-12, pp. 1447–1458, 2001.

[171] G. Marsaglia, "Choosing a point from the surface of a sphere," *The Annals of Mathematical Statistics*, vol. 43, no. 2, pp. 645–646, 1972.

[172] J. M. Cook, "Technical notes and short papers: Rational formulae for the production of a spherically symmetric probability distribution," *Math. Tables Aids Comput*, vol. 11, pp. 81–82, 1957.

[173] M. E. Muller, "A note on a method for generating points uniformly on n-dimensional spheres," *Commun. ACM*, vol. 2, pp. 19–20, apr 1959.

[174] F. R. Brown and T. J. Woch, "Overrelaxed heat-bath and metropolis algorithms for accelerating pure gauge monte carlo calculations," *Phys. Rev. Lett.*, vol. 58, pp. 2394–2396, Jun 1987.

[175] M. Creutz, "Overrelaxation and monte carlo simulation," *Phys. Rev. D*, vol. 36, pp. 515–519, Jul 1987.

[176] Y. Miyatake, M. Yamamoto, J. J. Kim, M. Toyonaga, and O. Nagai, "On the implementation of the 'heat bath' algorithms for monte carlo simulations of classical heisenberg spin systems," *Journal of Physics C: Solid State Physics*, vol. 19, no. 14, p. 2539, 1986.

[177] J. A. Olive, A. P. Young, and D. Sherrington, "Computer simulation of the three-dimensional short-range heisenberg spin glass," *Phys. Rev. B*, vol. 34, pp. 6341–6346, Nov 1986.

[178] R. H. Swendsen and J.-S. Wang, "Replica monte carlo simulation of spin-glasses," *Phys. Rev. Lett.*, vol. 57, pp. 2607–2609, Nov 1986.

[179] K. Hukushima and K. Nemoto, "Exchange monte carlo method and application to spin glass simulations," *Journal of the Physical Society of Japan*, vol. 65, no. 6, pp. 1604–1608, 1996.

[180] Y. Sugita and Y. Okamoto, "Replica-exchange molecular dynamics method for protein folding," *Chemical Physics Letters*, vol. 314, no. 1–2, pp. 141 – 151, 1999.

[181] M. Falcioni and M. W. Deem, "A biased monte carlo scheme for zeolite structure solution," *The Journal of Chemical Physics*, vol. 110, no. 3, pp. 1754–1766, 1999.

[182] D. J. Earl and M. W. Deem, "Parallel tempering: Theory, applications, and new perspectives," *Phys. Chem. Chem. Phys.*, vol. 7, pp. 3910–3916, 2005.

[183] E. Hairer, G. Wanner, and S. P. Nørsett, *Solving Ordinary Differential Equations I – Nonstiff Problems*. Springer Berlin Heidelberg, 1993.

[184] E. Fermi, J. Pasta, S. Ulam, and M. Tsingou, "Studies of nonlinear problems. 1," 1955.

[185] B. J. Alder and T. E. Wainwright, "Studies in molecular dynamics. I. general method," *The Journal of Chemical Physics*, vol. 31, no. 2, pp. 459–466, 1959.

[186] L. Euler and O. Omnia, *Institutiones calculi integralis 2nd part.* Birkhäuser, 1914.

[187] C. Runge, "Über die numerische auflösung von differentialgleichungen," *Mathematische Annalen*, vol. 46, pp. 167–178, 1895.

[188] Heun, "Neue methoden zur approximativen integration der differentialgleichungen einer unabhängigen veränderlichen," *Z. Math. Phys.*, vol. 45, pp. 23–38, 1900.

[189] W. Kutta, "Beitrag zur näherungsweisen integration totaler differentialgleichungen," *Z. Math. Phys.*, vol. 46, pp. 435–453, 1901.

[190] C. Kawabata, M. Takeuchi, and A. R. Bishop, "Monte carlo molecular dynamics simulations for two-dimensional magnets," *Journal of Statistical Physics*, vol. 43, pp. 869–871, Jun 1986.

[191] C. Kawabata, M. Takeuchi, and A. Bishop, "Simulation of the dynamic structure factor for two-dimensional classical heisenberg ferromagnets," *Journal of Magnetism and Magnetic Materials*, vol. 54, pp. 871 – 872, 1986.

[192] S. Lovesey, *Theory of Neutron Scattering from Condensed Matter*. No. v. 2 in International Series of Monogr, Clarendon Press, 1986.

[193] G. Squires, *Introduction to the Theory of Thermal Neutron Scattering*. Cambridge University Press, 2012.

[194] Y. Katznelson, *An Introduction to Harmonic Analysis*. Dover, 3 ed., 2002.

[195] A. P. Ramirez, "Strongly geometrically frustrated magnets," *Annual Review of Materials Science*, vol. 24, no. 1, pp. 453–480, 1994.

[196] A. Nag and S. Ray, "Misjudging frustrations in spin liquids from oversimplified use of curie-weiss law," *Journal of Magnetism and Magnetic Materials*, vol. 424, pp. 93 – 98, 2017.

[197] S. T. Bramwell, M. N. Field, M. J. Harris, and I. P. Parkin, "Bulk magnetization of the heavy rare earth titanate pyrochlores - a series of model frustrated magnets," *Journal of Physics: Condensed Matter*, vol. 12, no. 4, p. 483, 2000.

[198] T. T. A. Lummen, I. P. Handayani, M. C. Donker, D. Fausti, G. Dhalenne, P. Berthet, A. Revcolevschi, and P. H. M. van Loosdrecht, "Phonon and crystal field excitations in geometrically frustrated rare earth titanates," *Phys. Rev. B*, vol. 77, p. 214310, Jun 2008.

[199] G. Misguich, B. Bernu, and L. Pierre, "Determination of the exchange energies in Li_2VOSiO_4 from a high-temperature series analysis of the square-lattice J_1-J_2 heisenberg model," *Phys. Rev. B*, vol. 68, p. 113409, Sep 2003.

[200] L. D. C. Jaubert, J. T. Chalker, P. C. W. Holdsworth, and R. Moessner, "Three-dimensional kasteleyn transition: Spin ice in a [100] field," *Phys. Rev. Lett.*, vol. 100, p. 067207, Feb 2008.

[201] L. D. C. Jaubert, J. T. Chalker, P. C. W. Holdsworth, and R. Moessner, "The kasteleyn transition in three dimensions: Spin ice in a [100] field," *Journal of Physics: Conference Series*, vol. 145, no. 1, p. 012024, 2009.

[202] N. Prokof'ev and B. Svistunov, "Worm algorithms for classical statistical models," *Phys. Rev. Lett.*, vol. 87, p. 160601, Sep 2001.

[203] J. F. Nagle, "Lattice statistics of hydrogen bonded crystals. I. the residual entropy of ice," *Journal of Mathematical Physics*, vol. 7, no. 8, pp. 1484–1491, 1966.

[204] H. Nakano and T. Sakai, "The two-dimensional S=1/2 heisenberg antiferromagnet on the shurikenlattice – a lattice composed of vertex-sharing triangles," *Journal of the Physical Society of Japan*, vol. 82, p. 083709, Aug. 2013.

[205] R. Siddharthan and A. Georges, "Square kagome quantum antiferromagnet and the eight-vertex model," *Physical Review B*, vol. 65, p. 014417, Dec. 2001.

[206] J. Richter, O. Derzhko, and J. Schulenburg, "Magnetic-field induced spin-peierls instability in strongly frustrated quantum spin lattices," *Physical Review Letters*, vol. 93, p. 107206, Sept. 2004.

[207] O. Derzhko and J. Richter, "Universal low-temperature behavior of frustrated quantum antiferromagnets in the vicinity of the saturation field," *The European Physical Journal B*, vol. 52, pp. 23–36, July 2006.

[208] J. Richter, J. Schulenburg, P. Tomczak, and D. Schmalfuss, "The heisenberg antiferromagnet on the square-kagomé lattice," *Condensed Matter Physics*, vol. 12, no. 3, pp. 507–517, 2009.

[209] O. Derzhko, J. Richter, O. Krupnitska, and T. Krokhmalskii, "Frustrated quantum heisenberg antiferromagnets at high magnetic fields: Beyond the flat-band scenario," *Phys. Rev. B*, vol. 88, p. 094426, Sep 2013.

[210] H. Nakano, T. Sakai, and Y. Hasegawa, "Spin-flop phenomenon of two-dimensional frustrated antiferromagnets without anisotropy in spin space," *Journal of the Physical Society of Japan*, vol. 83, p. 084709, Aug. 2014.

[211] H. Nakano, Y. Hasegawa, and T. Sakai, "Magnetization jump in the magnetization process of the spin-1/2 heisenberg antiferromagnet on a distorted square-kagome lattice," *Journal of the Physical Society of Japan*, vol. 84, no. 11, p. 114703, 2015.

[212] A. Ralko and I. Rousochatzakis, "Resonating-valence-bond physics is not always governed by the shortest tunneling loops," *Physical Review Letters*, vol. 115, p. 167202, Oct. 2015.

[213] P. Tomczak and J. Richter, "Specific heat of the spin-1/2 heisenberg antiferromagnet on squagome lattice," *Journal of Physics A: Mathematical and General*, vol. 36, no. 20, p. 5399, 2003.

[214] A. W. Glaetzle, M. Dalmonte, R. Nath, I. Rousochatzakis, R. Moessner, and P. Zoller, "Quantum spin-ice and dimer models with rydberg atoms," *Phys. Rev. X*, vol. 4, p. 041037, Nov 2014.

[215] I. Rousochatzakis, R. Moessner, and J. van den Brink, "Frustrated magnetism and resonating valence bond physics in two-dimensional kagome-like magnets," *Physical Review B*, vol. 88, p. 195109, Nov. 2013.

[216] I. Rousochatzakis, A. M. Läuchli, and R. Moessner, "Quantum magnetism on the cairo pentagonal lattice," *Phys. Rev. B*, vol. 85, p. 104415, 2012.

[217] O. Derzhko, J. Richter, O. Krupnitska, and T. Krokhmalskii, "The square-kagome quantum heisenberg antiferromagnet at high magnetic fields: The localized-magnon paradigm and beyond," *Low Temperature Physics*, vol. 40, pp. 513–520, June 2014.

[218] S. Chun-Feng, K. Xiang-Mu, and Y. Xun-Chang, "A solvable decorated ising lattice model," *Communications in Theoretical Physics*, vol. 45, no. 3, p. 555, 2006.

[219] E. H. Lieb, "Two theorems on the hubbard model," *Phys. Rev. Lett.*, vol. 62, pp. 1201–1204, 1989.

[220] Y. Crespo, A. Andreanov, and N. Seriani, "Competing antiferromagnetic and spin-glass phases in a hollandite structure," *Phys. Rev. B*, vol. 88, p. 014202, Jul 2013.

[221] W. Li, S.-S. Gong, Y. Zhao, S.-J. Ran, S. Gao, and G. Su, "Phase transitions and thermodynamics of the two-dimensional ising model on a distorted kagome lattice," *Phys. Rev. B*, vol. 82, p. 134434, 2010.

[222] W. Apel and H.-U. Everts, "Correlations in the ising antiferromagnet on the anisotropic kagome lattice," *Journal of Statistical Mechanics: Theory and Experiment*, vol. 2011, no. 09, p. P09002, 2011.

[223] S. Bieri, L. Messio, B. Bernu, and C. Lhuillier, "Gapless chiral spin liquid in a kagome heisenberg model," *Phys. Rev. B*, vol. 92, p. 060407, 2015.

[224] O. Benton and N. Shannon, "Ground state selection and spin-liquid behaviour in the classical heisenberg model on the breathing pyrochlore lattice," *Journal of the Physical Society of Japan*, vol. 84, no. 10, p. 104710, 2015.

[225] M. Elhajal, B. Canals, and C. Lacroix, "Symmetry breaking due to dzyaloshinsky-moriya interactions in the kagomé lattice," *Phys. Rev. B*, vol. 66, p. 014422, Jul 2002.

[226] B. Canals, M. Elhajal, and C. Lacroix, "Ising-like order by disorder in the pyrochlore antiferromagnet with dzyaloshinskii-moriya interactions," *Phys. Rev. B*, vol. 78, p. 214431, Dec. 2008.

[227] P. A. McClarty, P. Stasiak, and M. J. P. Gingras, "Order-by-disorder in the xy pyrochlore antiferromagnet," *Phys. Rev. B*, vol. 89, p. 024425, Jan 2014.

[228] S. V. Isakov, K. S. Raman, R. Moessner, and S. L. Sondhi, "Magnetization curve of spin ice in a [111] magnetic field," *Phys. Rev. B*, vol. 70, p. 104418, SEP 2004.

[229] I. A. Ryzhkin, "Magnetic relaxation in rare-earth oxide pyrochlores," *Journal of Experimental and Theoretical Physics*, vol. 101, no. 3, pp. 481–486, 2005.

[230] P. H. Conlon and J. T. Chalker, "Absent pinch points and emergent clusters: Further neighbor interactions in the pyrochlore heisenberg antiferromagnet," *Phys. Rev. B*, vol. 81, June 2010.

[231] M. Isoda, "A mechanism for the downturn in inverse susceptibility in triangle-based frustrated spin systems," *Journal of Physics: Condensed Matter*, vol. 20, no. 31, p. 315202, 2008.

[232] A. J. Macdonald, P. C. W. Holdsworth, and R. G. Melko, "Classical topological order in kagome ice," *Journal of Physics-Condensed Matter*, vol. 23, p. 164208, Apr. 2011.

[233] D. P. Landau, B. E. Keen, B. Schneider, and W. P. Wolf, "Magnetic and thermal properties of dysprosium aluminum garnet. I. experimental results for the two-sublattice phases," *Phys. Rev. B*, vol. 3, pp. 2310–2343, 1971.

[234] W. P. Wolf, B. Schneider, D. P. Landau, and B. E. Keen, "Magnetic and thermal properties of dysprosium aluminum garnet. II. characteristic parameters of an ising antiferromagnet," *Phys. Rev. B*, vol. 5, pp. 4472–4496, 1972.

[235] W. P. Wolf, "The ising model and real magnetic materials," *Brazilian Journal of Physics*, vol. 30, pp. 794 – 810, 12 2000.

[236] S. Zhang, J. Li, I. Gilbert, J. Bartell, M. J. Erickson, Y. Pan, P. E. Lammert, C. Nisoli, K. K. Kohli, R. Misra, V. H. Crespi, N. Samarth, C. Leighton, and P. Schiffer, "Perpendicular magnetization and generic realization of the ising model in artificial spin ice," *Phys. Rev. Lett.*, vol. 109, p. 087201, Aug 2012.

[237] I. A. Chioar, N. Rougemaille, A. Grimm, O. Fruchart, E. Wagner, M. Hehn, D. Lacour, F. Montaigne, and B. Canals, "Nonuniversality of artificial frustrated spin systems," *Phys. Rev. B*, vol. 90, p. 064411, Aug 2014.

[238] I. A. Chioar, N. Rougemaille, and B. Canals, "Ground-state candidate for the classical dipolar kagome ising antiferromagnet," *Phys. Rev. B*, vol. 93, p. 214410, Jun 2016.

[239] J. Hablützel, "Dielelektrische untersuchungen an $KNaC_4H_2D_2O_6{\cdot}4D_2O$ - kristallen," *Helv. Phys. Acta*, vol. 12, p. 489, 1939.

[240] V. Vaks, A. Larkin, and Y. N. Ovchinnikov, "Ising model with interaction between nonnearest neighbors," *Soviet Physics JETP*, vol. 22, pp. 820–826, Apr 1966.

[241] A. N. Berker and J. S. Walker, "Frustrated spin-gas model for doubly reentrant liquid crystals," *Phys. Rev. Lett.*, vol. 47, pp. 1469–1472, Nov 1981.

[242] P. Cladis, "A 100 year perspective of the reentrant nematic phase," *Molecular Crystals and Liquid Crystals*, vol. 165, pp. 85–121, 1988.

[243] G. Aeppli, S. M. Shapiro, R. J. Birgeneau, and H. S. Chen, "Spin correlations and reentrant spin-glass behavior in amorphous Fe-Mn alloys: Statics," *Phys. Rev. B*, vol. 28, pp. 5160–5172, Nov 1983.

[244] M. Rojas, O. Rojas, and S. M. de Souza, "Frustrated ising model on the cairo pentagonal lattice," *Phys. Rev. E*, vol. 86, p. 051116, 2012.

[245] P. A. McClarty, O. Sikora, R. Moessner, K. Penc, F. Pollmann, and N. Shannon, "Chain-based order and quantum spin liquids in dipolar spin ice," *Phys. Rev. B*, vol. 92, p. 094418, Sep 2015.

[246] P. Henelius, T. Lin, M. Enjalran, Z. Hao, J. G. Rau, J. Altosaar, F. Flicker, T. Yavors'kii, and M. J. P. Gingras, "Refrustration and competing orders in the prototypical $Dy_2Ti_2O_7$ spin ice material," *Phys. Rev. B*, vol. 93, p. 024402, Jan 2016.

[247] Y. Okamoto, G. J. Nilsen, J. P. Attfield, and Z. Hiroi, "Breathing pyrochlore lattice realized in *A*-site ordered spinel oxides $LiGaCr_4O_8$ and $LiInCr_4O_8$," *Phys. Rev. Lett.*, vol. 110, p. 097203, Feb 2013.

[248] K. Kimura, S. Nakatsuji, and T. Kimura, "Experimental realization of a quantum breathing pyrochlore antiferromagnet," *Phys. Rev. B*, vol. 90, p. 060414, Aug 2014.

[249] C. Balz, B. Lake, A. T. M. Nazmul Islam, Y. Singh, J. A. Rodriguez-Rivera, T. Guidi, E. M. Wheeler, G. G. Simeoni, and H. Ryll, "Magnetic Hamiltonian and phase diagram of the quantum spin liquid $Ca_{10}Cr_7O_{28}$," *Phys. Rev. B*, vol. 95, p. 174414, May 2017.

[250] C. Balz, B. Lake, M. Reehuis, A. T. M. N. Islam, O. Prokhnenko, Y. Singh, P. Pattison, and S. Tóth, "Crystal growth, structure and magnetic properties of $Ca_10Cr_7O_28$," *Journal of Physics: Condensed Matter*, vol. 29, no. 22, p. 225802, 2017.

[251] D. Gyepesová, M. Handlovic, and S. Durovič, "The crystal structure of $Ca_3(CrO_4)_2$," *Silikaty č*, vol. 2, pp. 113–15, 1981.

[252] I. Arcon, B. Mirtic, and A. Kodre, "Determination of valence states of chromium in calcium chromates by using x-ray absorption near-edge structure (xanes) spectroscopy," *Journal of the American Ceramic Society*, vol. 81, no. 1, pp. 222–224, 1998.

[253] D. Gyepesová and V. Langer, " $Ca_{10}(Cr^VO_4)_6(Cr^{VI}O_4)$, a disordered mixed-valence chromium compound exhibiting inversion twinning," *Acta Crystallographica Section C*, vol. 69, pp. 111–113, Feb 2013.

[254] C. Balz, *Investigation of low–dimensional and frustrated spin–1/2 magnets*. PhD thesis, Technische Universität Berlin, 2015.

[255] D. Bergman, J. Alicea, E. Gull, S. Trebst, and L. Balents, "Order-by-disorder and spiral spin-liquid in frustrated diamond-lattice antiferromagnets," *Nat Phys*, vol. 3, pp. 487–491, July 2007.

[256] S. Gao, O. Zaharko, V. Tsurkan, Y. Su, J. S. White, G. S. Tucker, B. Roessli, F. Bourdarot, R. Sibille, D. Chernyshov, T. Fennell, A. Loidl, and C. Ruegg, "Spiral spin-liquid and the emergence of a vortex-like state in $MnSc_2S_4$," *Nat Phys*, vol. 13, pp. 157–161, Feb 2017.

[257] L. E. Svistov, T. Fujita, H. Yamaguchi, S. Kimura, K. Omura, A. Prokofiev, A. I. Smirnov, Z. Honda, and M. Hagiwara, "New high magnetic field phase of the frustrated S = 1/2 chain compound $LiCuVO_4$," *JETP Letters*, vol. 93, pp. 21–25, Mar 2011.

[258] M. Takahashi, "Modified spin-wave theory of a square-lattice antiferromagnet," *Phys. Rev. B*, vol. 40, pp. 2494–2501, Aug 1989.

[259] A. J. Dianoux and G. Lander, "Neutron data booklet." ISBN: 0-9704143-7-4.